Probing the proton structure through deep virtual Compton scattering at COMPASS, CERN

Antoine Vidon

université PARIS-SACLAY

NNT : 2019SACLS340

Thèse de doctorat

Probing the proton structure through deep virtual Compton scattering at COMPASS, CERN

Thèse de doctorat de l'Université Paris-Saclay
préparée à l'Université Paris-Sud

École doctorale n°576 Particules, Hadrons, Énergie, Noyau, Instrumentation, Imagerie, Cosmos et Simulation (PHENIICS)
Spécialité de doctorat : Physique Hadronique

Thèse présentée et soutenue à Saclay, le 1er Octobre 2019, par

ANTOINE VIDON

Composition du Jury :

Michel Guidal Directeur de recherche, IPNO, CNRS	Président
Eva-Maria Kabuß Prof. Dr., Institut fuer Kernphysik, Universität Mainz	Rapporteuse
Elke-Caroline Aschenauer Tenured senior scientist, Medium energy group, BNL	Rapporteuse
Cédric Lorcé Maître de Conférence, IPHT, École Polytechnique	Examinateur
Nicole d'Hose Directrice de recherche, DPhN, CEA/IRFU	Directrice de thèse
Andrea Ferrero Ingénieur de recherche, DPhN, CEA/IRFU	Co-directeur de thèse

À Toulouse, à San-Francisco, et à quelques autres encore...

REMERCIEMENTS

Quand j'ai annoncé à ma Grand-Mère que j'allais commencer une thèse de physique, elle s'est exclamée, inquiète : « Mais tu vas être pauvre ! ». Ses craintes se seront révélées en partie fondées, puisque je suis effectivement devenu chômeur, mais je ne crois pas pouvoir honnêtement prétendre à la pauvreté. Plutôt, au contraire, je n'ai jamais été aussi riche qu'au moment de quitter – avec autant de joie que de nostalgie – ce beau laboratoire.

C'est que la thèse est avant toute chose une aventure : c'est la variation contemporaine du *Grand Tour*, ce voyage de quelques années qui tout au long des XVII^{ème} et XVIII^{ème} siècles parachevait la formation intellectuelle, sociale et culturelle des jeunes aristocrates qui sillonnaient l'Europe accompagnés de leur *tutor*. Je suis aujourd'hui un *touriste*, qui rentre de son long voyage l'esprit libre et le cœur plein de souvenirs ; probablement un peu meilleur qu'au départ, certainement un peu plus vieux, mais avec la conviction inébranlable que cette aventure, le plus souvent palpitante, quelquefois difficile – parfois même déplaisante – mais jamais ennuyeuse, méritait chaque instant que je lui ai consacré.

Et parce que les plus beaux paysages, même intellectuels, n'ont pas la moindre saveur sans la compagnie appropriée, je voudrais ici chaleureusement remercier tous ceux qui, pour une heure ou pour plusieurs années, ont été mes compagnons de voyage.

Je voudrais d'abords remercier ceux qui m'ont permis d'en rentrer, parce que toutes les aventures doivent bien se terminer un jour. En ce sens je remercie mon jury : Michel Guidal, Cédric Lorcé, et mes deux rapporteuses Eva-Maria Kabuß et Elke Ashenauer pour leur relecture attentive et rigoureuse de mon manuscrit, qui n'en ressort que meilleur, ainsi que pour m'avoir fait vivre ce qui aura probablement été la soutenance de thèse la plus courte de mon existence. Rentrer de voyage est toujours un peu compliqué aussi bien logistiquement qu'émotionnellement, et je suis ravi d'avoir pu le faire sous leur égide à la fois joyeuse et exigeante. J'en profite également pour remercier les secrétaires de l'université, toujours souriantes et réactives, qui m'ont permis de surmonter quelques surprises de (toutes) dernières minutes.

Si le retour est toujours un moment important, je dois admettre que je n'aime rien de mieux que les départs. J'affectionne ce moment où se côtoient, dans un frémissement irrésistiblement guilleret, l'enthousiasme de la nouveauté et la peur de l'inconnu. Je veux manifester ma gratitude au CEA, qui m'aura permis de prendre celui-ci en me finançant pendant trois ans, mais surtout à la direction du laboratoire, en les personnes de Franck et Jacques, qui ont pris au sérieux mon retour à la physique après un master en sciences-humaines et sociales. Je voudrais remercier avec eux tous les chercheurs qui se sont battus pour en persuader la direction de l'école doctorale d'alors, qui – nettement moins convaincue – m'aura mis quelques bâtons dans les roues.

J'ai eu la chance grâce à eux de pouvoir faire du DPhN mon camp de base. Cela n'aurait pas été possible sans l'aide logistique extensive de Danielle et d'Isabelle, que je remercie autant

pour leur soutien technique que pour leur personnalité lumineuse, je mesure combien le laboratoire à de la chance de les avoir ! Je voudrais aussi remercier Franck pour toute la bienveillance et l'attention qu'il porte aux étudiants, qui permettent un encadrement sérieux et humain des thésards.

Ce laboratoire a été, tout au long de ma thèse et malgré sa distance à la ville, un espace agréable où j'ai toujours aimé me rendre. Faisant de chaque journée comme un voyage à la campagne, ce lieu demeure confortable malgré ses spartiates propriétés thermiques, ceci grâce à la compagnie chaleureuse des permanents qui l'occupent. Personnalités complexes et abouties, ne manquant pas d'humour, j'ai pris beaucoup de plaisir à partager avec eux aussi bien de la physique que des repas, ou d'indécentes pauses café. J'ai une pensée particulière pour Thomas, que j'ai dû convaincre un matin d'aller jusqu'au travail alors que nous étions coincés par la neige au guichet, pour Pierre, et ses visites récurrentes dans le bureau de Nicole agrémentées de bonbons, pour Jaume et ses anecdotes invraisemblables. J'aimerais aussi remercier les nouveaux embauchés pour leur présence enthousiaste et chaleureuse. J'aimerais remercier Maxime pour les volumineux documents sur le DVCS qu'il m'a transmis en début de thèse, et pour ces longues promenades à parler de physique dans la campagne toscane.

Je voudrais surtout remercier tous les permanents pour le talent indéniable qu'ils démontrent dans le choix de leurs étudiants. Les précaires forment au laboratoire une fresque vivante et bariolée d'individus fantasques, qui comptent au moins autant que la physique en ce qui concerne la qualité du voyage. Je voudrais les remercier d'avoir été, certains pendant quatre ans, les auditeurs attentifs de mes aventures perpétuellement rocambolesques, et d'avoir supporté en souriant mes originalités et mon humeur parfois changeante. Je me rappellerai en particulier longtemps, et avec émotion, notre découverte émerveillée et au pas de course des forets du plateau avec Aurélie, lorsque nous avons commencé simultanément l'aventure. Elle restera pour moi une amie fidèle et une physicienne impressionnante. Je remercie Valérian pour son invariable irrévérence, avec qui nous nous sommes perdus plus d'une fois dans les bois à l'époque. Je remercie Loïc, qui en plus d'être un coach imparable, est définitivement un ami joyeux sur qui l'on peut compter pour partir en vadrouille, même à l'autre bout du monde. Je remercie Mehdi qui, avant de se retrouver noyé sous sa rédaction, aura été pour moi une inégalable besta. Je remercie Christopher pour son humeur rayonnante même dans le malheur, pour son vocabulaire incompréhensible, et pour nos indispensables lectures croisées de l'horoscope. Je remercie Saba pour sa capacité à s'indigner, et tous ce qu'elle représente d'empowerement. Je remercie Adrien, pour sa foi inébranlable en la physique et sa volonté de feu, toujours prêt à sourire. Je remercie Charles pour la profondeur de nos conversations, toujours agréables sans être inconséquentes, parfois sous les étoiles. Je remercie benjamin pour ses gâteaux, Noëlie pour m'avoir prêté Brian, et nous avoir aidé avec Matplotlib. Et je remercie nos prédécesseurs pour tous ce qu'ils ont impulsé de bonne humeur !

Mon bureau à la campagne, si confortablement équipé de ses plantes, sa bibliothèque et de son salon de thé, a été partagé avec deux compagnons qui, sachant qu'il valait mieux ne pas me laisser seul, se seront aimablement relayé à mes côtés. Marco d'abord, qui m'a reçu au CERN au début de ma thèse comme si nous étions amis de longue date – il n'y a rien de plus agréable que de se sentir accueilli avec autant de chaleur lorsqu'on arrive quelque part – et qui

m'a aidé à me faire une place parmi les étudiants de la collaboration. Je le remercie pour toutes ces soirées perdues aux restaurant où il aura choisi ma compagnie à celle de la physique, pour m'avoir fait découvrir le col de la faucille à moto et pour m'avoir aidé à aménager le bureau !

Nicolas, ensuite, qui rentrant d'Allemagne quand Marco partait pour les Amériques, est devenu mon inséparable compagnon de voyage pendant ma dernière année de thèse. Je le remercie pour tous ces moments de complicité intense où nous avons pu, ensemble, laisser libre cours à notre fantaisie aussi bien face à la collaboration qu'au laboratoire. Il a été pour moi le meilleur binôme de TP qu'il m'ai été donnée d'avoir, et je le remercie pour sa patience infinie et son aide conséquente avec l'informatique.

J'aimerais surtout remercier l'équipe avec laquelle je me suis embarqué pour cette palpitante aventure. La première fois que j'ai rencontré Nicole, affublée d'un improbable pull rose à pompon dans la cantine du centre, je n'aurais sans doute pas su prédire qu'elle deviendrait ma directrice de thèse. Je la remercie infiniment pour ces années de physique et d'amitié qui ont été pour moi une expérience décisive. Je la remercie d'avoir su canaliser mes ardeurs, d'avoir toléré mes écarts et de m'avoir apporté pendant ces quelques années la rigueur qui me manquera probablement toujours. Je la remercie aussi mille fois de m'avoir emporté dans ses valises à de multiples reprises, et je retiendrai toujours que c'est elle qui m'a donné le goût, incomparablement délicieux, du voyage scientifique. Je la remercie encore pour ces merveilleuses soirées à Ferney et à Gif, et pour m'avoir fait découvrir sa sublime fromagerie jurassienne.

Je remercie Andrea, qui m'a appris le C++ avec une patience sans limites, qui m'a appris à ne pas être effrayé par des scripts Bash (cet apprentissage-là a été plus long encore que le précédent), qui n'a eu de cesse de m'aider à produire mes résultats et surtout mes calibrations, et qui a continué de m'encadrer même après avoir quitté la manip. Je lui suis vraiment reconnaissant de m'avoir appris à évoluer dans la collaboration sans trop craindre mes pairs. Je le remercie pour la tranquillité qu'il a su instiller face aux urgences. Il a été le nécessaire complément à l'encadrement de Nicole et c'est définitivement leur présence associée qui m'a décidé à revenir faire ma thèse à Saclay.

Ayant rejoint plus récemment l'aventure mais n'étant pas moins importants, j'aimerais remercier chaleureusement mes deux camarades Brian et Po-Ju. In particular, I would like to express my deepest gratitude to both of them for the work we managed to achieve as "the Saclay team". It has been an incredibly crazy, pleasant and productive year working along with them, and I would probably never have completed my PhD if it were not for their help! I want to sincerely thank Po-Ju for his infinite phlegm and dedication; even when I was asking him to do impossible things from scratch he would simply say yes and return to me with the job done. I really thank him for playing along with our unrealistic deadlines, and for answering the phone at night to allow us to reach those. But most importantly, and besides his impressive physics skills, I really would like to thank him for his sense of humor, his serenity, his smile and enthusiasm and his incredibly bright and expressive eyes!

J'aimerais aussi adresser mes plus sincères remerciements à Brian, que j'ai eu la chance d'accompagner dans la découverte de cette physique. Je le remercie pour les innombrables voyages dans lesquels il a accepté de m'accompagner, et pour avoir gardé son entrain même lorsqu'on était perdu dans la banlieue de Freiburg à chercher notre logement ! Je suis très

heureux d'avoir pu bénéficier de son aide talentueuse et d'avoir partagé avec lui d'interminables nuits à coder, pour pouvoir toujours présenter de nouveaux résultats le lendemain à la collaboration. Je lui suis encore plus reconnaissant pour toutes les soirées qu'on a pu passer à manger et/ou à boire, et pour avoir toujours accepté de me suivre dans mes aventures les plus loufoques, comme gravir le Jura enneigé en chaussures de ville, ou partir en bateau dans la grisaille pour se perdre sur une plage immense et vide au Portugal.

CERN has been a major travelling spot for me all these years, and COMPASS a wonderful playground. I would like to sincerely thank the whole collaboration for the physics, and for the fun. I must admit I might have been sceptical at first, facing one of those harsh and turbulent meeting, before I started to realise it was just one acceptable way to testify mutual love and appreciation when carried out by engagement. I would like to thank the overall collaboration for all the knowledge I could collect in COMPASS, and for the responsibility it gives to students. I had a lot of fun on shifts, and I would like to thank Vincent, Moritz, Annika, Riccardo and all the others for their playful company there. I would like to thank Bakur as well for the motivation, the grappa and the prosecco – which, combined, appeared to be most helpful under some circumstances.

I much enjoyed working among my physics group at COMPASS, under the caring watch of our senior physicists: Eva, Andrej, Horst, Andrea and Nicole, whom I thank for their advice and rigour all along the process. I would like to express my most enthusiastic gratitude as well to my fellow students, with whom we shared more than just hard work. I would like to thank Phillip for all the time he spent with us in Freiburg to help us with many parts of the analysis, and for making me discover you can eat a sandwich while walking and still call it a lunchbreak. I would like to thank Matthias for the crazy long run we had in Italy, and for the revenge he took swimming in Geneva lake, as well as for this improbable ice cream we brought back to shift afterwards. I would like to thank my very dear Johannes for being silly with me all along, for this memorable freiburger wine festival, for following me up to the top of many hills, for this incredible week in the states and for these terrible cross-checks. I would like to thank Karolina for her relevance, her enthusiasm towards whatever weird kind of food we have in France, her enthusiasm in general, and her openness. I would like to thank Marketa for her laughs and her incredible pipe. I would like to thank Anatolii for his unbelievable sense of humour, for being so natural, for finding so quick his spot in the team and for helping me to get rid of my broken fridge. Last, I would like to thank Sandro for sharing with me a clear inclination towards sassiness, a certain taste for irreverence and a nonetheless delightful touch of immaturity hidden behind his extremely charming and professional smile. I wish them all a very fruitful time in the collaboration for the end of their PhD!

My account of CERN travels would not be complete if I would forget to mention the many breakfasts at the sun, facing the Jura, in this small and lovely hotel in Segny, when coming back from night-shift. Nights at CERN were definitely one-of-a-kind and I will remember the frightening mist surrounding the path leading to the experiment on October's nights, the glowing eyeballs of the wildlife with which we are sharing the space in Prevessin site, and the numerous people I had the chance to meet around. Among which I would like to thank Pieter, who made me discover the not-so-secret CERN summer-student temple under memorable circumstances

one clear night of September.

Quand je ne passais pas mes nuits au CERN, je les passais souvent à Paris, à chanter ou à boire avec mes camarades du COGE, que je voudrais remercier pour leur compagnie ébouriffante. J'ai ici une pensée très particulière pour Amandine et Perrine ; Lucia, Aude et Fabrice ; Rémy, Grégoire, Jeanne, FrançBat et tous les autres. Ils ont rendu mon existence proprement excitante pendant ces trois années intenses, aussi bien musicalement qu'émotionnellement ! J'aimerais avec eux remercier Léa, Marie et Gabriel qui sont de fidèles compagnons depuis que nous nous sommes rencontrés à la rentrée de Centrale, et avec lesquels je suis heureux de pouvoir continuer à grandir.

Je remercie avec beaucoup de bienveillance Emiko, avec qui j'ai eu la chance d'habiter une bonne partie de l'aventure, et Mathieu qui nous aura rejoint pour un temps. Ils ont été tous deux les colocataires indispensables qui ont su donner à mon séjour parisien des allures de foyer. Je les remercie pour toutes ces histoires partagées au soir autour de la tisane, et pour la musique qu'on aura pratiquée ensemble à des heures indues au grand dam de nos pauvres voisins. Je remercie également Davy, qui aura eu, entre autres charmantes attentions, la patience admirable de reclouer mes fonds de placards alors que nous ne nous connaissions que depuis deux semaines. Je lui suis sincèrement gré des moments que nous avons pu partager et j'espère vivement que nous aurons encore quelques autres belles occasions ensemble à l'avenir.

J'aimerais enfin remercier ma famille, chez qui j'allais me reposer, en banlieue ou en Normandie, lorsque j'étais fourbu de tant de péripéties ; sans eux je n'aurais définitivement pas pu terminer cet exercice difficile. Je remercie mes parents, chez qui j'ai éhontément pris mes quartiers lorsqu'il a s'agit de rédiger cette thèse, pour leurs soins attentifs et les chambres confortables qu'ils continuent de mettre à ma disposition. Je remercie ma petite sœur pour sa cuisine et sa présence à la maison, et surtout pour prendre systématiquement ma défense. Je remercie mon petit frère pour ces éternelles séances de binge-watching et ces vacances à New-York. Je remercie ma grande sœur qui continue de réparer cette petite voiture bleue devenue mythique, et de nous avoir fait un neveu aussi facétieux !

Je souhaiterais pour finir remercier tous ceux qui, même si je ne les cite pas nommément, m'ont inspiré ou m'ont fait vibrer pendant ces incroyables années de découvertes et qui, à leur manière, ont travaillé à faire de moi un meilleur physicien.

CONTENTS

GLOSSARY

All units are expressed in a system where $\hbar = c = 1$.

PHYSICS PROCESSES:

ES Elastic Scattering ($lp \to lp$): process in which a nucleon p is probed by a lepton l in such way that the nucleon is left intact. This process allows to access the nucleon form-factors.

DIS Deep Inelastic Scattering ($lp \to lX$): process in which the content of a nucleon is probed by a lepton, the nucleon is left broken. This process allows to access the Parton Distribution Functions.

SIDIS Semi-Inclusive Deep Inelastic Scattering ($lp \to lXh$): extension of DIS in which a hadron in tagged in the final state. This process allows to access the Transverse-Momentum Dependent parton distribution functions and fragmentation functions of the nucleon.

DY Drell-Yan ($q\bar{q} \to l\bar{l}$): process in which a quark from a hadron and an anti-quark from another hadron annihilate and the resulting photon or Z boson decays to two leptons. This process allows to access Parton Distribution Functions and Transverse-Momentum Dependent parton distribution functions.

DVCS Deeply Virtual Compton Scattering ($lp \to lp\gamma$): process in which the content of a nucleon is probed by a lepton in such way that the nucleon is left intact and radiates a real photon. This process allows to access the nucleon Compton form-factors and GPDs.

HEMP Hard Exclusive Meson Production ($lp \to lpm$): process in which the content of a nucleon is probed by a lepton in such way that the nucleon is left intact and a meson is emitted. This process allows to access the nucleon GPDs as well.

BH Bethe-Heitler ($lp \to lp\gamma$): process similar to elastic scattering with an additional radiative photon emitted by either the incoming or outgoing lepton. This process has the same initial and final states as DVCS and therefore contributes to the experimental cross-section $\mathrm{d}\sigma(lp \to lp\gamma)$.

DISTRIBUTIONS:

FF	Form-Factor
PDF	Parton Distribution Function
GTMD	Generalised Transverse Momentum Dependent parton distribution function
TMD	Transverse-Momentum Dependent parton distribution function
GPD	Generalised Parton Distribution function
CFF	Compton Form-Factor

KINEMATIC VARIABLES:

Denoting k and k' the momenta of incoming and outgoing lepton, $q = k - k'$ the momentum carried by the virtual photon, p and p' the momenta of incoming and recoiling proton respectively and q' the momentum of the real photon emitted out of the DVCS process, one defines:

$Q^2 = -q^2$	hard photon virtuality,
$x_B = \dfrac{Q^2}{2p \cdot q}$	Bjorken x,
$\nu = k^0 - k'^0 = q^0$	lepton energy transfer,
$t = \left(q' - q\right)^2 = \left(p' - p'\right)^2$	nucleon squared momentum transfer,
$\xi \simeq \dfrac{x_B}{2 - x_B}$	parton half longitudinal momentum transfer,
ϕ	angle between the lepton scattering plane and the plane defined by the real and virtual photons,
$s = (p+q)^2 = \left(p' + q'\right)^2$	squared energy available in the centre-of-mass frame,
$W = \sqrt{s}$	energy available in the centre-of-mass frame.

EXPERIMENTS AND FACILITIES:

CERN	European Organisation for Nuclear Research
LHC	Large Hadron Collider
COMPASS	COmmon Muon Proton Apparatus for Structure and Spectroscopy
HERA	Hadron-Electron Ring Accelerator
H1 and ZEUS	Experiment at HERA, in collider mode

HERMES Experiment at HERA, using polarised electron on fixed targets (polarised gaseous targets)

JLab Jefferson Laboratory

CLAS Experiment at JLab, using polarised electron on polarised or unpolarised targets

In their attempt to make sense of the measurable reality, contemporary physicist resort to two main tools: *reductionism* and *unification*, the former hopefully paving the way to the latter. The basic theory of visible matter is organised accordingly, built around fundamental particles that combine and interact throughout certain fundamental laws to recreate the universe as we perceive it.

This theory is named the Standard Model and explains in principle all particle physics. In the Standard Model, interactions are formulated in terms of relativistic quantum field theories based upon gauge invariance. It splits the world into two kinds of particles: the gauge bosons on one side, that convey interactions, namely photons for electromagnetic interaction, W and Z bosons for the weak interaction, gluons for the strong interaction; aside with elementary particles called fermions: leptons and quarks. The Brout-Englert-Higgs boson explains the mass of fermions and the electroweak spontaneous gauge symmetry breaking.

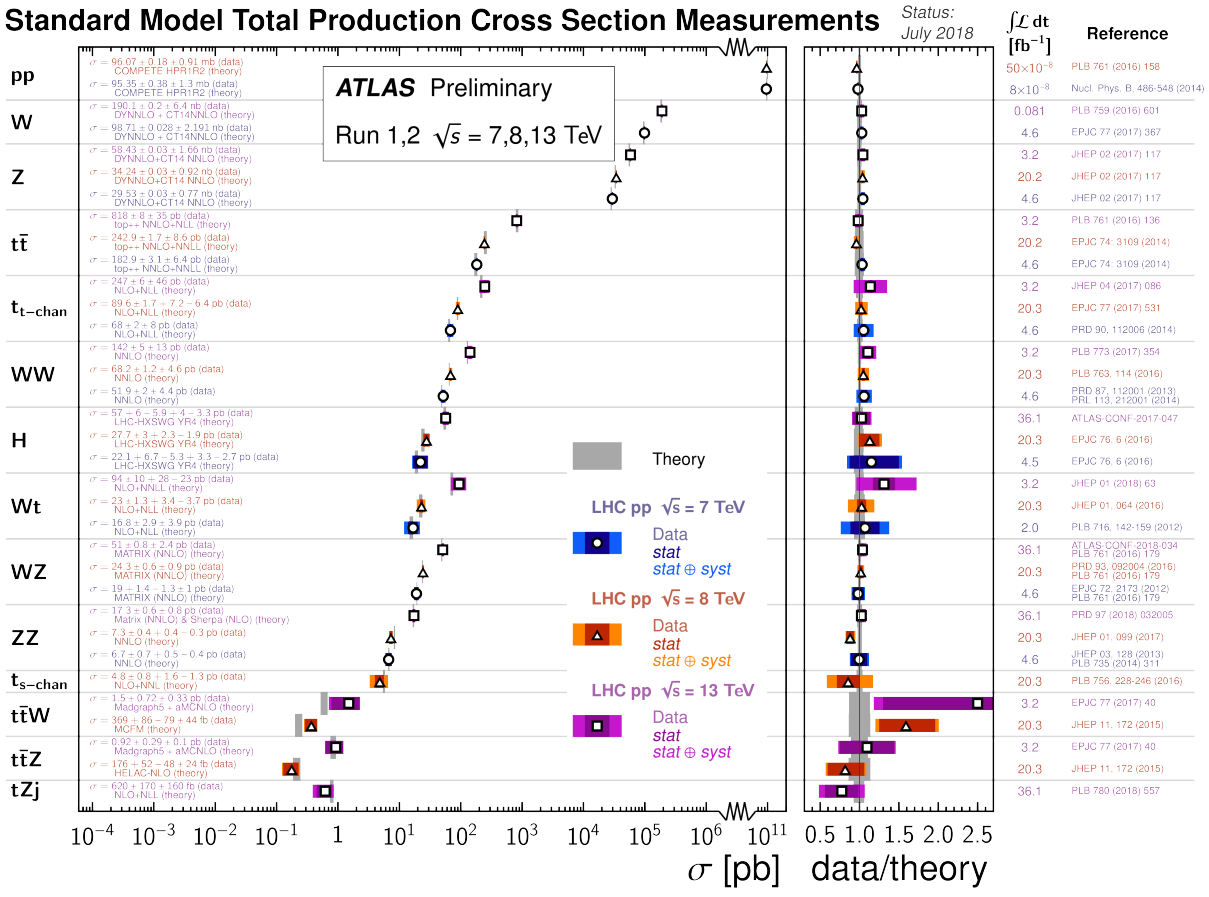

Figure 1: Comparison of cross section measurements and their associated theoretical predictions and uncertainties for a wide class of processes and observables, as obtained by the ATLAS experiment at the LHC. (Fig. from [64]).

The Standard Model is powerful to describe a wide range of phenomena at different energy scales, and it is striking to compare the vast amount of experimental measurements performed in the past fifty years to their theoretical predictions (see figure 1). It is unable, nonetheless, to capture gravitation, and theoreticians are struggling to reunite gravitation with the three other fundamental forces: the electromagnetic, the weak and the strong interactions. The theory describing the first two ones is called electroweak theory, while we refer as Quantum Chromo-Dynamics (QCD) for the last one.

This nice and united model which allows very accurate predictions of how the universe does behave still has a few drawbacks. Hadronic physics - i.e. the study of confined states of QCD - consists in a sort of challenge in that regard. Perfectly integrated within the overall particle physics formalism, it respects both principle stated above: *reductionism*, since it is expressed in terms of elementary particles (quarks and gluons), and *unification*, since these particles behave according to the common and universal rules of the Standard Model. Surprisingly, though, it is presently impossible to derive analytically the macroscopic properties of hadrons, such as mass, out of the quark masses and equations of QCD.

Interestingly, the reductionist paradigm fails as we are unsuccessful to scale-up from quarks and gluons to hadrons. This situation gets even more uncanny when considering that lattice QCD - a numerical implementation of QCD rules and particles - reaches confinement while we do not achieve its formal derivation from the QCD Lagrangian : as if we had written the proper equations but we were unable to use them. That sort of failure is generically and coyly described as *emergent phenomena*, and one can easily get why, denying the physicist a convenient display of reality, it motivates indeed a huge research effort.

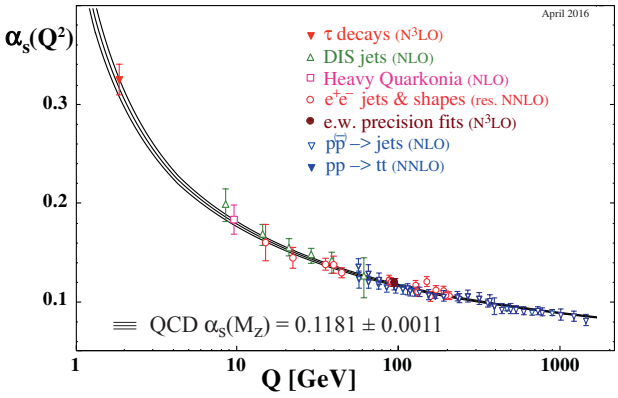

Figure 2: Summary of measurements of α_S as a function of the energy scale Q. The respective degree of QCD perturbation theory used in the extraction of α_S is indicated in parenthesis. (Fig. from [64]).

At least do we understand, a little, why we do fail in this scaling. Part of it is due to the fact that, contrary to QED, the coupling constant of QCD (α_s) cannot always be considered to be 'small'. It is only asymptotically free, that means it tends toward zero for very high energy or small range interaction (< 0.2 fm), while it is close to one for most hadronic phenomena (fig. 2). This forbids any simple use of perturbative expansions for solving problems relative to the internal structure of hadrons, and forces theoreticians to develop more advanced tools to tackle those.

This thesis will attempt to account for the experimental effort lead by the COMPASS collaboration to increase our knowledge in the matter, and I will expose in the following the status of the deeply-virtual Compton scattering (DVCS) cross section measurement performed by the collaboration on the data collected in 2016.

In a first chapter, I will present the theoretical context used to describe hadrons, in particular through the scope of Generalised Parton Distributions and their study *via* deep-virtual Compton scattering. In chapter 2, I will present the experimental apparatus used by the COMPASS collaboration to achieve this measurement. In a third chapter, I will present my work related to the determination of the target position and the time-of-flight recoil proton detector calibration. In a fourth chapter, I will present the analysis of the single-photon production events for the 2016 run. In a last chapter I will present results related to the Monte-Carlo simulation of the experiment and introduce the procedure to extract the DVCS cross section out of the collected data.

1

THE STRUCTURE OF HADRONS

1.1 THE PARTONIC STRUCTURE OF HADRONS

The first indication pointing towards the structural complexity of hadrons have been brought by electron-proton elastic scattering (ES) experiments. They provided direct evidence that the proton was not point-like, but has instead a finite size of around 1 fm [38]. The ES cross section can be parametrised by elastic Form Factors, describing the spatial distribution of charges and currents inside the proton [37]. Our knowledge on the internal structure of the proton was complemented by the systematic study of hadrons spectroscopy. Classifying hadrons in terms of mass, spin, and other quantum numbers gave birth to the theory of quarks. This theory turned out to be confirmed by measurements of deep inelastic scattering (DIS) cross section colliding high energy leptons on protons. The DIS cross section exhibits a behaviour characteristic of an interaction that occurs on free and point-like constituents of the proton, historically called partons which were soon identified to be quarks. This property, called scaling and asymptotic freedom, lead to interpret DIS cross section in terms of Parton Distribution Functions (PDFs) [65] representing the probability density for a parton to carry a given longitudinal momentum fraction of the proton.

While cross sections, structure functions and form factors are observables that are experimentally measured, all distributions used to interpret those measurements, connecting them to QCD degrees of freedom, are not. The extraction of quark and gluon distributions (e.g. parton distribution functions) relies on the possibility to separate the contribution of the probe from the one of the target in measured quantities. This property is called *factorisation* and is a cornerstone of hadronic physics: it makes distributions universal, that means independent of the process throughout which they are extracted. A huge theoretical effort was set-up in the past twenty years in order to connect Form Factors and PDFs, pursuing two main ambitions: construct equivalents of the Wigner distributions for Quantum Field Theories that would parametrise the complete phase-space for the hadron constituents, and ensure such distributions to be independent of the process in which they are measured. I will try here to summarise this enterprise, following mostly the both concise and very comprehensive presentations given by Markus Diehl [22, 24] and Nabil Chouika [20]. I also got inspiration from the PhD theses of my colleagues Maxime Defurne [21] and Cédric Mezrag [49].

Wigner distributions

Wigner distributions are quantum-mechanics extensions of the classical phase-space distributions $f(\boldsymbol{p}, \boldsymbol{q}, t)$, where t stands for the time, $\boldsymbol{p}$ is a generalised momentum and $\boldsymbol{q}$ a generalised position. In classical mechanics, f can be interpreted in a probabilistic way: it provides the density of particles expected to have the position $\boldsymbol{q}$ and the momentum $\boldsymbol{p}$ at time t.

The Wigner distribution for ψ a pure state wave function is defined in [67] as:

$$\rho(\boldsymbol{p},\boldsymbol{q},t) = \int \mathrm{d}^3\boldsymbol{r}\, \mathrm{e}^{-i\boldsymbol{p}.\boldsymbol{r}}\, \psi^*\left(\boldsymbol{q}-\frac{1}{2}\boldsymbol{r},t\right)\psi\left(\boldsymbol{q}+\frac{1}{2}\boldsymbol{r},t\right) \tag{1}$$

This function cannot be considered a probability anymore since it is no longer positive, it is a correlation function that encodes quantum interference. Nonetheless, integrating along one variable allows one to recover the probability density of the other:

$$\int \frac{\mathrm{d}^3\boldsymbol{p}}{(2\pi)^3}\,\rho(\boldsymbol{p},\boldsymbol{q},t) = \psi^*(\boldsymbol{q},t)\,\psi(\boldsymbol{q},t) \tag{2}$$

$$\int \mathrm{d}^3\boldsymbol{q}\,\rho(\boldsymbol{p},\boldsymbol{q},t) = \widetilde{\psi}^*(\boldsymbol{p},t)\,\widetilde{\psi}(\boldsymbol{p},t) \tag{3}$$

where $\widetilde{\psi}(\boldsymbol{p},t)$ is the Fourier transform of $\psi(\boldsymbol{q},t)$.

The Wigner distribution relates the density operator $\hat{\rho}$ through a Wigner transform:

$$\rho(\boldsymbol{p},\boldsymbol{q},t) = \int \mathrm{d}^3\boldsymbol{r}\, \mathrm{e}^{-i\boldsymbol{p}.\boldsymbol{r}} \left\langle \boldsymbol{q}+\frac{1}{2}\boldsymbol{r}\right| \hat{\rho}(t) \left|\boldsymbol{q}-\frac{1}{2}\boldsymbol{r}\right\rangle \tag{4}$$

which allows one to generalise the Wigner distribution to any mixed state $\hat{\rho}$.

The most general relativistic equivalent of Wigner distributions[1] in momentum space is a bi-linear quark correlator [25]:

$$H(k,P,\Delta) = (2\pi)^{-4}\int \mathrm{d}^4 z\, \mathrm{e}^{izk} \left\langle p(P+\tfrac{1}{2}\Delta)\right| \bar{q}(-\tfrac{1}{2}z)\Gamma\mathcal{W}q(\tfrac{1}{2}z)\left|p(P-\tfrac{1}{2}\Delta)\right\rangle \tag{5}$$

With p a hadron state, P, k and Δ three four-momenta, q and $\bar{q}$ two quark field operators, Γ a given Dirac matrix and $\mathcal{W}$ a Wilson line to ensure gauge-invariance between the fields at different points. Momentum assignments are shown in figure 3.

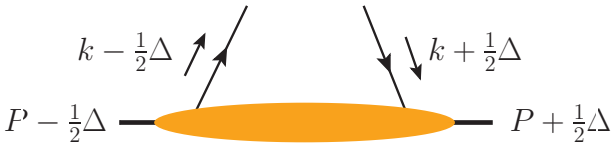

Figure 3: Momentum assignments in the general quark correlation function (eq. 5). (Fig. from [25].)

Factorisation

Whatever experimental process is used to probe the content of the hadron, the direction between the probe and the hadron will always be singled out, hence splitting the space between this *longitudinal* direction and its *transverse* plane, breaking the three-dimension rotational-invariance of the distribution. Even though all quantities discussed in the following are defined in a covariant way, it appears convenient to use a reference frame in which the hadron is moving fast along the positive z-direction in order to allow physics interpretation. Light-cone coordinates are therefore suitable and we will note $v^{\pm} = (v^0 \pm v^3)/\sqrt{2}$ the longitudinal component and $\boldsymbol{v} = (v^1, v^2)$ the transverse components of any fourvector v.

1 A rigorous extension of Wigner distribution can be found in [47].

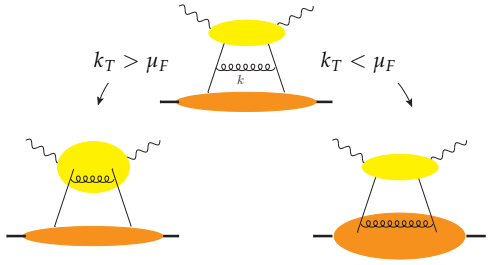

Figure 4: Factorisation consists in separating the hard part of the interaction accounting for *quasi*-free partons (in yellow) from the soft collinear part accounting for spectator partons. Separation is done accordingly to the factorisation scale μ_F: for k_T the transverse momentum component of an internal line, $k_T < \mu_F$ implies the line belongs to the soft part, while $k_T > \mu_F$ implies the line belongs to the hard one. (Fig. from [24].)

Factorisation is the key ingredient to make use of such distribution. Its principle is summarised from ref. [24, 25]. It relies in separating the two scales of our physics: a high momentum scale - named hard part - which translates the probe interaction with one particular parton *v.s.* a soft part - describing the spectator partons of the interaction (see figure 4). In the hard part of the process, quarks and gluons are treated according to perturbative QCD. They are considered on-shell ($k^- = 0$) and therefore distributions are used integrated over k^-. Quark fields are evaluated at time $z^+ = 0$, where they can be interpreted as *quasi*-free partons just before interacting. Depending on the sign of $k^+ - \Delta^+/2$ and $k^+ + \Delta^+/2$ the matrix element of figure 3 describes the emission and re-absorption of a quark, an anti-quark or either the emission or absorption of a quark/anti-quark pair ([25]).

A factorised cross section, under these hypothesis, happens to be the convolution between the soft part of a graph as described above, and a hard scattering part. The different perturbative orders appear in the hard scattering part, while the different twists are selected in the soft part according to Γ. If we note k_T the transverse component of an internal line of momentum k, hard graphs should not contain collinear ($k_T = 0$) lines, and soft collinear graphs should not contain hard line. One has to introduce a factorisation scale μ_F and and integrating applies a cutoff as follows: $k_T > \mu_F$ for the hard part and $k_T < \mu_F$ for the soft part (see figure 4). μ_F, as defined, is the one scale that physically separates what is considered the *object* from the *probe*. It is very important to notice that the hard and soft parts depend upon μ_F in such way that it vanishes in physics observable.

This separation makes the soft part of the graph independent of the process in which it is involved, that is to say it makes it *universal*. In particular, when it comes to relate an experimental process to some matrix elements, the distribution describing the hadron is completely independent of the perturbative order of the hard part of the interaction. The consequence of that is twofold: on one hand, it is possible to measure such a distribution through one channel and then use it as a known function when it appears in another physics context. This is exactly what happens when Parton Distribution Functions or Fragmentation Functions are used at LHC; on the other hand, it complicates further the link between the distribution and the experimental context in which it appears, since it always will do through some convolutions which *do depend* on the order. This complicates much the extraction of these distributions, in particular when they rely on several variables.

GTMDs

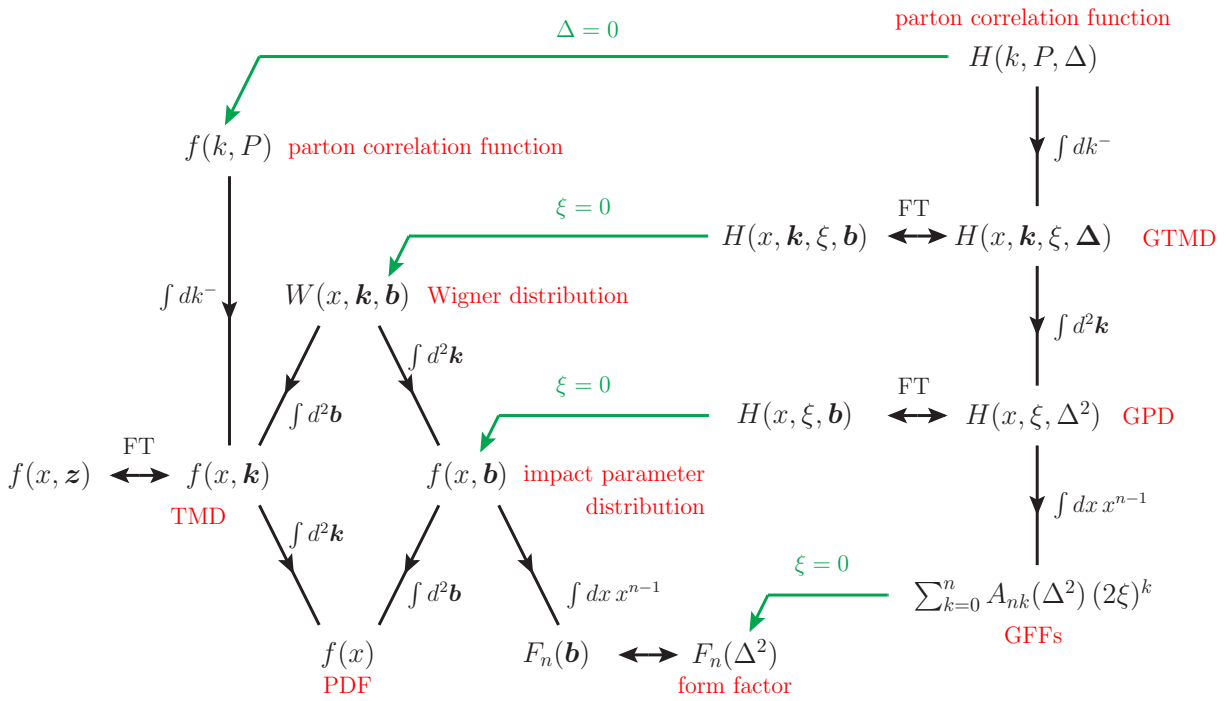

Figure 5: Selected quantities that can be derived from the fully differential two-quark correlation function $H(k, P, \Delta)$ defined in (5). Double arrows marked by "FT" denote a Fourier transform between $\boldsymbol{\Delta}$ and $\boldsymbol{b}$ or between $\boldsymbol{k}$ and $\boldsymbol{z}$. The integrals $\int dk^-$ and $\int d^2\boldsymbol{k}$ cannot be taken literally but must be supplemented with a regularisation procedure. (Fig. from [25].)

One can perform three different kinds of operation on the correlation function of eq. 5 in order to get the distributions as they appear in physics observables. These distributions are displayed in figure 5 and are obtained out of eq. 5 by combinations of:

1. taking the forward limit ($\Delta = 0$).
   In that situation, there is no momentum transfer to the hadron and the function appears in the cross section of inclusive processes evaluated through the optical theorem (the example for DIS will be given in the next section). It is typically the case for Transverse-Momentum dependent parton distributions or PDFs.
   In the opposite situation ($\Delta \neq 0$), the function appears in the amplitude of exclusive reactions and the probed hadron has a different incoming and outgoing momentum.

2. integrating over $\boldsymbol{k}$ and/or k^-.
   The functions integrated over $\boldsymbol{k}$ appear when the physics observable is not sensitive to the transverse momentum of partons. This is typically the case for usual PDFs but also for GPDs.
   If also integrated over k^-, the matrix element has no dependence over the parton momentum anymore. One gets back the usual Form-Factors.

3. Fourier-transform of the transverse component.
   Both the transverse momentum transfer $\boldsymbol{\Delta}$ and the transverse parton momentum $\boldsymbol{k}$ admit Fourier conjugate. It appears that the transverse momentum transfer $\boldsymbol{\Delta}$ is the Fourier conjugate of the average transverse position of partons $\boldsymbol{b} = \sum_i k_i^+ \boldsymbol{b}_i / \sum_i k_i^+$, which, in analogy with the Galilean centre-of-mass of a mechanical system, is the centre of $+$momentum of the hadron.
   Similarly, the average transverse momentum $\boldsymbol{k}$ is the Fourier conjugate of $\boldsymbol{z}$, the position difference, where *average* and *difference* refer to the right and left hand sides of figure 3.

One comprehensive way of exploring the broad ensemble of distributions of figure 5 is to start right after the integral over k^- of the two parton correlator. These distributions are called Generalised Transverse-Momentum dependent parton Distributions (GTMDs).

Note that after integrating over k^-, it is convenient to consider a change of variable as follows: split transverse and longitudinal parts of P, k and Δ; define longitudinal-momentum fractions $x = k^+/P^+$ and $2\xi = -\Delta^+/P^+$; and add on-shell conditions for the hadron: $P\Delta = 0$ and $4P^2 + \Delta^2 = 4m^2$, with m the hadron mass. This allows one to define GTMDs as function of $(x, \boldsymbol{k}, \xi, \boldsymbol{\Delta})$ or, *via* Fourier transform $(x, \boldsymbol{k}, \xi, \boldsymbol{b})$.

It is not clear whether GTMDs appear in any physics process, and they have been mostly studied in theoretical contexts. One can build 16 independent complex-valued GTMDs that encode the most general information one can gather about the internal structure of hadrons in transverse parton position, and both longitudinal and transverse parton momentum. They relate to two sets of eight real-valued distributions that decouple the transverse parton position $\boldsymbol{b}$ (or Δ) from the transverse parton momentum $\boldsymbol{k}$ (fig. 6).

Transverse Momentum dependent parton distributions (TMDs), on one hand, are the forward limit of GTMDs ($\Delta = 0$), they correlate the longitudinal momentum fraction x of the parton with its two-dimensional transverse momentum $\boldsymbol{k}$. TMDs appear experimentally in both Semi-Inclusive Deep-Inelastic-Scattering and Drell-Yan processes, connected *via* an interesting non-vanishing Wilson line that allows to test for the validity of the factorisation.

Generalised Parton Distributions (GPDs), on the other hand, will be discussed in the following section.

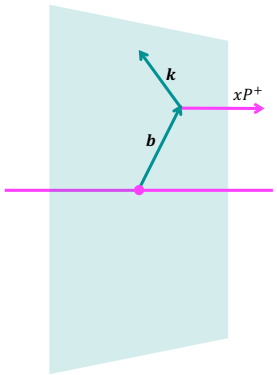

Figure 6: Transverse plane representation of the Wigner distribution variables: impact parameter $\boldsymbol{b}$, transverse momentum $\boldsymbol{k}$ and longitudinal momentum fraction x of partons. Adapted from [20].

1.2 GENERALISED PARTON DISTRIBUTIONS

From this section and in the following, we will consider the probed hadron to be a proton, and m to be the proton mass.

Definition

Generalised Parton Distributions, introduced in [40, 41, 55, 58, 59], are the distributions of interest in this thesis. They are obtained *via* integration over $\boldsymbol{k}$ of GTMDs, hence they do not account for any variation in transverse momentum of the struck parton, and they correlate its *longitudinal-momentum fraction* x with its *transverse position* $\boldsymbol{b}$, or, equivalently, its transverse momentum difference $\boldsymbol{\Delta}$. GPDs provides therefore a tool to access the transverse spatial distribution of partons from the transverse momentum transferred to the proton [22].

For convenience, we will adopt following notations.

- The initial proton state $\left|p(P-\frac{1}{2}\Delta)\right\rangle$ will be noted $|p,s\rangle$ where p is the four-momentum of the proton and s its spin, and respectively $\langle p',s'|$ the final proton state. Note that $P=\frac{1}{2}(p+p')$ does not change definition.
- We will consider $t=(p-p')^2=-\Delta^2=-\frac{4\xi^2m^2+\boldsymbol{\Delta}^2}{1-\xi^2}$, which accounts for both the transverse ($\propto \boldsymbol{\Delta}^2$) and the longitudinal ($\propto \xi^2$) momentum transferred to the proton.

Choosing the light-cone gauge, the Wilson line reduces to unity and one can rewrite the correlation (5) to get the GPDs:

$$F^q_\Gamma(x,\xi,t)=\int\frac{\mathrm{d}z^-}{4\pi}\,\mathrm{e}^{+ixP^+z^-}\,\left\langle p',s'\middle|\bar{q}(-\tfrac{1}{2}z)\Gamma q(\tfrac{1}{2}z)\middle|p,s\right\rangle|_{z^+=0,\,\boldsymbol{z}=\boldsymbol{0}} \tag{6}$$

The corresponding diagram is displayed in figure 7: x is the average momentum fraction carried by the active quark, the leaving parton has a longitudinal momentum $x+\xi$ and the incoming one $x-\xi$, t is the momentum transferred to the proton. q stands for any quark flavour or gluon.

Eight independent GPDs can be defined at twist 2: four of them are chiral-even, they relate incoming and outgoing partons with same helicity; four others, chiral-odd, take into account a helicity-flip of the partons. I will not discuss further chiral-odd GPDs as they will not be of

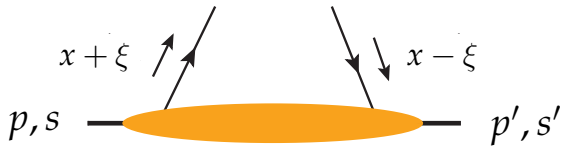

Figure 7: Diagram associated to the matrix element F^q_Γ. Adapted from [25].

interest in this work. Dirac operators for chiral-even GPDs are either $\Gamma = \gamma^+$ or $\Gamma = \gamma^+\gamma_5$ and one decomposes the correlator 6 as follows:

$$F^q_{\gamma^+} = \frac{1}{2P^+}\left[H^q(x,\xi,t)\bar{u}(p',s')\gamma^+u(p,s) + E^q(x,\xi,t)\bar{u}(p',s')\frac{i\sigma^{+\alpha}\Delta_\alpha}{2m}u(p,s)\right], \tag{7}$$

$$\widetilde{F}^q_{\gamma^+\gamma_5} = \frac{1}{2P^+}\left[\widetilde{H}^q(x,\xi,t)\bar{u}(p',s')\gamma^+\gamma_5u(p,s) + \widetilde{E}^q(x,\xi,t)\bar{u}(p',s')\frac{\gamma_5\Delta_+}{2m}u(p,s)\right]. \tag{8}$$

H and E GPDs account for the contribution of unpolarised quarks and gluons and are therefore referred to as unpolarised GPDs while $\widetilde{H}$ and $\widetilde{E}$ account for longitudinally polarised partons and are referred to as polarised GPDs.
H and $\widetilde{H}$ are quantities that conserve the spin of the nucleon while E and $\widetilde{E}$ account for nucleon spin-flip.

Some properties of GPDs

GPDs have non zero value for x and ξ in $[-1,+1]$, and one can distinguish two domains for their study (fig. 8):

- $|x| > \xi$ corresponds to a domain in which a parton/antiparton is emitted and then reabsorbed inside the nucleon. One can consider GPDs to be analogue of PDFs replacing the probability $|\psi_x|^2$ by the correlation $\psi^*_{x-\xi}\psi_{x+\xi}$. In this domain, GPDs evolve in the same way PDFs do, hence we call it DGLAP region.
- $|x| < \xi$ corresponds to a domain in which a quark-antiquark pair is coherently emitted from the nucleon. In that region, GPDs evolve under another set of equations named ERBL, and this domain is named accordingly.

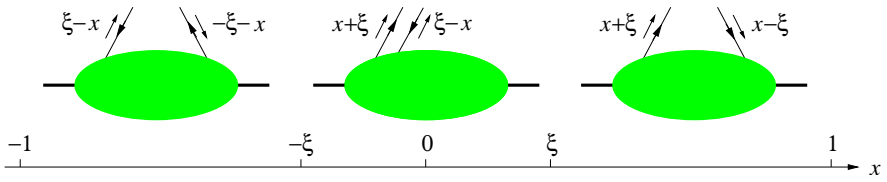

Figure 8: DGLAP (left and right), and ERBL (center) region of GPDs. (fig. from [24])

When $t \to 0$ and $\xi \to 0$, incoming and outgoing proton states coincide, *i.e.* when $|p,s\rangle = |p',s'\rangle$, the GPD H reduces to the usual quark density, similarly, $\widetilde{H}$ reduces to the polarised quark density, for any quark flavour f:

$$H^f(x,0,0) = q_f(x), \tag{9}$$

$$\widetilde{H}^f(x,0,0) = \Delta q_f(x). \tag{10}$$

For gluons one has, given that $x > 0$,

$$H^g(x,0,0) = xg(x). \tag{11}$$

The Mellin-moments of GPDs are related to local operators. The first moments of H, E, $\widetilde{H}$ and $\widetilde{E}$ bring respectively the Dirac (F_1), Pauli (F_2), axial (G_A) and pseudo-scalar (G_P) Form-Factors. They are independent of ξ as a consequence of Lorentz invariance.

$$\sum_f e_f \int_{-1}^{1} \mathrm{d}x\, H^f(x,\xi,t) = F_1(t) \qquad \sum_f e_f \int_{-1}^{1} \mathrm{d}x\, E^f(x,\xi,t) = F_2(t) \tag{12}$$

$$\sum_f e_f \int_{-1}^{1} \mathrm{d}x\, \widetilde{H}^f(x,\xi,t) = G_A(t) \qquad \sum_f e_f \int_{-1}^{1} \mathrm{d}x\, \widetilde{E}^f(x,\xi,t) = G_P(t) \tag{13}$$

$$\tag{14}$$

The second Mellin moments of GPDs can be related to the Energy-Momentum tensor in such way that one can derive the Ji sum-rule [41]:

$$\tfrac{1}{2} \int_{-1}^{1} \mathrm{d}x\, x \Big[H^f(x,\xi,t) + E^f(x,\xi,t) \Big] = J^f(t) \tag{15}$$

$$\int_{-1}^{1} \mathrm{d}x\, \left[H^g(x,\xi,t) + E^g(x,\xi,t) \right] = J^g(t) \tag{16}$$

Where $J^f(0)$ denotes the total angular momentum carried by a parton f. This accounts for both *helicity* and *orbital* parts of the momentum, such that the total proton spin reads:

$$\tfrac{1}{2} = \sum_f J^f(0) + J^g(0) \tag{17}$$

Due to Lorentz invariance, it is possible to derive that, in a more general way, any moment of GPDs can be written as a polynomial function of ξ:

$$\int_{-1}^{1} \mathrm{d}x\, x^{n-1} H^f(x,\xi,t) = \sum_{k=0}^{n} (2\xi)^k A^f_{n,k}(t). \tag{18}$$

This property, known as *polynomiality* of GPDs, is a key feature of both theoretical study and phenomenological modelling of those distributions.

Localisation of partons

Fourier-transforming GPDs from transverse momentum transfer to transverse position leads to an intuitive interpretation when done at the forward limit $\xi = 0$. Under this hypothesis, outgoing and incoming partons have a same longitudinal momentum fraction x and are fully localised on the impact parameter space [15–17, 23]. This allows one to interpret $H^f(x, \xi = 0, t = -\boldsymbol{\Delta}^2)$ as a density probability. Hence one can define an *Impact Parameter* representation of H^f to be

$$q^f(x, \boldsymbol{b}^2) = \frac{1}{(2\pi)^2} \int \mathrm{d}^2\boldsymbol{\Delta}\, \mathrm{e}^{-i\boldsymbol{b}\cdot\boldsymbol{\Delta}}\, H^f(x, \xi = 0, t = -\boldsymbol{\Delta}^2). \tag{19}$$

This distribution yields the probability to find a parton of flavour f having a longitudinal momentum xP^+ at a distance b from the proton *centre of plus-momentum* in the transverse plane. Following that interpretation it is possible to extract the transverse extension of partons inside

the unpolarised proton as a function of x integrating $q(x, \boldsymbol{b}^2)$ over $\boldsymbol{b}^2$. One can therefore define the *average impact parameter* to be

$$\left\langle \boldsymbol{b}^2 \right\rangle_x = \frac{\int \mathrm{d}^2\boldsymbol{b}\, \boldsymbol{b}^2 q^f(x, \boldsymbol{b}^2)}{\int \mathrm{d}^2\boldsymbol{b}\, q^f(x, \boldsymbol{b}^2)} = 4\frac{\partial}{\partial t} \log H^f(x, \xi = 0, t)\bigg|_{t=0}. \tag{20}$$

This two-dimensional transverse extension of partons compares with the one-dimensional one through integration over x, which yields the Dirac (F_1) form factor:

$$\left\langle \boldsymbol{b}^2 \right\rangle = \sum_f e_f \frac{\int \mathrm{d}x \int \mathrm{d}^2\boldsymbol{b}\, \boldsymbol{b}^2 q^f(x, \boldsymbol{b}^2)}{\int \mathrm{d}x \int \mathrm{d}^2\boldsymbol{b}\, q^f(x, \boldsymbol{b}^2)} = 4\frac{\partial}{\partial t} \log F_1(t)\bigg|_{t=0}. \tag{21}$$

Assuming that we can write $H \propto \mathrm{e}^{B(x)t}$, one can study the t-slope of H to extract this average transverse extension of partons:

$$\left\langle b^2 \right\rangle_x = 4B(x) \tag{22}$$

As pointed out by Diehl [22], the resolution of this method is not limited by the Compton wavelength, it is rather controlled by two limiting scales: 1. the hard scattering scale μ will specify *what are the partons probed*, indeed, the partons described by H will always have a finite extension $\sim 1/\mu$ and might appear as composite objects for a higher value of μ; 2. because in an experimental context one will always measure finite values of t, the Fourier transform integral domain will always suffer a cut-off of the order of the maximum momentum transfer measured $|t|_{max}$ and this will *limit the localisation of partons* up to some distance displayed below.

$$\text{distance resolution} \sim \frac{1}{\sqrt{|t|_{max} - \frac{4\xi^2 m^2}{1-\xi^2}}} \qquad \text{parton size} \sim \frac{1}{\mu} \tag{23}$$

It is possible to extend this simplistic 3-D picture of the proton for non-zero skewness ($\xi \neq 0$) GPDs. In that case, $\boldsymbol{b}$ is no longer the Fourier conjugate of $\boldsymbol{\Delta}$ but rather of the transverse component of $D = \frac{p'}{1-\xi} - \frac{p}{1+\xi}$: $\boldsymbol{D} = \boldsymbol{\Delta}/(1-\xi^2)$. As displayed in figure 9, the impact parameter representation of skewed GPDs still allows an intuitive picture of the information they contain: depending on the relative values of x and ξ, they describe either the emission and re-absorption of a parton, or a $q\bar{q}$ pair emission at position $\boldsymbol{b}$. The initial and final state transverse proton positions are relatively shifted of an order $\xi\boldsymbol{b}$. This shift is proportional to ξ which affects the weighting of the partons transverse position between initial and final states. Since this shift is proportional to ξ, it is reasonable to consider that for small values of ξ, $\boldsymbol{b}$ is almost the same between initial and final state, although this assumption is not true for the plus-momenta.

Another important case, addressed by Mathias Burkardt [17], arises when one is considering $\xi = x$. We will see in the next section how this can be of interest. Under that condition, $\boldsymbol{\Delta}$ is not anymore the Fourier conjugate of $\boldsymbol{b}$ but of $\boldsymbol{r}$, the separation between the active quark transverse position and the spectator quark centre of plus-momentum (see fig. 10):

$$\boldsymbol{r} = \boldsymbol{b} - \sum_{spectator\ i} x_i \boldsymbol{R}_i = \frac{1}{1-x}\boldsymbol{b}. \tag{24}$$

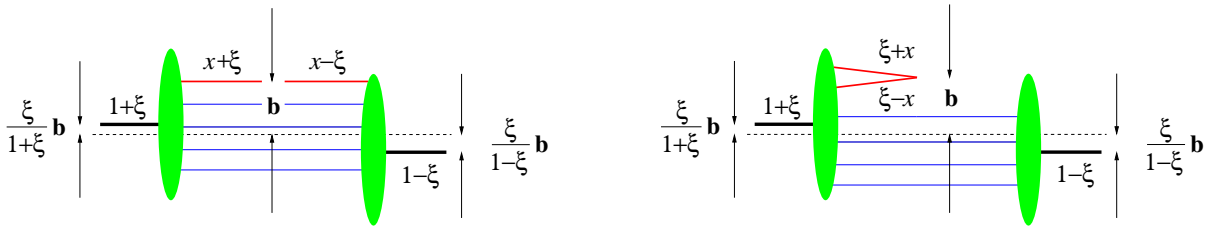

Figure 9: Impact parameter space representation of a GPD at nonzero skewness variable ξ in the regions $\xi < x < 1$ (left) and $|x| < \xi$ (right). ξ is taken to be positive, as appropriate for the processes in which GPDs are known to occur. The overall centre of plus-momentum shifts because of the transfer of plus momentum to the proton. The case $-1 < x < -\xi$ (not shown) is analogous to $\xi < x < 1$, with an antiquark carrying momentum fraction $-x + \xi$ in the wave function and momentum fraction $-x - \xi$ in the conjugate wave function. (Fig. from [23].)

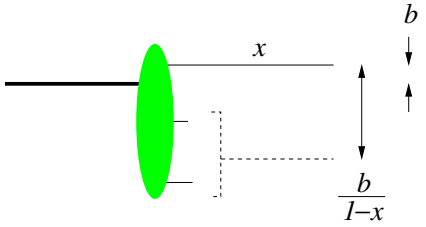

Figure 10: Separation between the active quark transverse position and the spectator quark centre of plus-momentum (fig. from [24]).

One can then rewrite equation 20:

$$\langle \boldsymbol{r}^2 \rangle_x = \frac{\int \mathrm{d}^2\boldsymbol{r}\, \boldsymbol{r}^2 q^f(x, \boldsymbol{r}^2)}{\int \mathrm{d}^2\boldsymbol{r}\, q^f(x, \boldsymbol{r}^2)} = 4 \frac{\partial}{\partial t} \log H^f(x, \xi = x, t)\Big|_{t=0} \tag{25}$$

and its comparison with F_1 will still hold since the integration of H over x yields the Dirac form-factor independently of the value of ξ.
The assumption $H \propto \mathrm{e}^{B(x)t}$ translates, when trading t for $\boldsymbol{\Delta}$ and taking $\xi = x$:

$$t = -\frac{4x^2m^2 + \boldsymbol{\Delta}^2}{1 - x^2}, \qquad H \propto \mathrm{e}^{-B_\perp(x)\boldsymbol{\Delta}^2}, \qquad B_\perp(x) = \frac{1}{1 - x^2} B(x). \tag{26}$$

And it is possible to extract $\langle \boldsymbol{r}^2 \rangle_x$ either from the $\boldsymbol{\Delta}$-slope $B_\perp(x)$, or the t-slope $B(x)$, of H:

$$\langle \boldsymbol{r}^2 \rangle_x = 4B_\perp(x) = \frac{4}{1 - x^2} B(x). \tag{27}$$

This quantity, which relates the partons transverse extension inside the proton to their longitudinal momentum-fraction, reflects the core property of GPDs which is to provide a 3-dimensional picture of nucleons. The experimental determination of this dependence is the subject of this work and we will see in the following section how (some) GPDs can be accessed throughout the Deeply Virtual Compton Scattering process.

1.3 THE DVCS PROCESS

The Deep Virtual Compton Scattering process is the simplest experimental channel to access GPDs. It is an exclusive process consisting in the scattering of a *virtual* photon of momentum q on a proton of momentum p. The final state of the reaction is characterised by a scattered *real* photon of momentum q' and the recoiling proton which has now a momentum $p' \neq p$.

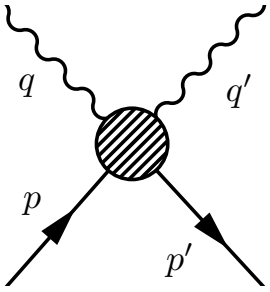

Figure 11: The DVCS process.

Before describing further the Deeply Virtual Compton Scattering, I will reproduce the presentation given by Nabil Chouika [20] of the way Compton amplitudes relate to PDFs and GPDs, thus giving a practical example of factorisation at work for both inclusive and exclusive processes.

Compton amplitudes and factorisation

Compton amplitudes are of the form $\mathcal{A}(\gamma^* p \to \gamma p)$ with one or both photons being virtual. They appear squared in the cross section of different exclusive processes involving GPDs: Deeply Virtual Compton Scattering ($\gamma^* p \to \gamma p$), Time-like Compton Scattering/TCS ($\gamma p \to \gamma^* p$) and Double Deeply Virtual Compton Scattering ($\gamma^* p \to \gamma^* p$). It also appears in the Deep Inelastic Scattering process, parametrised by PDFs, and its squared amplitude relates to the imaginary part of the forward Compton amplitude *via* the Optical Theorem:

$$\mathcal{M}^2_{DIS} \propto \mathrm{Im}\{\mathcal{A}(\gamma^* p \to \gamma^* p)\}. \tag{28}$$

Factorisation of Compton amplitudes have been demonstrated in the Bjorken limit of large Q^2 and finite t and x_B; where we have defined the hard scale to be the (high) virtuality $Q^2 = -q^2$ of the incoming virtual photon, and $x_B = Q^2/2p \cdot q$. Under this hypothesis, the graphs with least lines between hard and soft part are dominant, and other graphs are suppressed in powers of $1/Q^2$. The leading order in α_s and leading twist graphs for DIS, DVCS and TCS are displayed in figure 12.

Denoting k_1 and k_2 the momenta of the quarks coming from and coming back to the hard part respectively, one can define either a symmetric (Ji's, 29) or asymmetric (Radyushkin's, 30) sets of momenta:

$$x = \frac{k_1^+ + k_2^+}{P_1^+ + P_2^+} \qquad \xi = \frac{P_1^+ - P_2^+}{P_1^+ + P_2^+} \simeq \frac{x_B}{2 - x_B} \tag{29}$$

$$X = \frac{k_1^+}{P_1^+} \qquad X - x_B = \frac{k_2^+}{P_2^+}. \tag{30}$$

For this paragraph only, the notations are from Radyushkin (X) and not from Ji (x). The leading order hard scattering part of the handbag diagram have the following contribution, if $\mathcal{P}$ denotes the Cauchy principal value of the distribution:

$$\int \frac{1}{X - x_B + i\epsilon} + \{\text{crossed graph}\} = \mathcal{P} \int \frac{1}{X - x_B} - i\pi\delta(X - x_B) + \{\text{crossed graph}\} \tag{31}$$

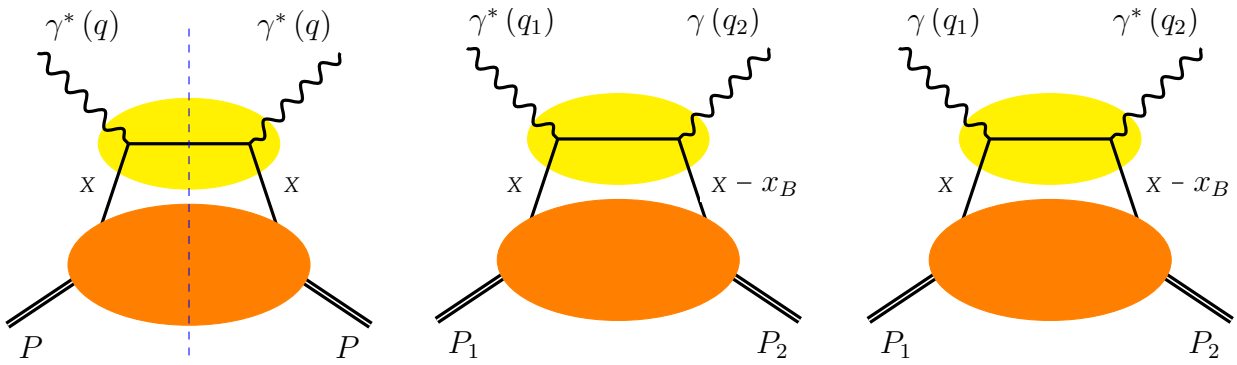

Figure 12: Handbag diagrams for DIS (left), DVCS (center) with $q_1^2 < 0$ and TCS (right) with $q_2^2 > 0$. Adapted from [20].

For DIS, only the imaginary part of the amplitude contributes to the cross section. The convolution of the hard kernel 31 to the PDFs reads:

$$\mathrm{Im}\{\mathcal{A}(\gamma^* p \to \gamma^* p)\} \propto \sum_q e_q^2 \left[q(x_B) + \bar{q}(x_B)\right] + (...) \tag{32}$$

where (...) stands for the crossed graph, polarised terms, higher order and higher-twist contributions. For DVCS, both real and imaginary parts intervene, and the amplitude reads:

$$\mathcal{A}(\gamma^* p \to \gamma p) \propto \sum_q e_q^2 \left[\mathcal{P}\int \mathrm{d}X \frac{H^q(X, x_B, t)}{X - x_B} + i\pi H^q(x_B, x_B, t)\right] + (...) \tag{33}$$

As mentioned in the previous section, factorisation of inclusive processes happens at cross section level since they are obtained *via* the optical theorem, while factorisation happens at amplitude level for exclusive processes. As a consequence, LO DIS structure functions do not have any explicit dependence in X, while their equivalents for GPDs do contain a convolution between X and x_B.

Compton form-factors

Going back to Ji notations, by analogy with DIS structure function, one can introduce so called leading twist Compton Form-Factor (CFF) to be the convolution between a generic hard kernel and twist-2 GPDs:

$$\mathcal{H}(\xi, t, Q^2) = \int_{-1}^{1} \frac{\mathrm{d}x}{\xi} \sum_{a=g,q} C^a\left(\frac{x}{\xi}, \frac{Q^2}{\mu_F^2}, \alpha_S(\mu_F)\right) H^q(x, \xi, t, \mu_F^2) \tag{34}$$

CFFs are observables since they are proportional to the Compton amplitudes, therefore dependence upon the factorisation scale μ_F has to vanish in the right hand side of the equations. This induces a factorisation scale evolution for GPDs which I already mentioned to be either generalised DGLAP or ERBL equations depending on the relative values of x and ξ. As a conse-

quence, for $\xi = 0$, $q(x, \boldsymbol{b}^2)$ fulfils the standard DGLAP equations, which read for the non-singlet combination:

$$\mu_F^2 \frac{\mathrm{d}}{\mathrm{d}\mu_F^2} q_{NS}(x, \boldsymbol{b}^2) = \int_x^1 \frac{\mathrm{d}z}{z} P_{NS}\left(\frac{x}{z}\right) q_{NS}(z, \boldsymbol{b}^2) \tag{35}$$

where P_{NS} is the non-singlet evolution kernel. This accounts for the valence contribution and does not mix with gluons. Singlet combinations are obtained through a matrix equation mixing quarks and gluons GPDs.

The derived quantity of interest $\langle \boldsymbol{b}^2 \rangle_x$ evolves in a similar way [24]:

$$\mu_F^2 \frac{\mathrm{d}}{\mathrm{d}\mu_F^2} \langle \boldsymbol{b}^2 \rangle_x = -\frac{1}{q_{NS}(x, \boldsymbol{b}^2)} \int_x^1 \frac{\mathrm{d}z}{z} P_{NS}\left(\frac{x}{z}\right) q_{NS}(z, \boldsymbol{b}^2) \left[\langle \boldsymbol{b}^2 \rangle_x - \langle \boldsymbol{b}^2 \rangle_z \right]. \tag{36}$$

And so will $\langle \boldsymbol{r}^2 \rangle_x$ with the extended DGLAP equations for $x = \xi$. Nonetheless, reproducing experimentally such evolution, similar to the one visible in DIS, would be a great achievement we are quite far from obtaining. In what follows, scale dependence in μ_F and Q^2 will be implicit.

C^a coefficients are computed perturbatively in α_S and the leading order only accounts for quark lines:

$$C^q = e_q^2 \left(\frac{1}{1 - \frac{x}{\xi} - i\epsilon} - \frac{1}{1 + \frac{x}{\xi} - i\epsilon} \right) + \mathcal{O}(\alpha_S). \tag{37}$$

One has therefore four complex-valued CFFs at *leading-order leading-twist* (fig. 13). The real and imaginary parts of $\mathcal{H}$ and $\widetilde{\mathcal{H}}$ (or equivalently $\mathcal{E}$ and $\widetilde{\mathcal{E}}$) read:

$$\mathrm{Re}\,\mathcal{H}(\xi, t) \underset{\mathsf{LO}}{=} \mathcal{P} \int_{-1}^1 \mathrm{d}x \sum_q e_q^2 \left(\frac{1}{\xi - x} - \frac{1}{\xi + x} \right) H^q(x, \xi, t), \tag{38}$$

$$\mathrm{Im}\,\mathcal{H}(\xi, t) \underset{\mathsf{LO}}{=} \pi \sum_q e_q^2 \left[H^q(\xi, \xi, t) - H^q(-\xi, \xi, t) \right], \tag{39}$$

$$\mathrm{Re}\,\widetilde{\mathcal{H}}(\xi, t) \underset{\mathsf{LO}}{=} \mathcal{P} \int_{-1}^1 \mathrm{d}x \sum_q e_q^2 \left(\frac{1}{\xi - x} + \frac{1}{\xi + x} \right) \widetilde{H}^q(x, \xi, t), \tag{40}$$

$$\mathrm{Im}\,\widetilde{\mathcal{H}}(\xi, t) \underset{\mathsf{LO}}{=} \pi \sum_q e_q^2 \left[\widetilde{H}^q(\xi, \xi, t) + \widetilde{H}^q(-\xi, \xi, t) \right]. \tag{41}$$

It should be noted that gluons do not contribute to LO CFFs, the first gluon contribution arises at NLO or higher-twist. LO CFFs do not depend either on Q^2, the scale dependence appears starting from NLO.

One can relate the real and imaginary parts of the CFFs using a subtraction constant, $\mathcal{C}_{\mathcal{H}}(t)$, which is linked to the integral of the so-called D-term:

$$\mathrm{Re}\,\mathcal{H}(\xi, t) \underset{\mathsf{LO}}{=} \mathcal{P} \int_{-1}^1 \mathrm{d}x \sum_q e_q^2 \left(\frac{1}{\xi - x} - \frac{1}{\xi + x} \right) H^q(x, x, t) + \mathcal{C}_{\mathcal{H}}(t) \tag{42}$$

$$\mathcal{C}_{\mathcal{H}}(t) = \sum_q e_q^2 \int_{-1}^1 \mathrm{d}\alpha \frac{2D^q(\alpha, t)}{1 - \alpha} \tag{43}$$

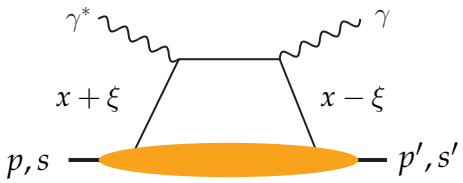

Figure 13: LO DVCS handbag diagram: the hard kernel is reduced to a simple quark line and does not account for gluons. Consequently, LO LT CFFs do not allow for parton helicity flip. Adapted from [25].

The D-term, connected to the QCD energy momentum tensor, relates to the pressure of partons inside the nucleon [48, 56]. This is beyond the scope of this work, but this subject will be experimentally investigated in further analysis lead by our experimental group in Saclay.

Compton Form-Factors are the only experimental way to access GPDs, and they unfortunately do it through a convolution that makes their extraction quite difficult a matter. It is important to understand that equation 42 implies that the most information we can get out of LO CFFs is limited to two quantities:
1. $\mathrm{Im}\,\mathcal{H}(\xi,t)$ which yields the cross-over line $x=\xi$ of GPDs for a few values of x, and $\langle r^2\rangle_x$;
2. $\mathrm{Re}\,\mathcal{H}(\xi,t)$ which can be related to a partially known integral of $\mathrm{Im}\,\mathcal{H}(\xi,t)$ and the D-term.

DVCS cross section

Experimentally, virtual photons are produced by lepton radiation $l \to \gamma^* l$. As a consequence, the DVCS process is accessed through the $lp \to lp\gamma$ channel, and coherently interferes with a pure QED process named Bethe-Heitler (BH). The BH process corresponds to the radiative emission of the real photon by either the incoming or outgoing lepton instead of the proton (fig. 14). The experimental cross section is therefore proportional to the squared amplitude, with $\mathcal{I}$ the interference:

$$\mathcal{T}^2 = |\mathcal{T}_{\mathrm{BH}}|^2 + |\mathcal{T}_{\mathrm{DVCS}}|^2 + \underbrace{\mathcal{T}_{\mathrm{DVCS}}\mathcal{T}^*_{\mathrm{BH}} + \mathcal{T}^*_{\mathrm{DVCS}}\mathcal{T}_{\mathrm{BH}}}_{\mathcal{I}} \tag{44}$$

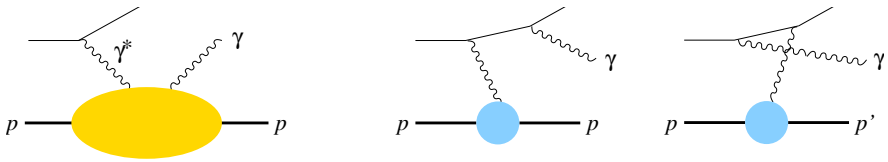

Figure 14: The DVCS (left), and BH (center and right) graphs contribute to the cross section. The proton of the BH graphs are represented by the form-factors F_1 and F_2. (Fig. from [24])

For an unpolarised target, the differential cross section depends upon four kinematic variables: x_B - Bjorken x, Q^2 - photon virtuality, t - the nucleon squared momentum transfer between initial and final states, and ϕ - the angle between the lepton scattering plane and the

plane defined by the real and virtual photons, see figure 15. ϕ is taken to be the 'Trento convention' one [9]. Denoting k and k' the momenta of incoming and outgoing leptons, $q = k - k'$ the momentum carried by the virtual photon, p and p' the momenta of incoming and recoiling proton respectively and q' the momentum of the real photon emitted out of the DVCS process, one has:

$$\begin{aligned} Q^2 &= -q^2 \\ x_B &= \frac{Q^2}{2p\cdot q} \\ t &= \left(q'-q\right)^2 = \left(p'-p'\right)^2. \end{aligned}$$

In the following we will use the abbreviation:

$$\mathrm{d}\sigma = \frac{\mathrm{d}^4\sigma(lp \to lp\gamma)}{\mathrm{d}Q^2\mathrm{d}x_B\mathrm{d}|t|\mathrm{d}\phi}. \tag{45}$$

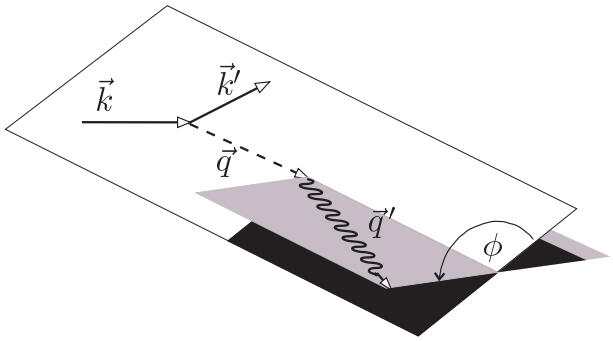

Figure 15: Definition of the angle ϕ as being the angle between the leptonic and the hadronic plane of the DVCS process. Adapted from [68].

This cross section can be decomposed according to ϕ harmonics up to twist-3 with the following contribution for each part quoted above, with λ the lepton polarisation. The complete set of formula can be found in [10]:

$$|\mathcal{T}_{\mathrm{BH}}|^2 = \frac{e^6}{x_B^2 y^2(1+\epsilon^2)tP_1(\phi)P_2(\phi)}\left\{c_0^{\mathrm{BH}} + \sum_{n=1}^{2} c_n^{\mathrm{BH}}\cos(n\phi) + \lambda s_1^{\mathrm{BH}}\sin(\phi)\right\} \tag{46}$$

$$|\mathcal{T}_{\mathrm{DVCS}}|^2 = \frac{e^6}{y^2Q^2}\left\{c_0^{\mathrm{DVCS}} + \sum_{n=1}^{2}\left[c_n^{\mathrm{DVCS}}\cos(n\phi) + \lambda s_n^{\mathrm{DVCS}}\sin(n\phi)\right]\right\} \tag{47}$$

$$\mathcal{I} = \frac{\pm e^6}{x_B y^3 tP_1(\phi)P_2(\phi)}\left\{c_0^{\mathcal{I}} + \sum_{n=1}^{3}\left[c_n^{\mathcal{I}}\cos(n\phi) + \lambda s_n^{\mathcal{I}}\sin(n\phi)\right]\right\}. \tag{48}$$

The BH contribution is exactly calculable within QED and depends on the knowledge of the FFs F_1 and F_2, while the Fourier coefficients of the DVCS part contain the dependence on CFFs. These different harmonics can be selected according to the beam charge and polarisation and it is useful to rewrite [68]:

$$\mathrm{d}\sigma = \mathrm{d}\sigma^{\mathrm{BH}} + \left(\mathrm{d}\sigma_{\mathrm{unpol}}^{\mathrm{DVCS}} + \lambda\mathrm{d}\sigma_{\mathrm{pol}}^{\mathrm{DVCS}}\right) \pm \left(\mathrm{d}\sigma_{\mathrm{unpol}}^{\mathcal{I}} + \lambda\mathrm{d}\sigma_{\mathrm{pol}}^{\mathcal{I}}\right) \tag{49}$$

where the $\pm$ sign corresponds to the charge of the beam. In this work, we aim at extracting the beam charge ($+$, $-$) and spin ($\leftarrow$, $\rightarrow$) sum combination:

$$\mathrm{d}\sigma^{\overset{+}{\leftarrow}} + \mathrm{d}\sigma^{\overset{-}{\rightarrow}} = 2\left(\mathrm{d}\sigma^{\mathrm{BH}} + \mathrm{d}\sigma^{\mathrm{DVCS}}_{\mathrm{unpol}} + \mathrm{d}\sigma^{\mathcal{I}}_{\mathrm{pol}}\right) \tag{50}$$

which integrated over ϕ and after $\mathrm{d}\sigma^{\mathrm{BH}}$ subtraction allows us to access:

$$\begin{aligned} c_0^{DVCS} = \frac{2(2-2y+y^2)}{(2-x_B)^2}\Bigg\{ & 4(1-x_B)\left(\mathcal{H}\mathcal{H}^* + \widetilde{\mathcal{H}}\widetilde{\mathcal{H}}^*\right) \\ & - x_B^2\left(\mathcal{H}\mathcal{E}^* + \mathcal{E}\mathcal{H}^* + \widetilde{\mathcal{H}}\widetilde{\mathcal{E}}^* + \widetilde{\mathcal{E}}\widetilde{\mathcal{H}}^*\right) \\ & - \left(x_B^2 + (2-x_B)^2\frac{t}{4m^2}\right)\mathcal{E}\mathcal{E}^* - x_B^2\frac{t}{4m^2}\widetilde{\mathcal{E}}\widetilde{\mathcal{E}}^*\Bigg\}. \end{aligned} \tag{51}$$

For a small $x_B \sim 10^{-2}$, c_0^{DVCS} is mostly sensitive to the combination:

$$c_0^{DVCS} \propto \mathcal{H}\mathcal{H}^* + \widetilde{\mathcal{H}}\widetilde{\mathcal{H}}^* - \frac{t}{4m^2}\mathcal{E}\mathcal{E}^* \tag{52}$$

A study of two different phenomenological models (KM [44, 46] and GK [31–33] models) shows that one actually expects c_0^{DVCS} to be mostly sensitive to $\mathrm{Im}\,\mathcal{H}$, and that $\mathrm{Re}\,\mathcal{H}$ and other GPDs should have less than a few percent contribution for COMPASS kinematics [5]. It follows that the extraction of $\mathrm{d}\sigma^{\overset{+}{\leftarrow}} + \mathrm{d}\sigma^{\overset{-}{\rightarrow}}$ and its t-dependence allows one to access to the t-slope of H, and the transverse extension of partons $\langle \boldsymbol{r}^2 \rangle_x$ in the proton.

Hard Exclusive Meson Production (HEMP)

In contrast to DVCS, the leading-twist hard scattering sub-processes for HEMP contains hard quarks and gluons exchange. These graphs contain contributions at the same order of the strong coupling constant α_s plus a meson distributions amplitude (fig. 16). It hence provides a

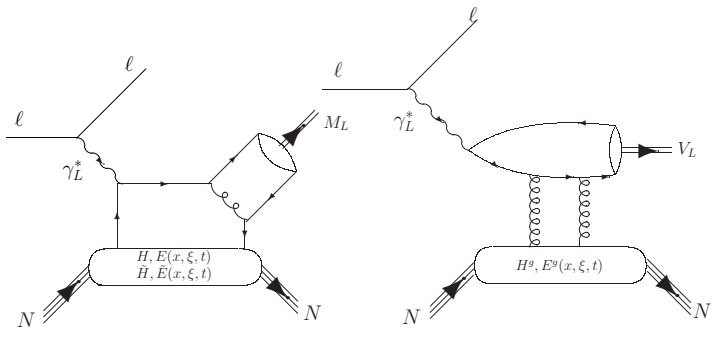

Figure 16: Typical leading-twist HEMP diagrams for the quark ($\gamma_L^* q \to M_L q$) and gluon ($\gamma_L^* g \to V_L g$) sub-processes. The symbol M stands for pseudo-scalar mesons as well as vector mesons while the symbol V stands only for vector mesons. The subscript L stands for longitudinal polarization. (Fig. from [28].)

great tool for the study of gluon contributions. It enables as well, combining results for different mesons in the final state (π^0, ρ^0, ω, ϕ, J/Ψ, ...) , to disentangle flavour dependence of GPDs.

HEMP will appear in two ways in this work:

1. $lp \to lp\rho^0 \to lp\pi^+\pi^-$ will be used for calibrations and data quality assessment purposes, for it is a very clean and well enhanced experimental channel. In this case, it will only be used for its exclusivity kinematic closure.

2. $lp \to lp\pi^0 \to lp\gamma\gamma$ will appear as an inappropriately tagged DVCS event whenever one of the two photons happens not to be detected, adding background to the DVCS signal.

1.4 EXPERIMENTAL STATUS OF THE DVCS CROSS SECTION t-DEPENDENCE

A number of experiments, throughout the world, are trying to extract GPD related information out of DVCS. A recent and extensive review can be found in [68]. In this part, I will exclusively focus on the works related to the extraction of the t-dependence of the DVCS cross section.

Valence region of the proton

Data from HERMES, CLAS and Hall A have been analysed in order to extract locally in each investigated kinematics the imaginary and real parts of the four CFFs from $ep \to ep\gamma$ observables [26, 27]. These fixed target experiments with electron beams (6 GeV at JLab and 27 GeV at HERMES) probed a kinematic domain around $x \sim 0.1$ and $Q^2 \sim 2$ GeV^2. The result mostly depends upon $\mathcal{H}_{Im} = \mathrm{Im}\,\mathcal{H}/\pi = \sum_q e_q^2 \left[H^q(\xi,\xi,t) - H^q(-\xi,\xi,t)\right]$ which is fitted for each (ξ, t, Q^2) bin to an exponential t-dependence:

$$\mathcal{H}_{Im} = A(\xi)\, \mathrm{e}^{B(\xi)t}\,. \tag{53}$$

The figure 17 displays the result of the fit for $\mathcal{H}_{Im}$ for JLab, and the largest part of the error budget comes from the other CFFs contributions to the fit, not from the experimental errors.

The combined result using one HERMES point and seven JLab points of the extraction of $B(\xi)$ and its translation in term of $\left\langle b_\perp^2 \right\rangle_x$ is displayed in figure 18. This conversion is not straightforward in that case, since one needs to take into account that $\left\langle b_\perp^2 \right\rangle_x$ is meant to be the mean squared valence quark transverse extension of the proton, and is therefore extracted at $\xi = 0$ for the valence combination $H^q(x,0,t) + H^q(-x,0,t)$. This is taken into account, under hypotheses described in the article, by a parameter k which should in principle depend on x and ξ but is taken constant on the considered x range ($k = 0.925 \pm 0.025$):

$$\left\langle b_\perp^2 \right\rangle_x \simeq k 4 B(\xi) \tag{54}$$

The model error uncertainty due to this parameter k is small relatively to the error introduced by the fit in figure 18. The large errors are a consequence of the local fit of $Im\mathcal{H}$ and of the other CFFs.

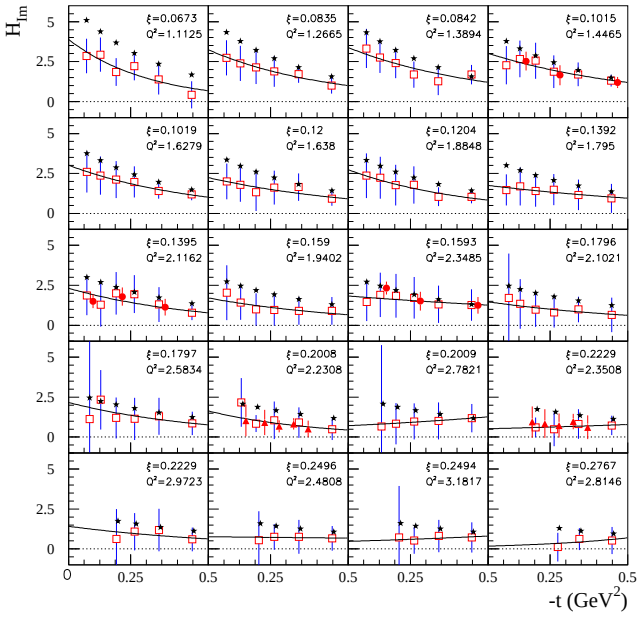

Figure 17: t-dependence of the CFF H_{Im} for twenty (x_B, Q^2) bins from CLAS. Open squares: results of the CLAS σ and $\Delta\sigma$ fit, with the 8 CFFs as free parameters. Solid circles: results of the fit to CLAS σ and $\Delta\sigma$ data, as well as longitudinally polarized target and double beam-target polarized asymmetries, with the 8 CFFs as free parameters. Solid triangles: results of the Hall A σ and $\Delta\sigma$ fit with the 8 CFFs as free parameters. Stars represent the VGG reference-model used to fit CFFs. The solid curve shows an exponential fit of the open squares. (fig. from [26])

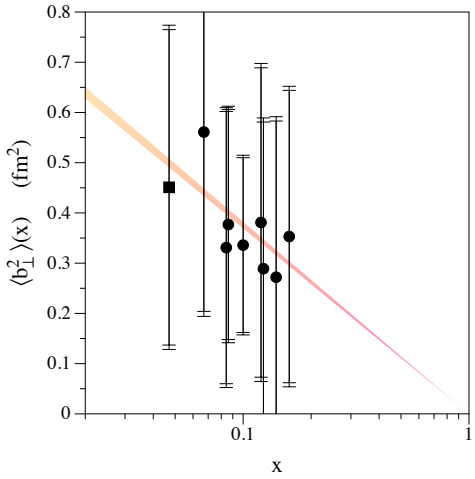

Figure 18: x-dependence of $\langle b_\perp^2 \rangle_x$ for valence (non-singlet) quark combination in the proton. The resulting (small) model uncertainty is shown by the outer error bars. The red band displays the empirical result assuming a logarithmic ansatz $B_0(x) = a_{B_0} \ln \frac{1}{x}$. (Fig. from [26])

Sea quarks and gluons region of the proton

The t-dependence of the DVCS cross section has also been extracted by the H1 and ZEUS collaborations. In these experiments, the collider configuration between a 27 GeV electron and

a 920 GeV proton beam allows the DVCS cross section to become dominant with respect to the BH process. They spanned a wide x_B kinematic range between 10^{-4} and 10^{-2}, for which two-gluons exchange plays an important role in addition to the leading-order quark-photon scattering process. The average Q^2 was between 3.2 and 25 GeV².

The measured t-dependence of the cross section is following a Regge behaviour of the form:

$$\frac{\mathrm{d}\sigma}{\mathrm{d}t} \propto \mathrm{e}^{-B(W)|t|} \tag{55}$$

with $B(W) = B_0 + 4\alpha' \ln(W/W_0)$. B_0 and W_0 are constant, and α' was found to be rather small for DVCS. The t-slope presents no evolution with respect to W and evolves slightly logarithmically with Q^2. $B = 5.45 \pm 0.19_{stat} \pm 0.34_{syst}$ was the averaged value obtained at $Q^2 = 8$ GeV^2 and $x_B = 1.2 \cdot 10^{-3}$. This translates into a transverse extension following:

$$\langle r^2 \rangle_{x_B} \simeq 2B(x_B). \tag{56}$$

The proton transverse extension was measured to be

$$\sqrt{\langle r^2 \rangle_{x_B}} = 0.65 \pm 0.02 \text{ fm}, \tag{57}$$

and compares to:

$$\sqrt{4\frac{\mathrm{d}}{\mathrm{d}t} \log F_1^p \Big|_{t=0}} = 0.67 \pm 0.01 \text{ fm}. \tag{58}$$

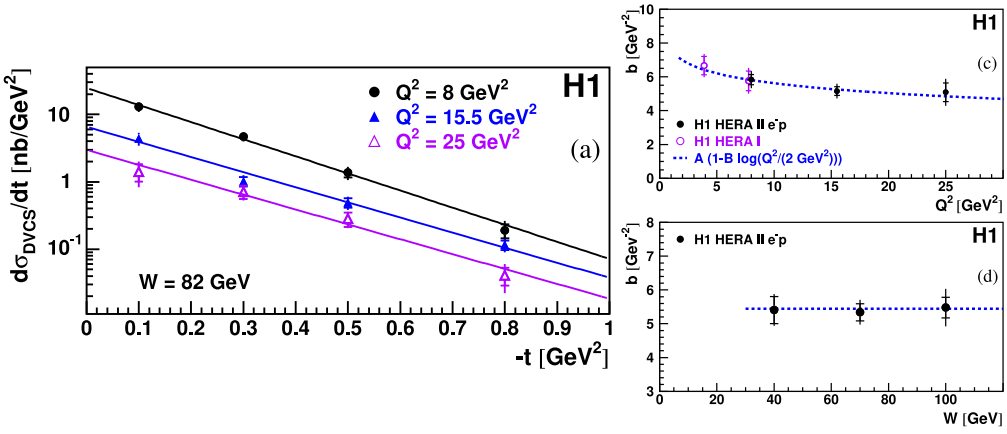

Figure 19: t-dependence of the DVCS cross section for three values of Q^2 (a) and the variation of the fitted values as function of Q^2 (c) and W (d). (Fig. from [1])

In 2012, a test run of two weeks for the COMPASS 2016/2017 program has been analysed [5, 42] for x_B between 0.01 and 0.15. As for HERA experiments, the high energy of the muon beam allows the DVCS process to be dominant with respect to the BH. The extraction of $\langle r^2 \rangle_{x_B}$ was done as described in the previous section: through the ϕ integration of the $\mathrm{d}\sigma^{\overleftarrow{\pm}} + \mathrm{d}\sigma^{\overrightarrow{-}}$ cross section and after subtraction of the Bethe-Heitler contribution. For a mean $x_B = 0.056$ and $Q^2 = 1.8$ GeV^2, the parton transverse extension measured at COMPASS was [5]

$$\sqrt{\langle r^2 \rangle_{x_B}} = 0.58 \ \pm \ 0.04_{\text{stat}} \ ^{+\ 0.01}_{-\ 0.02}\Big|_{\text{sys}} \text{ fm}. \tag{59}$$

This is slightly smaller than the lower x_B measurements of H1 and Zeus, taken at smaller x_B and for comparable $Q^2 < 10$ GeV². These results are displayed in figure 20. The Q^2 sensitivity is displayed for two different models on the right hand side figure, and is of the order of the experimental error bar, allowing us to compare H1, Zeus and COMPASS results.

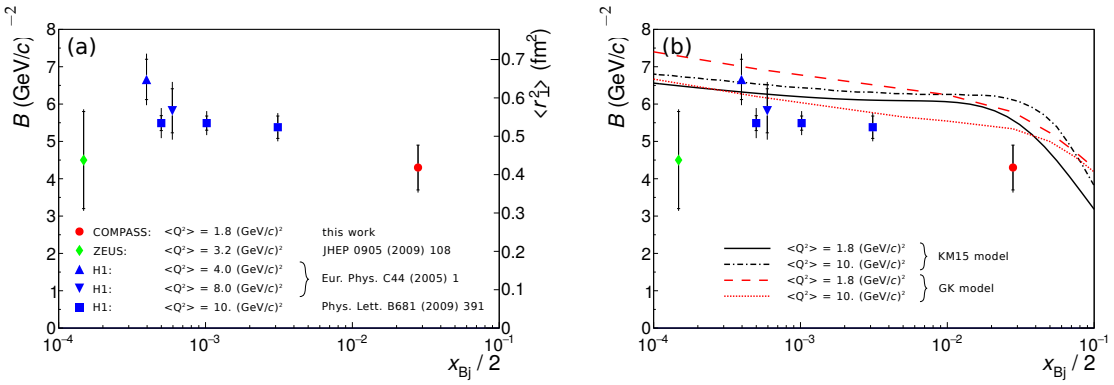

Figure 20: Left: results from COMPASS and previous measurements by H1 [2, 6] and ZEUS [19] on the t-slope parameter B, or equivalently the average squared transverse extension of partons in the proton, $\langle r^2 \rangle$, as probed by DVCS at the proton longitudinal momentum fraction $\xi \sim x_B/2$. Inner error bars represent statistical and outer ones the quadratic sum of statistical and systematic uncertainties. Right: same results compared to the predictions of the GK [31–33] and KM15 [44, 46] models. (Fig. from [5])

1.5 ABOUT THE 'SIZE' OF THE PROTON

The 'proton radius puzzle' in atomic vs elastic-scattering measurements

It happens that it is possible to estimate the charge radius of the proton using two different kinds of physics: atomic physics and spectroscopy of hydrogen atom on one side, probing some levels of energy of the nucleus of which gap is related to its radius, and nuclear physics lepton elastic scattering experiments on the other side. Both fields define the proton radius in the same way:

$$r_E^2 \equiv -6\, G_E(Q^2 = 0) \qquad \text{for atomic physics,} \tag{60}$$

$$r_E^2 \equiv -6\, \frac{\mathrm{d}G_E}{\mathrm{d}Q^2}\bigg|_{Q^2=0} \qquad \text{for nuclear physics.} \tag{61}$$

Nonetheless, the experimental situation appears to be more complex than expected and is well described in [18, 63]. Indeed, both of these methods were agreeing nicely providing a result around $r_E = 0.88$ fm until 2010, when physicists started to probe the lamb shift of muonic hydrogen and got a radius of 0.84 fm. Interestingly, a team from the Max-Plank-Institut reevaluated the Rydberg constant of the standard hydrogen in 2017 and managed to measure a very accurate and similar 0.84-ish value of the radius, quickly followed by an incompatible measurement of similar energy level at Laboratoire Kastler-Brossel around 0.88 fm... Many different atomic physics providing two values for r_E separated from around 4σ. Most recent

nuclear physics data available come from a unique and precise electron-proton scattering dataset from MAMI, and the question of its interpolation is clearly debated [11]. New nuclear physics experimental results should complement soon our knowledge as electron-proton elastic scattering experiments are nearly published for PRad at JLab and under preparation at MAMI, as well as muon-proton elastic scattering at MUSE (PSI) and at COMPASS (CERN). Altogether with new atomic physics experiments, physicists expect to be able to conclude on whether a fundamental difference exists between muon-proton and electron-proton interactions - which would advocate for a deviation from the Standard-Model - or the different results are simply due to insufficient experimental accuracy [50].

Different sizes for the proton

Besides the challenging topics raised by the proton radius puzzle, this discussion leads to another subject of further consideration. The radius defined in equations 60 and 61 is merely a historical convention. It considers the proton radius to be derived from a moment of a three-dimensional spherical symmetric charge density. This derivation is however incorrect as it does not properly take into account relativistic effects [51].

The only relativistically correct derivation has to be done considering a two-dimensional density as considered in the previous sections of this chapter (eqs. 20, 21):

$$\langle \boldsymbol{b}^2 \rangle = \sum_f e_f \frac{\int \mathrm{d}x \int \mathrm{d}^2\boldsymbol{b}\, \boldsymbol{b}^2 q^f(x, \boldsymbol{b}^2)}{\int \mathrm{d}x \int \mathrm{d}^2\boldsymbol{b}\, q^f(x, \boldsymbol{b}^2)} = 4 \frac{\partial}{\partial t} \log F(t) \Big|_{t=0} \tag{62}$$

where F is a given combination of structure functions, and relates to GPDs:

$$\langle \boldsymbol{b}^2 \rangle_x = \frac{\int \mathrm{d}^2\boldsymbol{b}\, \boldsymbol{b}^2 q^f(x, \boldsymbol{b}^2)}{\int \mathrm{d}^2\boldsymbol{b}\, q^f(x, \boldsymbol{b}^2)} = 4 \frac{\partial}{\partial t} \log G^f(x, \xi = 0, t) \Big|_{t=0} \tag{63}$$

where G is the corresponding combination of GPDs.

This definition of impact-parameter, brings as many definitions of "size" as distributions G or F. Hence, when it comes to compare values, one has to be careful and use relevant distributions, since all of these *do not* contain the same information. As an example one can see in table 1 a few values of the impact parameter for different one dimensional Form-Factors.

FORM-FACTOR	DISTRIBUTION	$\langle b^2 \rangle$
F_1^p	$\sum_q e_q^2 \left[q(x_B) - \bar{q}(x_B)\right]$	$(0.66 \text{ fm})^2$
G_E^p		$(0.71 \text{ fm})^2 = (0.66 \text{ fm})^2 + \frac{\kappa_p}{m_p^2}$
G_A^p	$\Delta u + \Delta \bar{u} - \left(\Delta d + \Delta \bar{d}\right)$	$(0.52 \text{ to } 0.54 \text{ fm})^2$

Table 1: Different values of impact parameter for Dirac (F_1^p), Electromagnetic (G_E^p) and Axial (G_A^p) proton Form-Factor. (table from [24])

While all experimental results presented above rely on a similar exponential ansatz for the CFFs t-dependence, they are extracted using different methods and values are summed-up

in table 2. The singlet/non-singlet combinations, the $\xi = 0/\xi = x_B$ configurations as well as all other underlying hypothesis make all these values difficult to interpret and reflect the complexity of the field at the moment.

The only relevant and painstaking way to make a comprehensive analysis of the proton, and hence a proper "tomography" of this particle, would be to collect an extensive amount of data for a wide kinematic range, and proceed through a complete and rigorous global phenomenological analysis, as it has been done the last two decades for PDFs. While some theoretical tools and frameworks are already being developed to achieve these tasks [13, 43–46, 53, 54], we do not have accurate enough data yet. We can hope for such data to be collected at Electron-Ion colliders, as the one projected in the United-States [8], but in the meantime we have to make the most of the available data. The COMPASS 2016/2017 contribution to this vast enterprise will be the subject of the following parts.

CFFS	DISTRIBUTION	x_B	$\langle b^2 \rangle_{x_B}$	REF.
8 CFFs	$\sum_q e_q^2 \left[H^q(x_B,0,t) + H^q(-x_B,0,t)\right]$	$\sim 10^{-1}$	$\langle \boldsymbol{b}^2 \rangle_{x_B} \sim (0.35\ \text{fm})^2$	[26, 27]
$\sim \text{Im}\,\mathcal{H}$	$\sum_q e_q^2 \left[H^q(x_B,x_B,t) - H^q(-x_B,x_B,t)\right]$	$\sim 5.6 \cdot 10^{-2}$	$\langle r^2 \rangle_{x_B} \sim (0.58\ \text{fm})^2$	[5]
$\sim \text{Im}\,\mathcal{H}$	$\sum_q e_q^2 \left[H^q(x_B,x_B,t) - H^q(-x_B,x_B,t)\right]$	$\sim 1.2 \cdot 10^{-3}$	$\langle r^2 \rangle_{x_B} \sim (0.65\ \text{fm})^2$	[1]

Table 2: Different values of impact-parameter for the GPD H, for different x_B and different hypotheses. First line result is dominated by $\text{Im}\,\mathcal{H}$ but the 8 CFFs are fitted, while the two other results are interpreted considering only $\text{Im}\,\mathcal{H}$ contribution. Approximate value of $\langle \boldsymbol{b}^2 \rangle_{x_B}$ in the first line is an order of magnitude of the mean values of figure 18.

2

THE COMPASS EXPERIMENT

The COMPASS (COmmon Muon Proton Apparatus for Structure and Spectroscopy) experiment is one of the CERN fixed target experiments. It is located at the end of the M2 beamline of the Super Proton Synchrotron (SPS), at Prevessin North-Area. Proposed for the first time in 1996, this experiment is a versatile tool for studying the structure and the spectroscopy of hadrons using a high energy beam of about 200 GeV beam.

The COMPASS-II program [30], approved in 2010 as a continuation of the first COMPASS experiment, was primarily aiming at studying the nucleon structure *via* Semi-Inclusive Deep Inelastic Scattering, Drell-Yan, HEMP and DVCS for the extraction of Fragmentation Functions, TMDs and GPDs respectively. Two years of data taking were dedicated in 2016 and 2017 to the DVCS part of the program. I describe in this chapter the apparatus as it was used for those two years.

2.1 THE BEAM

The beam delivered at the M2 beamline can be switched easily from hadrons (mainly protons and pions) to muons. They are generated by collision of the SPS 450 GeV protons on a berylium target (T6) of adjustable length to accommodate for different intensities of the secondary or tertiary beams. The muon beam (μ^-) or anti-muon beam (μ^+) is mostly obtained out of the weak pion decay, favoured with a branching ratio of 0.999877 ($\pi^- \to \mu^- + \bar{\nu}$ or $\pi^+ \to \mu^+ + \nu$) in a process similar to cosmic muon production. A kaon contamination of about 4% of the pion flux contributes also slightly to the muon beam. A pion momentum selection [3] is achieved in a band of $\pm 10\%$ by bending magnets in a 600 meter long tunnel where a large fraction of pions decay into muons. Remaining hadrons are filtered out by some hadron absorber, and the muon beam is then lead to the experimental hall through a 800 meter tunnel. When entering the experimental hall, the muon beam is surrounded by a large halo, primarily composed of muons that could not be significantly deflected or absorbed.

Since the μ^- (μ^+) is produced throughout weak decay, its spin is aligned with (respectively opposite to) to its momentum. This allows for polarised muon beams. The polarisation rate in the laboratory frame is function of the ratio between the pion (or kaon) and the muon momenta. It is given by:

$$P_{\mu^\mp} = \pm \frac{m_{\pi,K}^2 + (1 - 2\frac{E_{\pi,K}}{E_\mu} m_\mu^2)}{m_{\pi,K}^2 - m_\mu^2} \tag{64}$$

where m is a mass, E and energy, and the subscript π, K and μ implies respectively pions, kaons and muons. A beam polarisation of about $\pm 80\%$ is reached by selecting muons and kaons emitted forward in the rest-frame of the decaying meson.

For the analysis presented in this thesis, the beam had a nominal energy of 160 GeV, with a momentum spread of $\sigma p/p = 0.05$ and a spatial spread of about 7 mm at the target centre. To ensure proper analysis of exclusive events, the momentum of each incoming particles is measured upstream the target by the Beam Momentum Station (BMS) which consists in a bending dipole magnet (B6) in between two scintillating-fibre detectors (BM05 and BM06) and four hodoscopes (BM01-BM04), see figure 21. The momentum of particles is then reconstructed out of the bending of their trajectory within a one percent uncertainty.

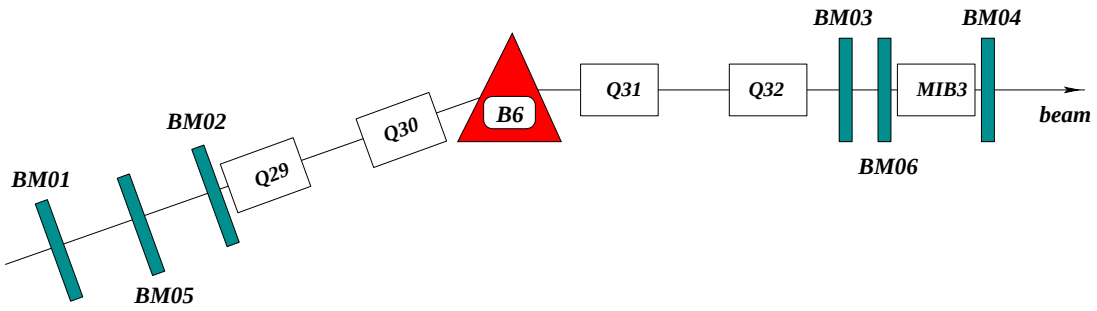

Figure 21: The Beam Momentum Station, fig. from [3].

The typical proton beam flux on T6 was $100(150) \cdot 10^{11}$ protons/spill in 2016 (2017), for a spill length of 4,8 seconds and two spills were delivered every 36 seconds (fig. 22). Using a same T6 target the resulting μ^+ beam intensity is about 2.7 larger than the μ^- beam one. To ensure the best experimental conditions for studying sum and difference of μ^+ and μ^- DVCS contributions we have decided to work with similar beam fluxes. We hence used a T6 target of 100(500) mm for the $\mu^+(\mu^-)$ beams. Typical $\mu^+(\mu^-)$ fluxes were $7.6(6.3) \cdot 10^7$ muons per spill, which is about $1.5 \cdot 10^7$ muons per seconds.

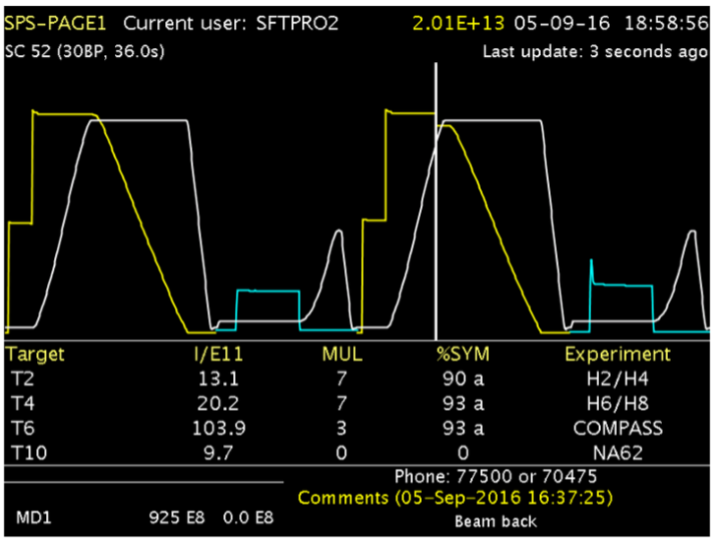

Figure 22: Profile of the proton intensity on T6 (yellow curve) as a function of time, as provided by the SPS control-centre.

2.2 THE TARGET

The target used for the 2016/2017 run is a liquid hydrogen target of 2.5 meter. It has been conceived with a minimal material budget to allow for accurate proton momentum detection, with the requirement to reach a momentum transfer detection $|t|$ as low as 0.07 GeV². Consequently, the cryostat was designed to allow proton to recoil with a momentum down to 270 MeV (fig 23).

Since we aim at extracting a cross section, a key point is to be able to determinate accurately the luminosity. This implies that the target has to be filled with homogeneous density of LH_2, and this requires to identify clearly the fiducial volume that can be used for analysis. I will come back to that point in the following chapter. An extended description of the target can be found in figure 23.

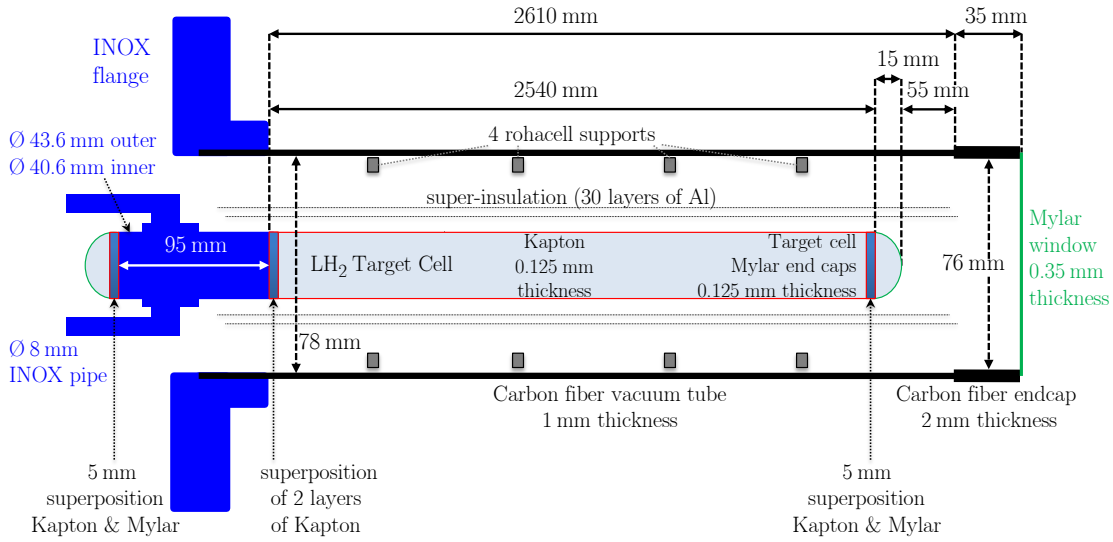

Figure 23: Schematic view of the LH_2 target, fig. from [14].
The target is held inside the carbon tube by the rohacelle supports.

2.3 THE SPECTROMETER

The COMPASS spectrometer is a large acceptance two-stage spectrometer equipped with trackers and particle identification detectors. It has been described in detail in reference [3, 4] and I will only provide the reader with relevant details for the presented analysis. Each stage of the spectrometer is build around a dipole magnet (SM1 and SM2). Momentum of charged particles are reconstructed using the track curvature and the knowledge of the magnitude of the magnetic field. The first part of the spectrometer (LAS on figure 81) is dedicated to particles with large scattering angles up to 180 milliradians and the second part (SAS on figure 81) for small angles below 30 milliradians.

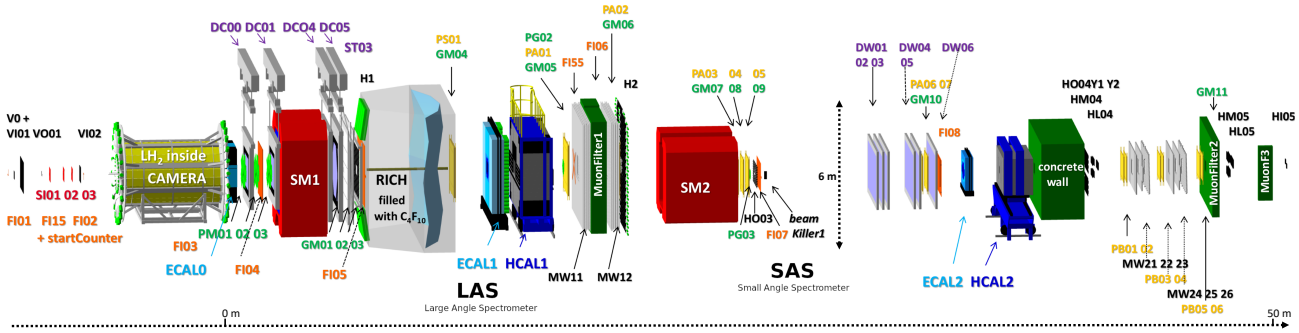

Figure 24: Schematic view of the COMPASS 2016/2017 setup.

Trackers

Charged particles are detected along the 60m of the hall inside many tracking detectors. Different technologies of trackers are used inside the spectrometer, depending on the distance to the beam and the interaction vertex. Close to the beam, one needs both a high rate stability and high spatial and time resolution to disentangle signal tracks from halo. At larger distance to the beam, one does not need such accurate resolution nor rate stability while it is crucial to get large geometric coverage to ensure high acceptance. The different types of trackers used inside COMPASS are summed up in the table 3.

TYPE	$A\,(\mathrm{cm}^2)$	$\delta_x\,(\mu\mathrm{m})$	$\delta_t\,(\mathrm{ns})$
SCIFI	$3.9^2 - 12.3^2$	$130 - 210$	0.4
SILICON detector	5×7	$8 - 11$	2.5
Pixel-GEM	10×10	95	9.9
GEM	31×31	70	12
Pixel-MicroMegas	40×40	70	9
MWPC	$178 \times (90 - 120)$	1600	N/A
DC	$(180 - 248) \times (127 - 208)$	$190 - 500$	N/A
STRAW	280×323	190	N/A

Table 3: The different trackers used in the COMPASS experiment and their properties: A denotes the detector active area, δ_x its spatial and δ_t its time resolutions. The first row of detector types displays very small area trackers: SCIntillating FIbre (SCIFI), SILICON strip (SILICON) and Pixelised Gas Electron Multiplier (Pixel-GEM) detectors. Second row small area trackers: Gas Electron Multiplier (GEM) and Pixel Micro-Mesh GAseous Structure detectors (Pixel-MicroMegas). Last row large area trackers: MultiWire Proportional Chambers (MWPC), Drift-Chambers (DC) and STRAW (STRAW) detectors.

Muon filters

Muons identification lies upon the fact these particles interact very little with matter. This basic principle is implemented as follows: at each end of the two stages of the spectrometer, a heavy absorber is placed in between trackers. We call these muon walls and we consider to be a muon whatever charged particles having coincident tracks right before and right after such absorber.

The first muon wall is placed at the end of the LAS, and consists in four drift chambers placed before and after a 60cm thick iron absorber. Particles deflected with a small angle can pass the muon wall throughout a hole in its centre to access the second stage of the spectrometer. The second muon wall is placed at the end of the SAS and its absorber is made out of 2.4m thick concrete blocks.

Calorimeters

Three electromagnetic calorimeters complete the spectrometer: ECAL0, placed right after the target, allows the detection of large angle photons emitted in the DVCS process before they might get absorbed by all the surrounding material. Intermediate angle photons are detected in ECAL1, placed right after SM1, and a last calorimeter, ECAL2 detects photons with very small angles after SM2 (see fig. 25).

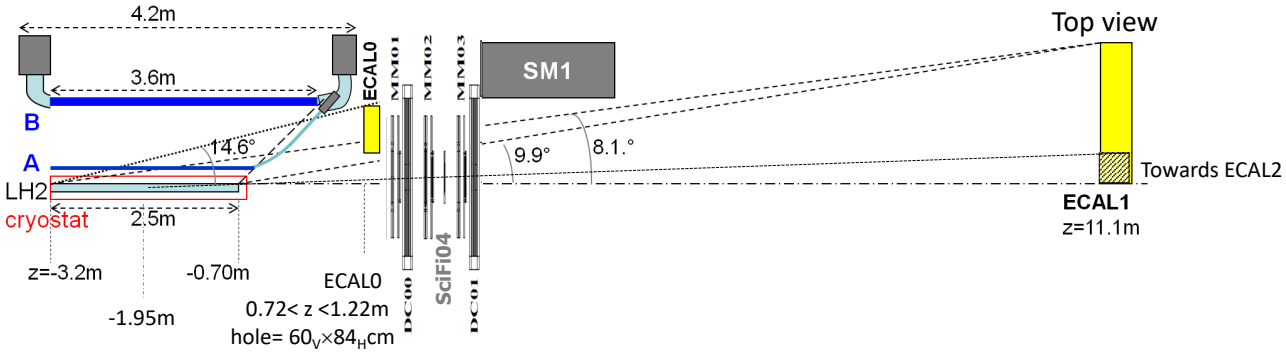

Figure 25: Schematic view of the target area, halved top-view.

These calorimeters are mainly made out of lead glass or shashlik modules. Inside lead-glass modules, photons radiate showers of e^+e^- and the Cerenkov light emitted is collected by photo-multiplier tubes (PMT) and digitised. Shashlik modules are alternating layers of lead and scintillating material. The lead layers produce the e^+e^- pairs which radiate visible light within the scintillating material. Light is collected through wave-length shifting optical fibres and detected by photo-multipliers. The energy deposit in all neighbouring cells is proportional to the total energy of the initial photon and a careful calibration of the cells has to be performed. The cells measure 3.83×3.83 cm², except for the outer part of ECAL1, which consists in 'Mainz' (resp. 'Olga') cells two (four) times bigger for economic reasons (fig. 26).

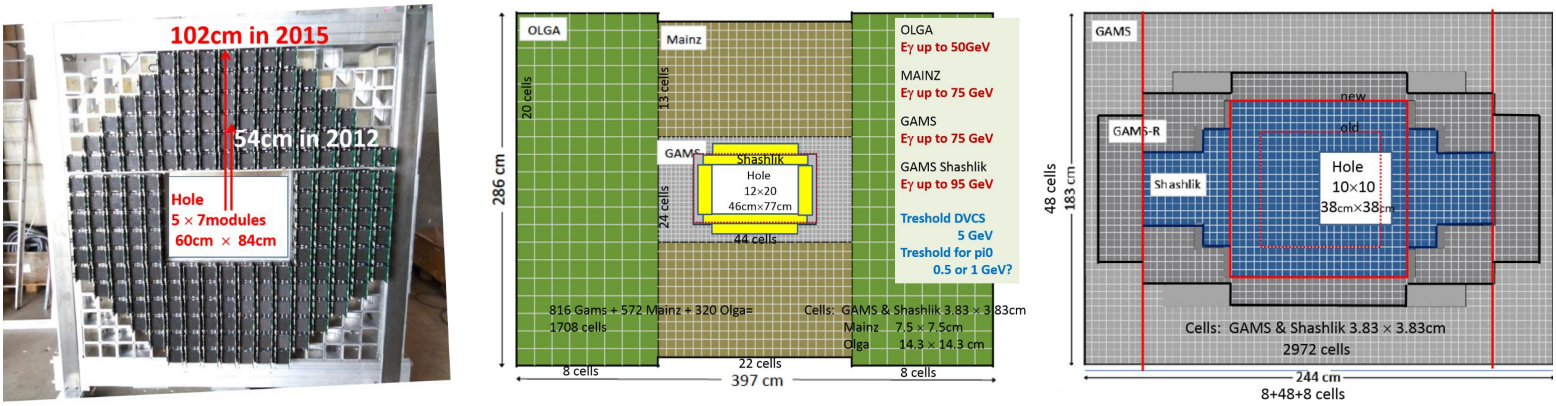

Figure 26: Schematics or photograph of ECAL0 (left), ECAL1 (middle) and ECAL2 (right).

Recoil proton Time-of-Flight detector

The recoiling proton, emitted at large angles (> 45 deg) is detected by a Time-of-Flight (ToF) detector called CAMERA. Placed around the target, it consists in two concentric cylinders of twenty-four scintillator slats each placed respectively at a radial distance of 25 cm and 110 cm respectively from the target axis. Its inner cylinder is called "Ring A" and the outer one "Ring B". Each slat of CAMERA covers 15 degrees around the z-axis. To improve the azimuthal resolution, Ring A is rotated by 7.5 degrees with respect to Ring B (see figure 31). Each end of the scintillators is connected to PMTs *via* long light-guides to minimise the budget material close to the target, and avoid in particular to absorb photons downstream the target (see figure 27).

Ring A scintillators measure $(275 \times 6.3 \times 0.4)$ cm^3, they are build out of BC408, and connected to 107 cm long light-guides bend downstream and 54 cm long upstream the target. They are connected to ET9813B PMTs, having a 51 mm photo-cathode diameter.

Ring B BC408 scintillators measure $(360 \times 30 \times 5)$ cm^3. Light-guides at both ends are bend at 90 deg and are 59 cm long. They are connected to ET9823B PMTs, with 130 mm photo-cathode diameter. The scintillating material BC408 emits light at 430 nm, while the maximum quantum efficiency of the PMTs lies in between 350 and 450 nm.

The principle of such detector is to detect coincident hits in the two rings, and use the timing of such hits to reconstruct the ToF and the Distance-of-Flight of the particle. Knowing those two quantities allows to reconstruct the β of the particle. In our case we are interested at measuring very small momentum transfer for the proton, down to $|t|_{min} = 0.07$ GeV^2. As for the cryostat, material budget for Ring A had to be optimised in order to reach an optimal trade-off between the produced light-yield, which is needed to be high enough for a precise time measurement, and not too much proton energy loss, which would lead a low energy proton to simply stop inside Ring A. For these reasons, Ring A scintillators have been chosen to be 4 mm thick.

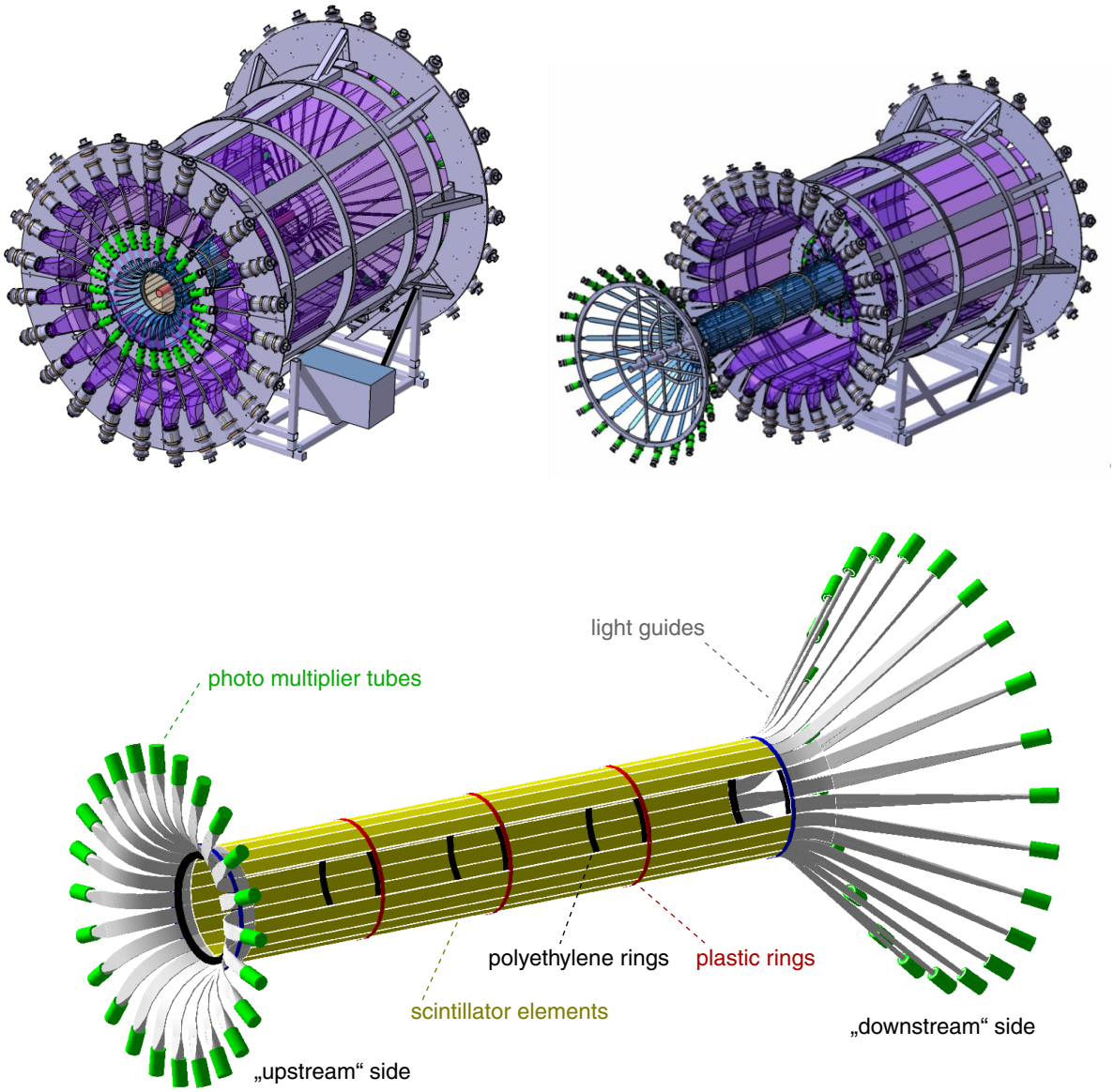

Figure 27: Schematic views of the CAMERA detector, fig. from [29].
Top-left: upstream view, top-right: downstream view, bottom: Ring A detail, plastic rings are suspended to the external mechanical structure by thin nylon wires.

The principle of ToF measurement by CAMERA is presented in figure 28. A charged particle recoiling from the target will create scintillating light through both A and B scintillators. This light will propagate to PMTs at both ends of each slat. PMTs convert photons to an electronic signal, which is sent to GANDALF modules to be digitised. At this stage, both the time-stamps and the maximum amplitude of the signal is sent to the COMPASS Data Acquisition System (DAQ).

To reconstruct a momentum out of this information, one needs to calibrate: the relative timing between the two ends of one scintillator, and the relative timing between an A and a B PMT. I note the first set of constant C_{A_i/B_j} and the second set $C_{A_iB_j}$, where A or B stands for the ring and i or j the identifier of the given slat. Indeed, since Ring A and Ring B are shifted respectively half their angular coverage, there is more than one A slat in coincidence with one

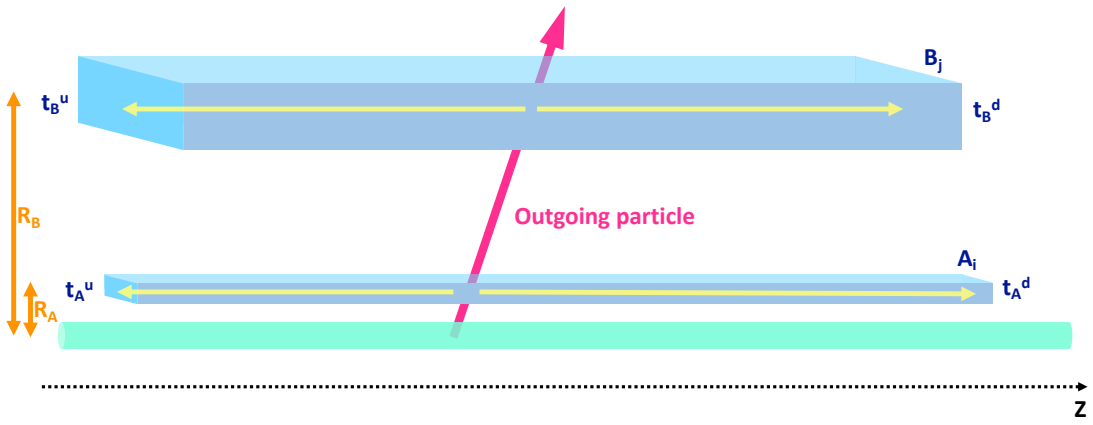

Figure 28: Principle of TOF measurement by CAMERA: a charged outgoing particle (pink track) leaving the target (green cylinder) sparkles inside one ring A and one ring B scintillator (blue parallelepipeds). The light propagates inside the scintillator to reach both ends of it (yellow arrows) and allow PMTs to record time-stamps and amplitudes.

B slat. I note t^u (t^d) the time-stamp given by the upstream (respectively downstream) PMT. Denoting V_{A_i/B_j} the velocity of the light in the scintillator A/B number i or j, one can recover the z-coordinate of the hit following:

$$z_{A_i} = \tfrac{1}{2} V_{A_i}(t^u_{A_i} - t^d_{A_i}) + C_{A_i}, \tag{65}$$

$$z_{B_j} = \tfrac{1}{2} V_{B_j}(t^u_{B_j} - t^d_{B_j}) + C_{B_j}. \tag{66}$$

Making the assumption that slats are parallel, and writing R_{A_i} and R_{B_j} the distance of the slats from the central axis of the cylinders, one gets the Distance-of-Flight of the particle to be:

$$\mathrm{DoF} = \sqrt{\left(z_{B_j} - z_{A_i}\right)^2 + \left(R_{B_j} - R_{A_i}\right)^2}. \tag{67}$$

The Time-of-Flight of the particle is given by the difference between the respective average timing of A and B hits:

$$\mathrm{ToF} = \frac{t^u_{B_j} + t^d_{B_j}}{2} - \frac{t^u_{A_i} + t^d_{A_i}}{2} + C_{A_iB_j}. \tag{68}$$

The velocity β and the momentum p of the detected particle of mass m is therefore simply given by:

$$\beta = \frac{\mathrm{DoF}}{\mathrm{ToF}}, \qquad p = \frac{m\beta}{\sqrt{1-\beta^2}}. \tag{69}$$

We make the hypothesis that the recoiling particle is a proton. This hypothesis is actually confirmed when plotting the measured energy-loss inside Ring B scintillators as a function of the measured β (figure 29).

The calibration of CAMERA detector and the extraction of C_{A_i/B_j}, R_{A_i/B_j}, V_{A_i/B_j} and $C_{A_iB_j}$ will be discussed in the next chapter. Nonetheless, it is important to note that the momentum measured in CAMERA does take into account the energy loss of the particle inside the target. One has to correct for such effect in order to reconstruct exclusive events at the vertex using the Bethe-Bloch formula.

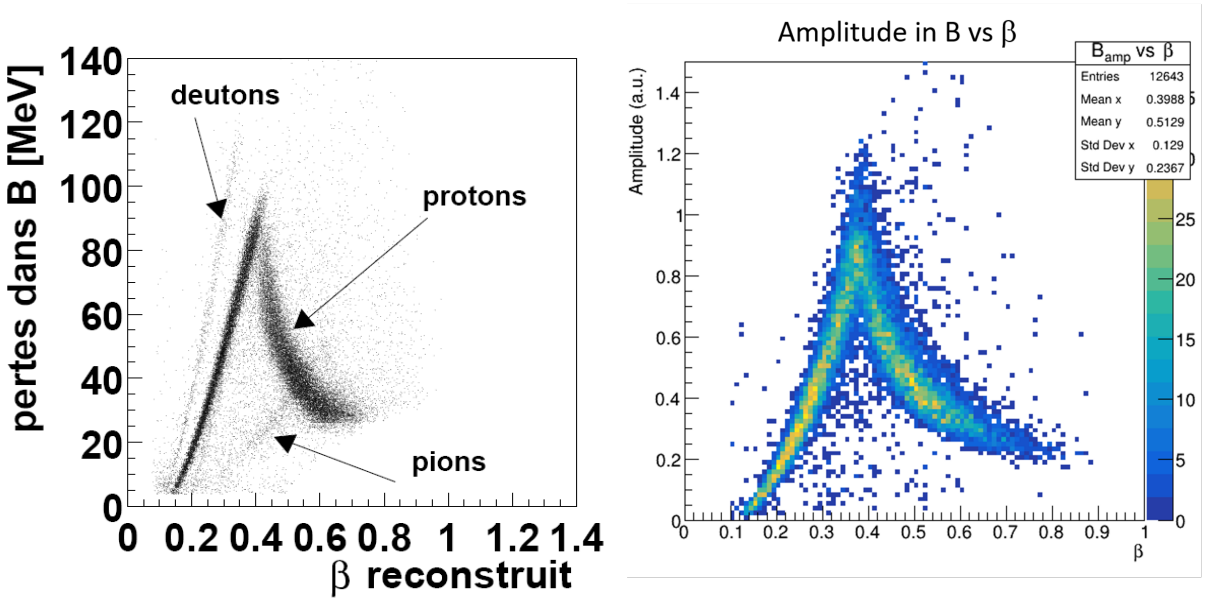

Figure 29: Energy-loss of the recoil particle inside Ring B scintillators as a function of the measured β. Left: prototype used in 2001 around a CH_2 target to demonstrate the separation of pions, protons and deutons [52]. Right: 2016 data using CAMERA.

2.4 THE TRIGGER SYSTEM

COMPASS has many different set-ups that can be implemented depending on the part of its physic program. In 2016/2017, mostly three different types of triggers were at use: the muon, the CAMERA and the random trigger.

The Muon Trigger

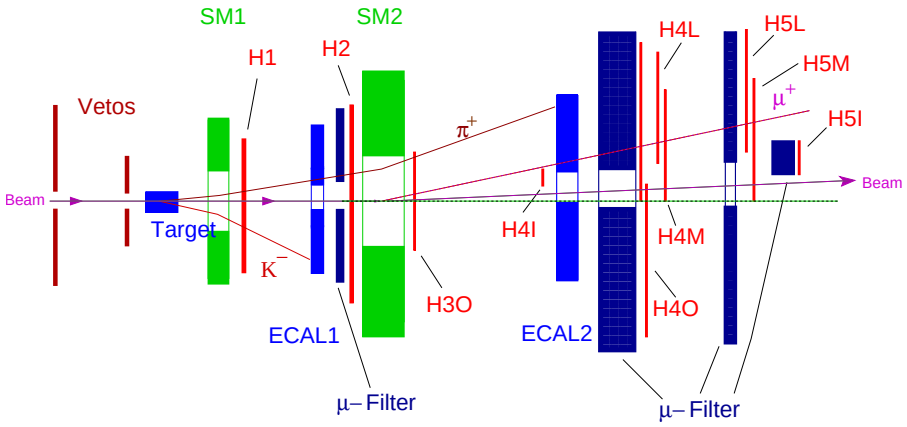

Figure 30: Schematic top-view of the muon trigger system, fig. from [12].

The muon trigger [12] (fig. 30) is the main trigger for the data we will discuss later in this thesis, in particular for the selection of DVCS events. Its role is to detect a diffracted muon out of the target in the widest possible range of Q^2 and x_B. It is implemented following the idea of muon filters described above: it consists on fast hodoscopes planes before and after an absorber, ensuring a geometric and time coincidence for the muon track. Two methods are used to select the relevant tracks:

– *vertical scattering angle measurement:* Events with Q2 > 0.5 (GeV/c)2 are mainly triggered by using the scattered muon information only. The muons are measured in two horizontal scintillator hodoscopes in order to determine the projection of the muon scattering angle in the non-bending plane and to check its compatibility with the target position (vertical target pointing). This is the method used for the Middle Trigger (H4M and H5M), the Outer Trigger (H30 and H4O) and the LAS trigger (H1 and H2) reaching increasing values of Q^2.

– *energy loss measurement:* At low Q^2, in the quasi-real photon regime, the muon scattering-angles is close to zero so that target pointing does not work any longer. These events are selected by measuring the energy loss with two vertical scintillator hodoscopes using the bending of the muon track in the spectrometer magnets. A careful rejection of background processes has to be done. This is the method used for the Ladder Trigger (H4L and H5L).

To suppress events due to halo muons, a veto system is added to the trigger system.

The Random Trigger

The random trigger is a trigger completely decoupled from the experiment itself. It consists in some $^{22}_{11}$Na radioactive source placed far away from the experimental hall. β^+ decay of the source generates a positron which annihilates with some electrons into two back to back photons of 511 keV. When these photons are detected by the system of two coincident scintillators placed around the source, a trigger signal is sent to the DAQ. This trigger is of great importance when it comes to measure the beam flux as it provides random rates independent from the experiment.

The CAMERA Trigger

A last trigger type is of use for the data we will discuss, and is driven by CAMERA. It consists on recording the data whenever some geometrically coincident sectors of both Ring A and Ring B are activated in a time window of $[-5, 40]$ ns. (figure 31). This requires to be able to continuously record time-stamps for all CAMERA PMTs and have fast enough data transfer from front-end electronic to the trigger electronic.

At first, this trigger system was thought of as an additional trigger for protons, and some additional trigger stage using the amplitude of the collected signal should have been added. This was not done, but this trigger mode was still used to collect some cosmic muons and elastic pion data I will discuss in the following section.

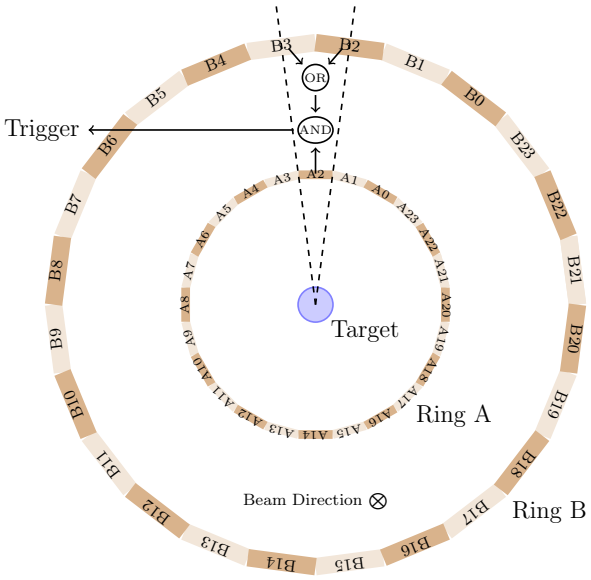

Figure 31: Illustration of the CAMERA trigger principle, fig. from [42].

2.5 DATA ACQUISITION AND RECONSTRUCTION

The DAQ of COMPASS is built around a modular design and is able to readout over 250000 detectors channels (fig. 32). The first stage of the electronics is placed very close to the detectors themselves and transform analogical signals into digital ones. Most of it is based upon Time to Digital (TDC) or Analogical to Digital (ADC) converters.

The second stage of the DAQ manages the on-clock readout of the first stage, it is connected to the trigger control system and works at a global 38.88 MHz frequency. This stage collects data from ADCs and TDCs in some time-window around the trigger signal and serialises it. It can be realised either on the same, or a different module as the first stage.

Serialised data is already organised on an event-by-event basis and is transferred through S-LINK protocol. It is either transferred directly to the "spillbuffer computers" of the DAQ or multiplexed before transfer.

Spillbuffer computers receive this data and pass it to "event builder computers" which gather the entire information from all detectors contained in a single event before sending it into one data package to the CERN main area for long term storage.

This raw data, stored on tape on the CERN Advanced STORage Manager (CASTOR), is then piped into CORAL, our track and vertex reconstruction software, which is able to handle particle identification as well. At this stage, track reconstruction is done using a Kalman filter algorithm, and charged tracks are combined in some vertex fitting procedure. Calorimeter clusters are reconstructed. All this reconstructed data, along with uncertainties associated to the reconstruction fit, is stored in the mDST (mini Data Summary Tree) format readable by the ROOT software. Analysis of mDSTs are done using a C++ library called PHAST, developed by our collaboration in order to conveniently access data inside mDST as produced by CORAL.

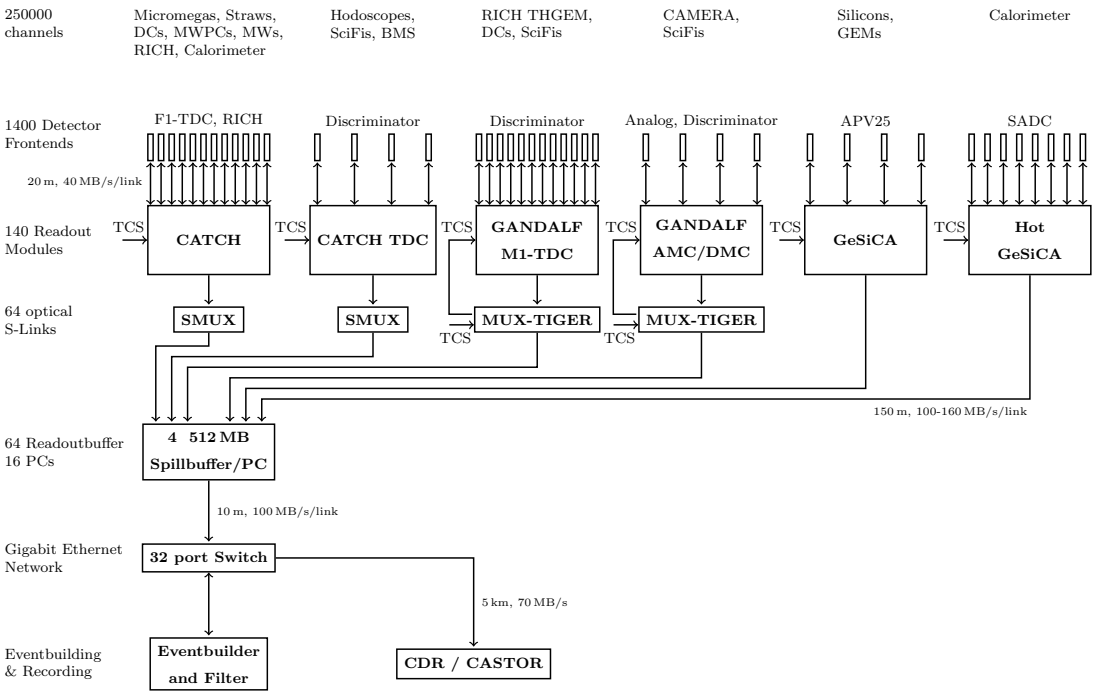

Figure 32: The different stages of the COMPASS Data Acquisition System, fig. from [3].

3

ABOUT CALIBRATIONS AND OTHER PREPARATORY WORKS

Calibrations are an important preparatory step before it is possible to consider any physics-wise relevant data when using complex apparatus. Although calibrations are supposed to occur *before* we 'do physics', they still require most of the time to actually look at simple physics processes through the apparatus. For the DVCS analysis case, the main experimental calibration operations and preparatory analyses could be grouped as follows: calibrations of trackers and triggers, alignment of the spectrometer, calibration of the Beam-Momentum Stations, beam and detectors stability along the run, determination of the target position, calibration of CAMERA, calibration of Electromagnetic Calorimeters. During my PhD, I worked out two of these tasks: the determination of the target position and the calibration of the CAMERA detector.

3.1 DETERMINATION OF THE TARGET POSITION

The precise determination of the target position is of importance for two reasons in our experiment: first, we want to select events that are coming from the liquid hydrogen of the target and not its surrounding material, second, we need to know accurately the fiducial volume of the target to compute the corresponding luminosity in order to access the DVCS cross section. This part of the work was done following the method developed for the 2012 data.

Principle

The detection of the target-cell borders relies on the fact that the kapton containing the liquid hydrogen is more dense than the liquid hydrogen itself (see fig. 33). More interactions should occur at the borders of the cell, as the halo of the beam hits the kapton cell. This phenomenon leads to an increase of the density of interaction vertices reconstructed in the kapton part of the target. The cell is easily detected since on its outside the cryostat is mostly filled with vacuum, while on its inside the beam itself is centred away from the kapton. Hence it is possible to reconstruct the geometry of the target *via* a vertex tomography, using the spectrometer and reconstruction software.

It is important to note two things about that method: first, this can only work if the halo of the beam is wide enough to illuminate the entirety of the target cell. This a nice way to take advantage of the wide-spread COMPASS muon beam in that case. Second, this relies on the detection and reconstruction of the tracks in the spectrometer and their interpolation to the target. It is therefore conditioned to the state of the alignment of the spectrometer and the reconstruction software.

This constraint points us to the requirements of the corresponding event selection: we want the most accurate possible interpolation for the vertices position and this can be achieved selecting vertices out of which more than one track scatters (hence we have three tracks at least

contributing to the fit: the incoming one, and at least two outgoing ones). We also want high statistics, since we want a 3-dimensional reconstruction of the target-cell. Most of the statistics in our experiment happens to be at low Q^2, so I allow Q^2 to go down to 0.1 GeV^2. I cut on $0.05 < y < 0.95$ and the data includes all possible triggers.

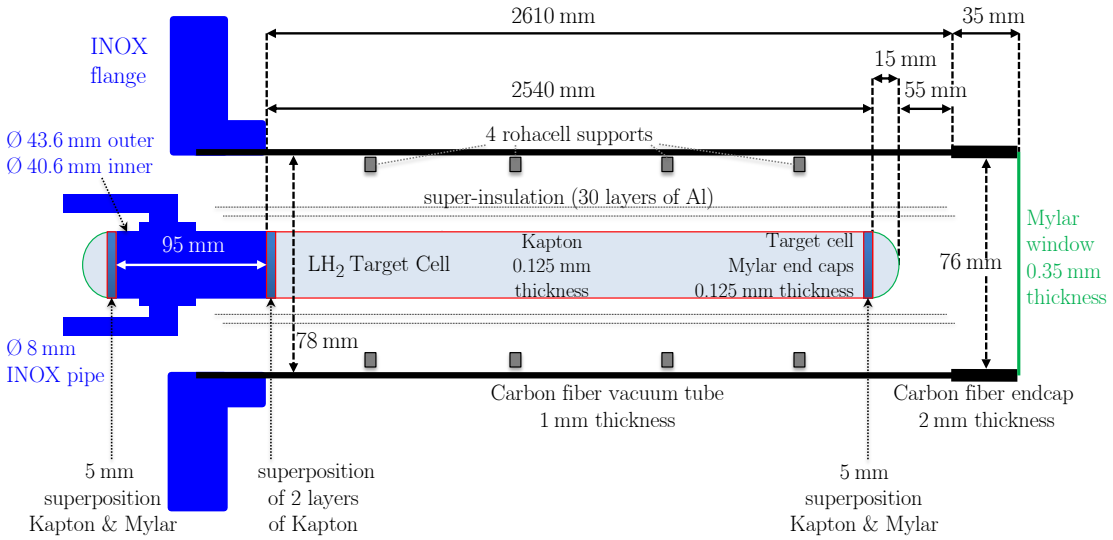

Figure 33: Schematic view of the LH_2 target, fig. from [14].

Fitting procedure

A first plot of the z position of selected vertices allows us to see where is the target along the z-axis (figure 34). This plot is accurate enough to let us see the mylar window situated at the downstream end of the cryostat ($z = -62$ cm). I split the data in 10 cm slices in the region of interest and then display for a given slice the (x, y) distribution of vertices (top-left figure 36). Borders of the kapton-cell are clearly visible by eye and form an almost perfect circle. To be able to automatically and efficiently fit circles on each slice is a challenging matter and one has to proceed step by step. First as it is more convenient to fit a sinusoid instead of a circle, a polar transformation of the distribution allow for such trick (figure 35).

To ensure the proper fit of the cell itself, the fit function is not applied to the transformed vertex distribution itself but to its gradient, and is initialised in the ϕ region where the signal is less ambiguous (bottom-left figure 36). The fit is then redone a second time over the entire ϕ-axis, and displayed in green on top of the vertex distribution (bottom-right figure 36). As a verification, the transformed result of the fit, expressed as parameters (x, y, R), with (x, y) the coordinate of the centre and R the radius of the target-cell, is plot on top of the original vertices distribution (dark blue points on top-left figure 36).

This operation is done for each slice along the target length, starting from the one in the centre of the target and going toward both ends, every time initialising the fits with the previous adjacent (x, y, R) values. This is essential as both the upstream and downstream ends happen to been quite hard to fit. In particular, at the upstream end, the distribution of vertices is blurred by the inox part that maintains the kapton-cell (middle blue piece in figure 33).

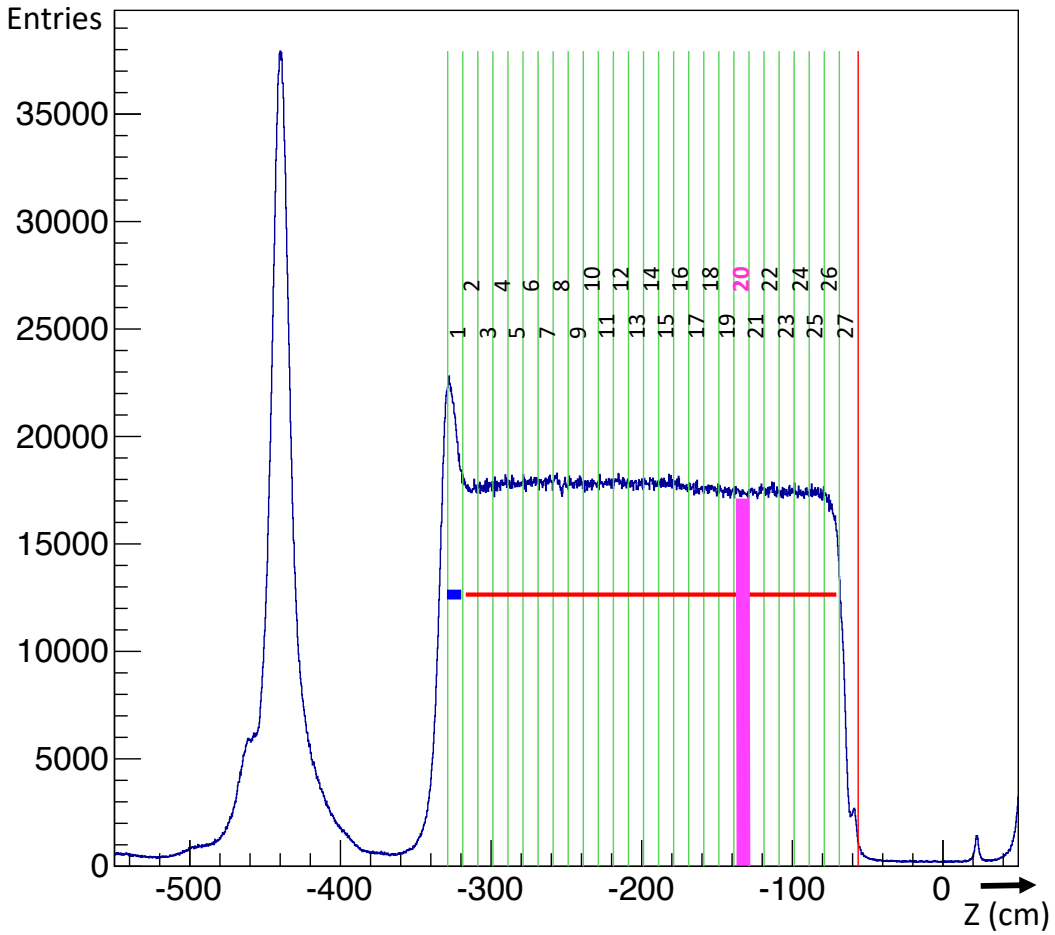

Figure 34: Profile of the distribution of events along the Z-axis and definition of 27 bins of 10cm along the target.

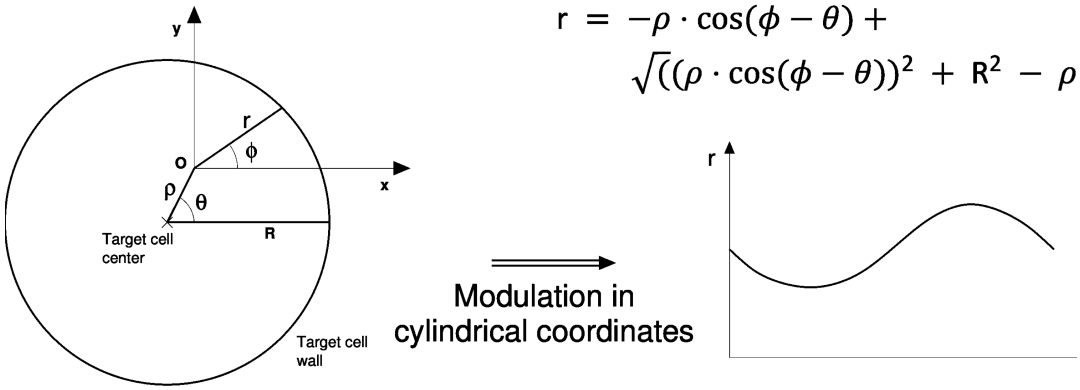

Figure 35: Description of the wall and centre of the target cell in the plane perpendicular to the z-axis using cartesian and polar coordinates.

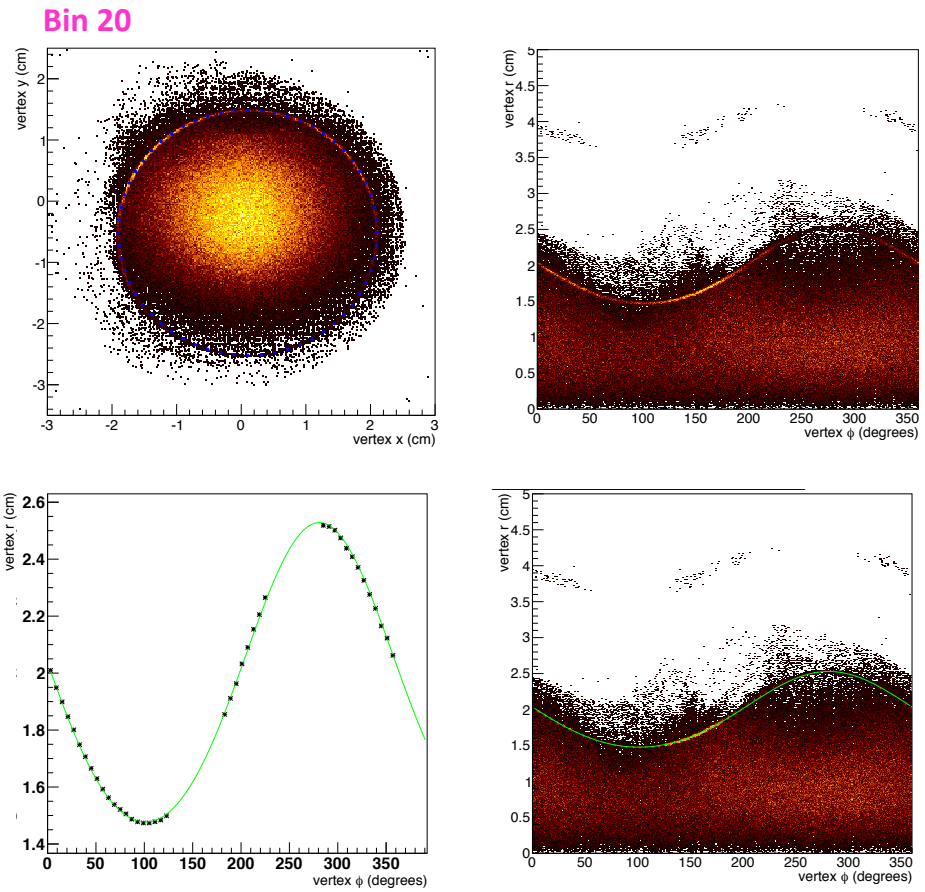

Figure 36: Top-left: Distribution of vertices for bin 20 in Cartesian coordinates (x,y).
Top-right: Distribution of vertices for bin 20 in polar coordinates (r,ϕ).
Bottom-left: Maximum values of the gradient of top right figure fitted with a sinusoid.
Bottom-right: Fit in green superimposed with the distribution of vertices in polar coordinates (r,ϕ).
The result of the fit transformed in Cartesian coordinate is superimposed to the data in top-left figure (small dark blue dots).

Results

The tomography of the target along with the fit is displayed in figure 82. It is easy to see both the border of the kapton-cell and the horizontal interface between the liquid and the gaseous hydrogen.

The values of each fitted parameter as a function of z are displayed in figure 83. One can see that the radius is constant over z and $R_{target} = 2 \pm 0.005cm$. The x-coordinate (horizontal coordinate) of the centre of the target oscillates around zero but only of 1 mm on a 2.4 m length. The y-coordinate drops down intentionally in order to keep the gaseous hydrogen at the beginning of the target, and is tilted 4 mm over its 2.4 m length. I did the same study on the 2017 data, as the target was moved between the two runs and the result is displayed in figure 39. The target is unfortunately shifted with respect to the x direction and hence less centred with respect to the beam.

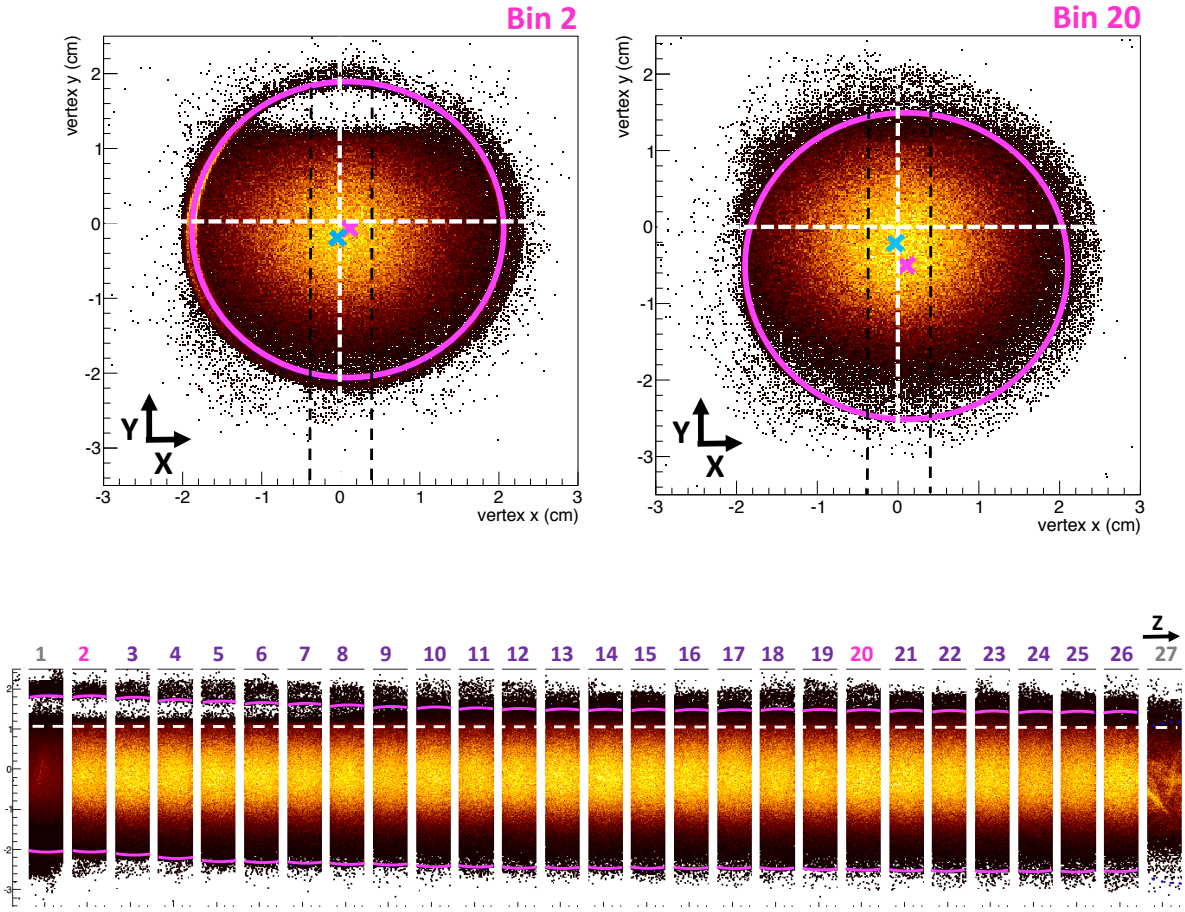

Figure 37: Distribution of vertices for bins 2 and 20 (top left and right). The target and beam centres are indicated by the pink and blue crosses respectively. The central parts of the transverse distributions defined by the two black dotted lines are presented for all the bins along the z-axis in the bottom figure to better visualise the intercept between the beam and the hydrogen target.

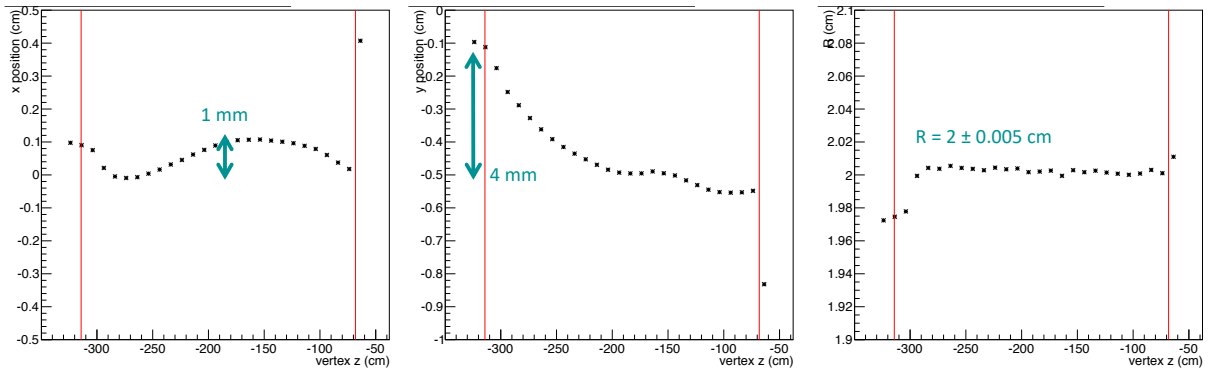

Figure 38: 2016 x and y positions of the target centre and it radius as a function of z.

This study allows to decide for a cut which will define the fiducial volume of hydrogen selected for the analysis. In the final analysis we will only consider the content of the target from bin 2 to 25, which corresponds to a cut in z: $-318.5 < z < -78.5$ cm. A constant $y = 1$ cut

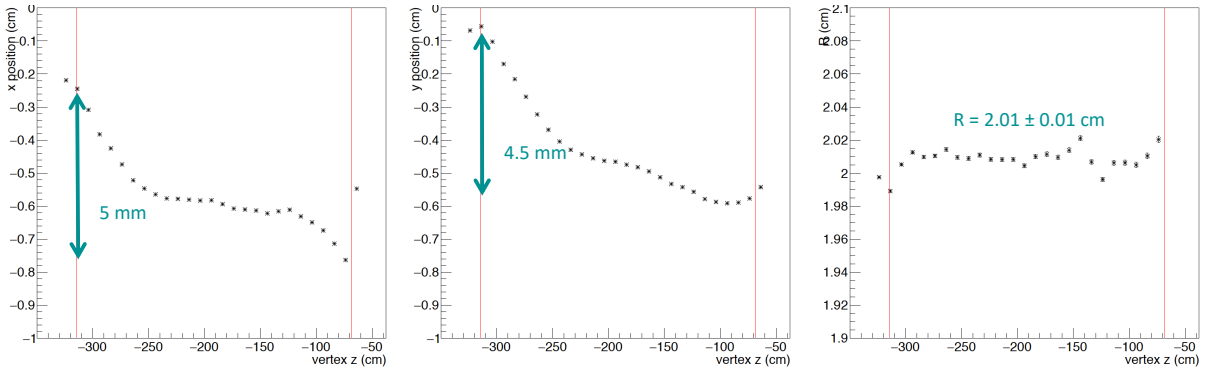

Figure 39: 2017 x and y positions of the target centre and it radius as a function of z.

is applied to get rid of the gaseous hydrogen, while we cut for each z slice all vertices outside a 1.9 cm radius away from the target centre. The cut is graphically displayed in figure 40.

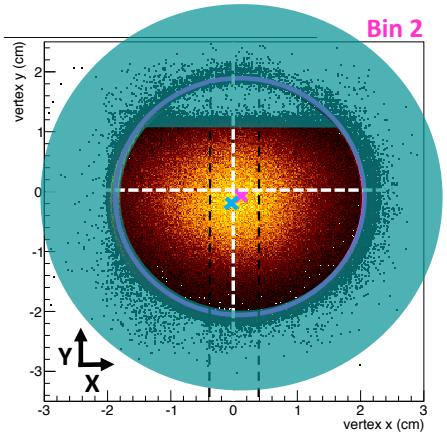

Figure 40: Distribution of vertices for bin 2 and the associated cut: all vertices inside the blue area and beyond are rejected from the analysis.

3.2 CAMERA CALIBRATIONS

Calibrations for the CAMERA detector are achieved in three different steps: the first one is about determining the azimuthal position φ of each individual slat, the second one is about finding the correspondence between timing difference and z-position of hits inside each individual slat, and the last one is about linking hit timing between inner and outer slats to recover a valid time-of-flight (see chapter 2).

To carry out these calibrations, I used three different and independent data sets: exclusive ρ^0 muo-production $\mu p \longrightarrow \mu p \rho^0$, elastic pion scattering on the proton $\pi^- p \longrightarrow \pi^- p$, and cosmic muon data without beam nor magnetic field. Elastic pion scattering is a two-body reaction on a fixed target for which the kinematics is completely determined knowing only the incoming and scattered pion momenta. Exclusive ρ^0 is a three-body reaction on a fixed target for which kinematics is completely determined knowing only the incoming and outgoing muon and

outgoing ρ^0 momenta. The ρ^0 is detected in the apparatus throughout its charged pions decay ($\rho^0 \to \pi^+\pi^-$). If we assume the BMS and spectrometer to be performing well, we can extract for both reactions an accurate value and direction of the recoiling proton momentum and compare it to the output of the CAMERA detector (see figure 41).

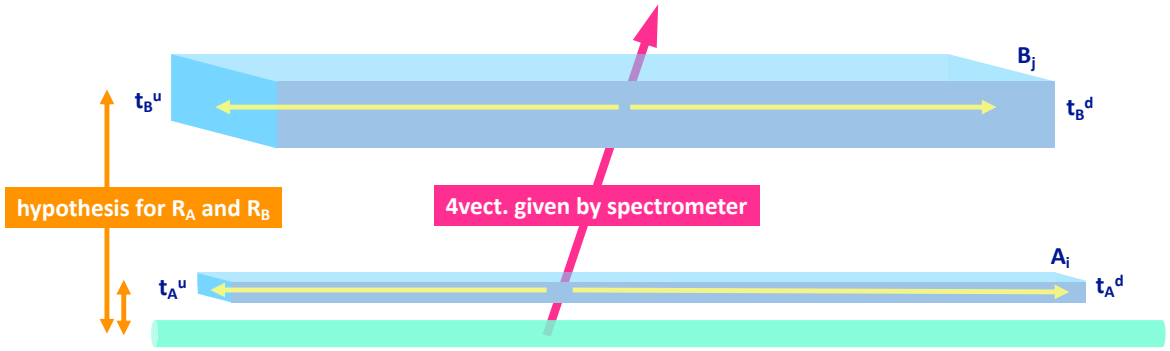

Figure 41: Principle used for the calibrations of CAMERA: The goal is to go from the recorded timings of a given set of slats to the momentum of the recoiling proton. This is achieved using simple physics reactions for which the proton momentum can be reconstructed with the sole use of the spectrometer information. This reconstructed momentum is compared with CAMERA measurement in order to extract calibration constants.

We note that the angular and momentum coverage of the recoil proton is similar for the two reactions mentioned above, as well as for the reaction of interest: $\mu p \longrightarrow \mu p \gamma$ (see fig.42).

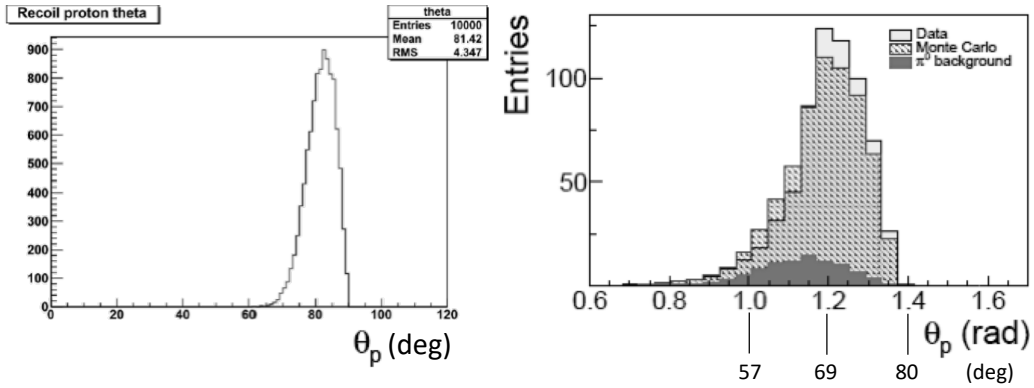

Figure 42: Proton polar angle distributions for elastic pion scattering (left) and exclusive single-photon production (right). Figures from [66] (left) and [42] (right).

Impact of CAMERA detector in the analysis

CAMERA detector is used for two complementary purposes in the experiment: it is used for detection and identification of a recoiling proton on one hand, and to ensure the best measurement possible for the proton momentum.

A priori t can be evaluated either using CAMERA alone, denoted t_{cam} or combining spectrometer, calorimeters and BMS information, denoted t_{spec}. We have, denoting $E_p = p'^0$ and $E_\gamma = q'^0$:

$$t_{cam} = (p - p')^2 = 2m(m - E_p) \tag{70}$$

$$t_{spec} = (q - q')^2 = -Q^2 - 2E_\gamma(\nu - q\cos\theta_{\gamma^*\gamma}). \tag{71}$$

As the resolution of the photon energy is always weak compared to the one of a charged particle momentum, E_γ has to be evaluated using information on q, ν and $\theta_{\gamma^*\gamma}$:

$$t'_{spec} = \frac{-Q^2 - 2\nu(\nu - q\cos\theta_{\gamma^*\gamma})}{1 + 1/m(\nu - q\cos\theta_{\gamma^*\gamma})}. \tag{72}$$

t_{cam} and t'_{spec} are two reasonably good approximations of t. These values can be improved using a kinematic fit as presented in figure 43 [42].

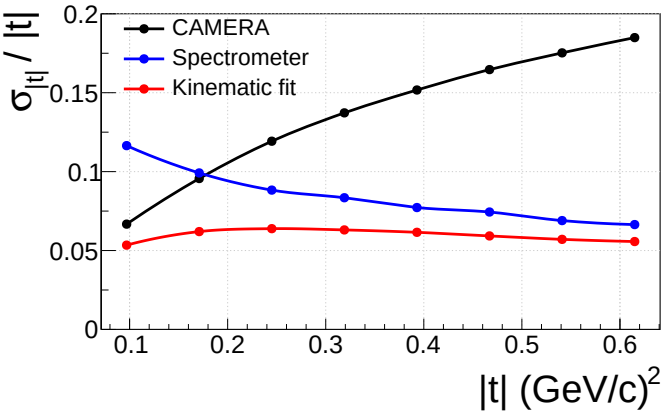

Figure 43: Relative resolution on t as a function of $|t|$. The black line corresponds to a determination of t by using the CAMERA detector only (t_{cam}). The blue line corresponds to a determination of t using the combined beam and spectrometer measurement of the in- and outgoing muon (t'_{spec}). The red line shows the most accurate determination of t by combining the beam and spectrometer measurement with the CAMERA measurement, using a kinematic fitting procedure. The resolutions have been extracted by comparing reconstructed and generated values of $|t|$, using a single photon Monte Carlo yield. Fig. from [42].

The region where CAMERA provides an insightful information related to the recoil proton momentum extends to $t < 0.2$ GeV^2, or $p < 460$ MeV or $\beta < 0.4$. This corresponds to half of the exclusive-single photon production statistics (see fig. 29, right).

φ calibration

To calibrate the azimuthal position of each slat, I use exclusive ρ^0 production. As I cannot use CAMERA to select exclusive channels since it was not calibrated yet, the exclusive ρ^0 sample selection relies on all cuts presented in section 4.3 but the 'exclusivity cut'. I apply instead a cut on the missing energy, and require the number of hits in each CAMERA scintillators to be less than four. This selection does not ensure that all considered hits in CAMERA are induced by the recoil proton of an exclusive event, but provides distributions clean enough to extract calibration constants.

For each slat, I plot the reconstructed value of the azimuthal angle of the proton momentum determined by the spectrometer and I average over all events. This gives a mean value of the scintillator φ_i position for the slat i:

$$\varphi_{A_i/B_i} = \langle \varphi^{spec} \rangle_{A_i/B_i} \tag{73}$$

According to the figure 31, we can write for each A slat:

$$\varphi_{A_i/B_i} = \varphi^0_{A_i/B_i} + (120 - \frac{360}{24} i) = \varphi^0_{A_i/B_i} + \varphi^i \tag{74}$$

Results are displayed in figure 44, where I present four distributions of the azimuthal angle of the reconstructed ρ^0 track minus φ^i, which are fitted by a Gaussian in order to extract $\varphi^0_{A_i/B_i}$. The table in figure 44 summarises all $\varphi^0_{A_i/B_i}$ values and the associated width. The noise in the distributions arises from the fact not all CAMERA hits considered are induced by the recoil proton of an exclusive event. The angular shifts and widths of B slats vary about 2%. The value of the widths for B slats have a mean value around $\langle \sigma_B \rangle = 5.7$ deg. This value is in between the σ of a Gaussian distribution with 15 deg FWHM ($\sigma_G = 15\,\text{deg}\,/2.36 = 6.36\,\text{deg}$) and the σ of a squared function of width 15 deg ($\sigma_S = 15\,\text{deg}\,/\sqrt{12} = 4.33\,\text{deg}$).
Ring A slat fluctuations are rather large, as variation of 10% of the angular width is observed. This translates into a fluctuation of the radial position of the slat of ± 2.5 cm for a cylinder having a 25.7 cm radius. These fluctuations are enabled by the mechanical forces constraining the long, thin and flexible slats assembled in the lightest way possible to detect low momentum protons (see figure 27).

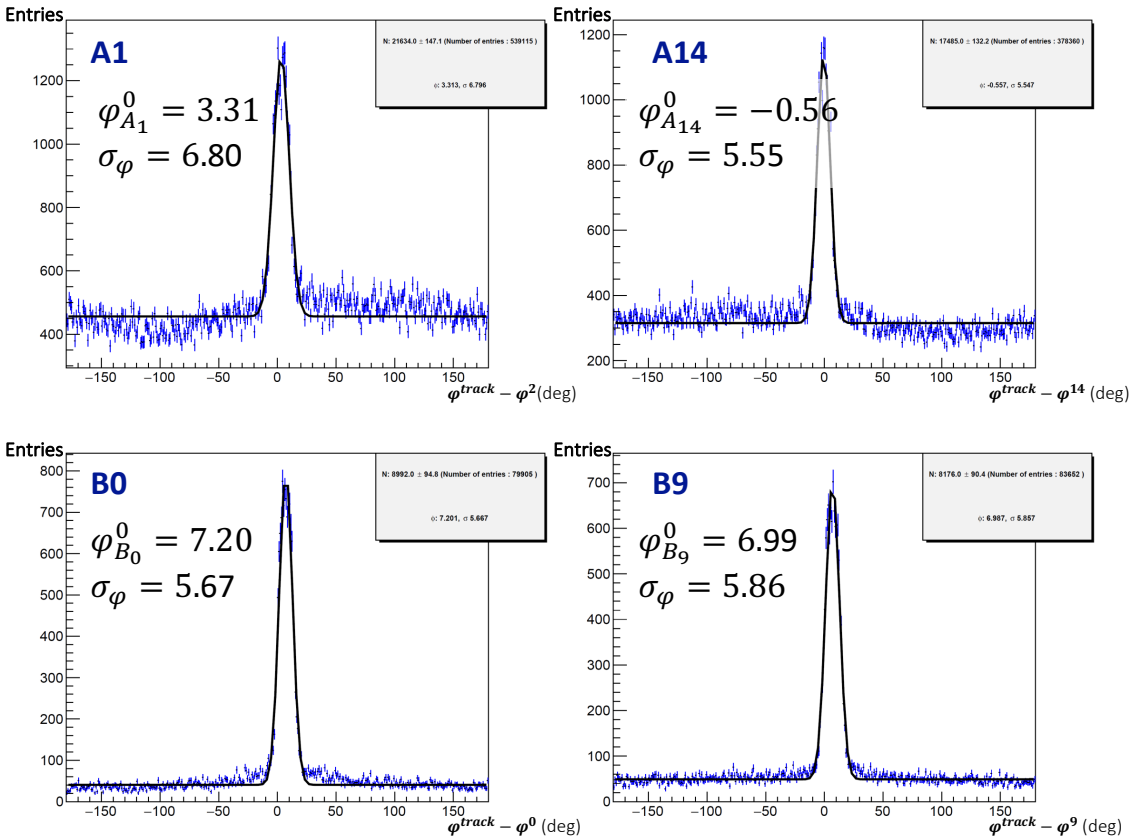

	0	1	2	3	4	5	6	7	8	9	10	11	12	13	14	15	16	17	18	19	20	21	22	23
φ^0_A	4.70	3.31	1.65	-0.15	-2.22	-3.72	-4.63	-5.14	-5.79	-5.68	-4.92	-4.24	-3.26	-1.92	-0.56	0.93	2.27	3.39	4.55	5.56	6.44	6.91	6.47	5.90
σ_φ	6.52	6.80	6.71	6.55	6.37	6.45	6.02	6.01	6.35	5.71	5.91	5.61	5.66	5.64	5.55	5.78	5.71	5.75	6.15	6.15	6.17	6.66	6.67	6.98
φ^0_B	7.20	7.36	7.49	7.38	7.32	7.31	7.24	7.12	7.23	6.99	6.90	6.93	6.79	6.60	6.65	6.66	6.62	6.67	6.63	6.69	6.78	7.02	6.99	7.17
σ_φ	5.67	5.69	5.64	5.69	5.78	5.58	5.71	5.70	5.76	5.86	5.54	5.83	5.63	5.57	5.63	5.78	5.73	5.75	5.76	5.76	5.78	5.66	5.78	5.73

Figure 44: Calibration of the azimuthal angle of CAMERA scintillators.
$\varphi^{track} - \varphi^i$, where $\varphi^i = 120 - \frac{360}{24}i$ is an approximation for the expected position of the scintillator i and φ^{track} is the azimuthal angle of the many reconstructed ρ^0 tracks. Ring A (top row) scintillators experience variations in the distribution width: A1 is the scintillator with the widest distribution and A14 the one with the tightest. Ring B (bottom row) does not display any such behaviour. All extracted values of the fit are displayed in the table: top two rows display $\varphi^0_{A_i}$ and σ for A scintillators, bottom rows display $\varphi^0_{B_i}$ and σ for B scintillators.

z calibration

The z-coordinates of a hit is calibrated using the proton track reconstructed in the spectrometer. As the z-position of a hit is given by the intersect of the proton track and the position of the scintillator, I have to make assumptions about the scintillator position and geometry. As an assumption, I consider scintillators to be straight, horizontal, arranged in a perfect circle centred on the z-axis of the spectrometer. I used as a radius for Ring A and Ring B the mean value obtained by the 2012 calibration: $R_A = 25.7 + 0.4$ cm (0.4 cm being Ring A scintillator thickness) and $R_B = 111.6$ cm. In that configuration:

$$z_A^{spec} = z_{vertex} + \frac{R_A}{\tan\theta} \tag{75}$$

$$z_B^{spec} = z_{vertex} + \frac{R_B}{\tan\theta}, \tag{76}$$

where θ is the polar angle of the proton track with respect to the z-axis. Considering the thickness and rigidity of Ring B scintillators, and given this part of the detector has been unchanged since 2012, this hypothesis is completely legitimate for Ring B. On the other hand, Ring A scintillators have all been changed between 2012 and 2016 in order to improve the detector efficiency. The analysis of the φ calibrations and a sight control on the detector itself can confirm easily that they suffer from distortion along z up to a few centimetres.

The first step of this calibration consists in plotting $\Delta t = t^u_{A_i/B_j} - t^d_{A_i/B_j}$ *vs* $z^{spec}_{A_i/B_j}$. One can check on figure 45 that both z_A^{spec} and z_B^{spec} display a linear behaviour as a function of Δt. This does not mean that scintillators are straight, which we know is untrue for some Ring A scintillators, it just means that this approximation is reasonable considering the resolution of the apparatus and the available statistics. This justifies to consider that:

$$z_{A_i} = \tfrac{1}{2} V_{A_i}(t^u_{A_i} - t^d_{A_i}) + C_{A_i}, \tag{77}$$

$$z_{B_j} = \tfrac{1}{2} V_{B_j}(t^u_{B_j} - t^d_{B_j}) + C_{B_j}. \tag{78}$$

One then needs to calibrate two quantities at once for each scintillator: the velocity of light inside the plastic V, and the offset that defines the centre of the scintillator C. Practically speaking, it means that I need to properly and automatically fit a straight line to the z *vs* Δt distributions. These two-dimensional distributions exhibit a non-zero thickness, which is a consequence of experimental resolution (see fig. 45 left column), and makes the distribution uneasy to work with. What I do instead is to slice-it up into Δt bins of 5 ns which I fit with a Gaussian distribution. I extract the mean values of these distributions and I am left with points on which I can fit a linear distribution. To maximise the efficiency of the fit I use a manually implemented dichotomy algorithm to find the velocity of light inside the scintillator, and I stop the procedure when the error of the slope of the linear fit is compatible with zero given the error on the fit. The intercept yields the value of the origin. I display in figure 45 (right column) the last iteration of the fit for some scintillators. I reach an overall less than three centimetre resolution on z_A and z_B with this method (where I consider the resolution to be the amplitude of the points dispersion with respect to the y-axis in figure 45 right column), which is to be compared to the approximately ten centimetre resolution on the z_{vertex}. This improved z-resolution is made possible by adding CAMERA to the spectrometer, as CAMERA detects tracks with wider polar

angles (> 60 deg) than the one detected in the forward spectrometer (< 10 deg). The noise in the distributions arises from the fact not all CAMERA hits considered are induced by the recoil proton of an exclusive event.

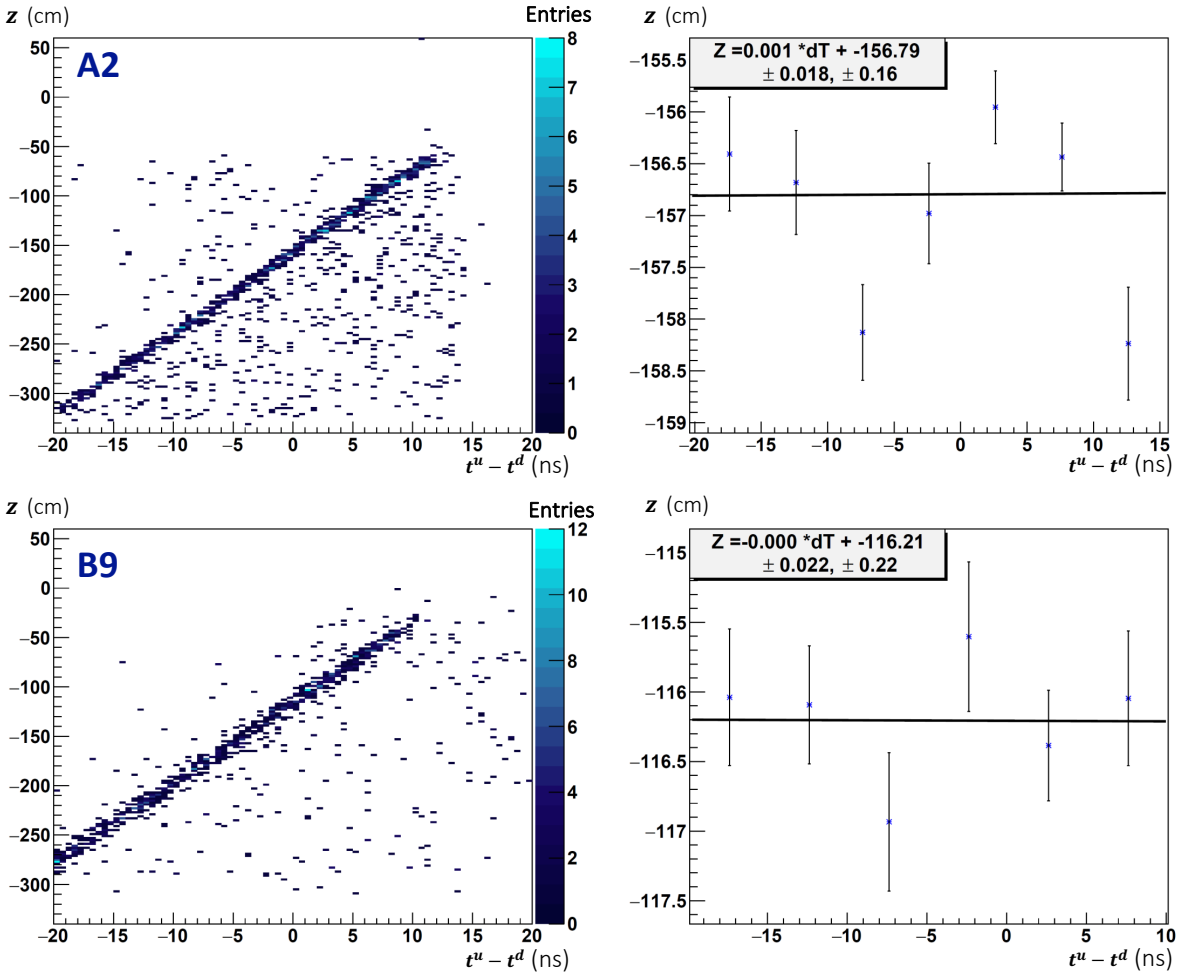

Figure 45: Calibration of the z position of CAMERA hits.
Left column: hypothesis for z of the hit for exclusive ρ^0 tracks as a function of $t^u - t^d$ for A2 (top) and B9 (bottom) scintillators. Distributions of events are straight and justify the linear relation used between z and t.
Right column: last iteration of the fit used to extract the two constants following the method described in the text for the two considered scintillators.

Momentum calibration

The determination of the momentum of a particle flying through CAMERA requires two different additional information to be reconstructed: the distance of flight (DoF) and the time of flight (ToF) of the particle.

According to our previous hypothesis on Ring A and Ring B and using the z calibration, the DoF writes:

$$\mathrm{DoF} = \sqrt{\left(z_{B_j} - z_{A_i}\right)^2 + \left(R_{B_j} - R_{A_i}\right)^2}. \tag{79}$$

On the other hand, the ToF is given by the time difference between the hit in Ring B and the one in Ring A. The time of a hit in a given scintillator is defined to be the average between the time given by the upstream and the downstream photo-multipliers. Nonetheless, each of these times has a constant but arbitrary origin due to light-guides, photo-multipliers and cables. This is modelled by adding a constant $C_{A_iB_j}$ in the ToF which depends on both A and B scintillators:

$$\mathrm{ToF} = \frac{t^u_{B_j} + t^d_{B_j}}{2} - \frac{t^u_{A_i} + t^d_{A_i}}{2} + C_{A_iB_j}. \tag{80}$$

This constant has therefore to be calibrated for each A_iB_j pair relevant to the analysis, i. e. sharing an angular sector of CAMERA. One can then reconstruct the four-momentum of the outgoing particle, assuming it is a proton of mass m, using:

$$\beta = \frac{\mathrm{DoF}}{\mathrm{ToF}}, \qquad p = \frac{m\beta}{\sqrt{1-\beta^2}}. \tag{81}$$

This process requires two steps: a first one which consists in evaluating $C_{A_iB_j}$ under certain hypothesis, and a second step which consists in confirming these hypotheses comparing CAMERA and the spectrometer reconstructed protons for some physics channels.

Calibration of $C_{A_iB_j}$ using cosmic muons

CAMERA has been built to overcome the low momentum resolution limit of the spectrometer regarding the outgoing proton detection, as $t \to 0$ is the kinematic region of interest for this measurement. Momentum calibration requires the selection of particles with known momentum. One could use the ρ^0 selection as for the z calibration, as it was done for 2012 data, but it has been decided instead to use cosmic muons for the first time in 2016 to free ourselves from the spectrometer momentum resolution.

Several runs of cosmic muons have been collected in 2016 and 2017 using CAMERA trigger, and the proton trigger to define a good track (coincident hits in A_i and B_i or A_i and B_{i+1}), without surrounding magnetic fields and no beam. The statistics of 2016 cosmic muons run was unfortunately not enough for me to perform the calibration of $C_{A_iB_j}$. I used the 2017 cosmic muons to do so, keeping in mind the CAMERA detector might have nonetheless experienced geometrical changes along the runs due to mechanical relaxations.

The principle of the calibration consists of inverting the relation stated above between $C_{A_iB_j}$ and β, assuming β is known. The first thing we should care about is that, contrary to *outgoing* protons, muons crossing CAMERA can go *any direction*. Though it is statistically very unlikely that a cosmic muon would go vertically upwards, nothing prevents horizontal muons to go any direction. The trick here lies into the fact that, for the detection of the recoil particles we are only interested in some of the $C_{A_iB_j}$, namely the one that corresponds to geometrically correlated sectors of CAMERA (A_i and B_i or A_i and B_{i+1}). Notably, A and B scintillators are geometrically

correlated by pair, as there is always two B scintillators (respectively two A scintillators) facing each other across the target. It happens that two ring B scintillators facing each other are separated by $2 \times R_B \simeq 2$ metres. As the speed of light is roughly 3 ns/metre, one expects muons to take more than 5 nano-seconds to go from one B scintillator to the other. We also expect $C_{B_jB_{j+12}}$ to be negligible against the ToF, as scintillators and light-guides have similar length and photo-multipliers similar characteristics. Hence we can sort out events such as:

$$\left| \mathrm{ToF}_B^\mu = \frac{t^u_{B_j} + t^d_{B_j}}{2} - \frac{t^u_{B_{j+12}} + t^d_{B_{j+12}}}{2} \right| > 5 \text{ ns} \quad \text{and} \quad \mathrm{ToF}_B^\mu > 0 \quad \text{or} \quad \mathrm{ToF}_B^\mu < 0. \tag{82}$$

If $\mathrm{ToF}_B^\mu < 0$ we can consider that the muon flies from B_j to B_{j+12}. If $\mathrm{ToF}_B^\mu > 0$ then it goes from B_{j+12} to B_j. From here, it is possible to determine unambiguously if the muon flies from Ring A to Ring B, as an outgoing proton would, which case I will denote $+$, or from Ring B to Ring A, which case I will denote $-$ (see figure 46). We have, with these notations:

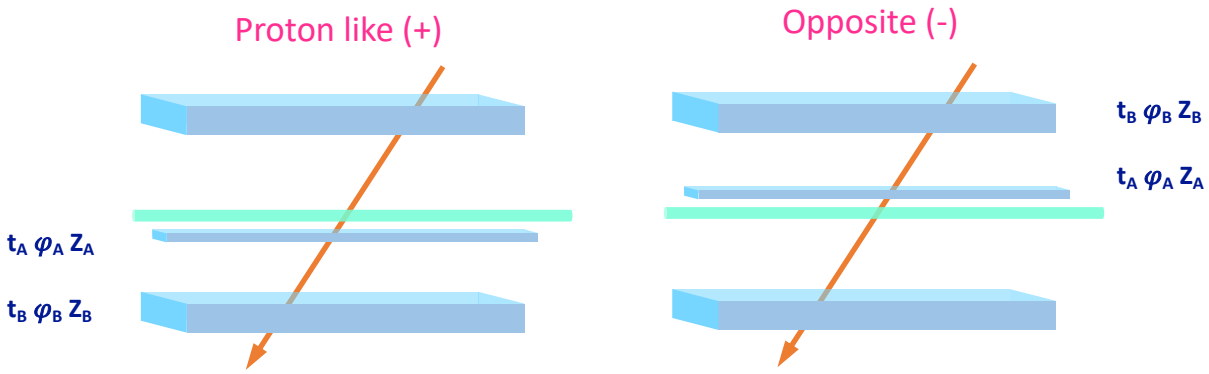

Figure 46: A cosmic muon can cross CAMERA A_iB_j pair of scintillators in two different ways: it can fly from A to B (left) or from B to A (right). In the first case, denoted +, everything happens as when a proton recoils, in the second one the relation between the calibration constant and the ToF is transformed according to equation 84.

$$C^+_{A_iB_j} = \frac{t^u_{A_i} + t^d_{A_i}}{2} - \frac{t^u_{B_j} + t^d_{B_j}}{2} + \mathrm{ToF}^\mu \tag{83}$$

$$C^-_{A_iB_j} = \frac{t^u_{A_i} + t^d_{A_i}}{2} - \frac{t^u_{B_j} + t^d_{B_j}}{2} - \mathrm{ToF}^\mu \tag{84}$$

where:

$$\mathrm{ToF}^\mu = \mathrm{DoF}^\mu / \beta^\mu, \tag{85}$$

$$\mathrm{DoF}^\mu = \sqrt{\left(z_{B_j} - z_{A_i}\right)^2 + \left(R_{B_j} - R_{A_i}\right)^2} = \sqrt{\left(z_{B_j} - z_{A_i}\right)^2 + \left(R_B - R_A + \delta R_{A_iB_j}\right)^2}. \tag{86}$$

$C^+_{A_iB_j}$ and $C^-_{A_iB_j}$ depend on the velocity of the muons. As muons have a few GeV of energy, which translates into $\beta^\mu \simeq 1$, one chooses $\beta^\mu = 0.999$, which corresponds to 4 GeV cosmic muons. $C^+_{A_iB_j}$ and $C^-_{A_iB_j}$ also depend strongly and directly on the difference of radii $R_{B_j} - R_{A_i}$,

but they do not depend explicitly on the individual radii. It is convenient to write $R_{B_j} - R_{A_i} = R_B - R_A + \delta R_{A_iB_j}$, where R_B and R_A are the mean values I chose as first hypothesis. I compute $C_{A_iB_j}$ for all relevant i, j and all values of $\delta R_{A_iB_j}$ between 9 and -3 cm. I display in figure 47 the result of this operation for two pairs of scintillators. $C^+_{A_iB_j}$ and $C^-_{A_iB_j}$ dependence on radii appears nonetheless indirectly through the z calibration described previously.

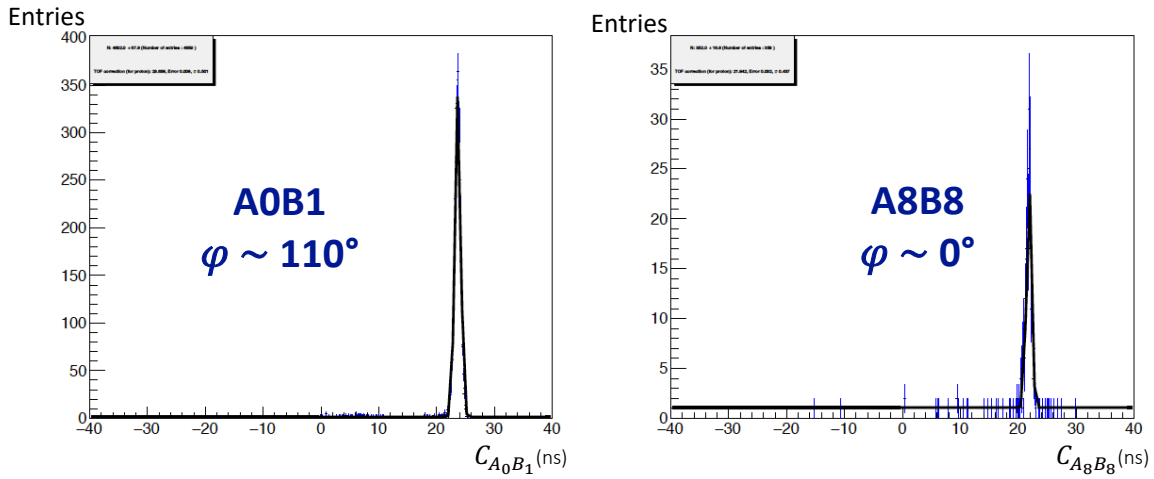

Figure 47: $C_{A_iB_j}$ for two different pairs of scintillators and for a given value of $_{A_iB_j}$. Even though the counts are reduced by a factor ten for pairs having horizontal inclination (right picture) compared to more vertically oriented pairs (left picture), the method consisting in the use of the three scintillators $A_iB_jB_{j+12}$ and the time cut $\left|\mathrm{ToF}^{\mu}_{B}\right| > 5$ ns proves to be highly effective as both $C^+_{A_iB_j}$ and $C^-_{A_iB_j}$ contributions to $C_{A_iB_j}$ combine in one peak, clearly visible and with almost no noise.

Determination of $\delta R_{A_iB_j}$ using elastic pion scattering

To determine $\delta R_{A_iB_j}$ I needed some high statistics data (as I have 48 relevant AB pairs) for comparing recoil protons reconstructed in the spectrometer and in CAMERA. To achieve that purpose, I used some elastic pion-proton scattering data taken with π^- beam in 2016, benefiting from an accurate reconstruction of the proton momentum as this is a simple two body reaction with a single charged track emitted in the forward spectrometer.

I chose as an evaluating observable the projection of the recoil proton four-momentum orthogonal to the z-axis of the spectrometer: p_T. p_T is an observable very sensitive to the calibration while being really close to t. I compare the proton momentum between CAMERA and the spectrometer using:

$$\Delta p_T = |p_T^{cam}| - |p_T^{spec}|. \tag{87}$$

I display in figure 48 Δp_T as a function of p_T^{spec} for a particular pair of scintillators, and several $\delta R_{A_iB_j}$. To determinate automatically the best value of $\delta R_{A_iB_j}$, I slice this distribution along p_T and I fit each slice with a Gaussian distribution. I extract the mean value and the sigma of the fits and plot it as a function of p_T. I chose to be the best $\delta R_{A_iB_j}$ the one that yields the least integral of absolute value of Δp_T in the domain $0.25 < p_T < 0.55$ GeV, as it is the region of greatest statistical significance (see fig. 48).

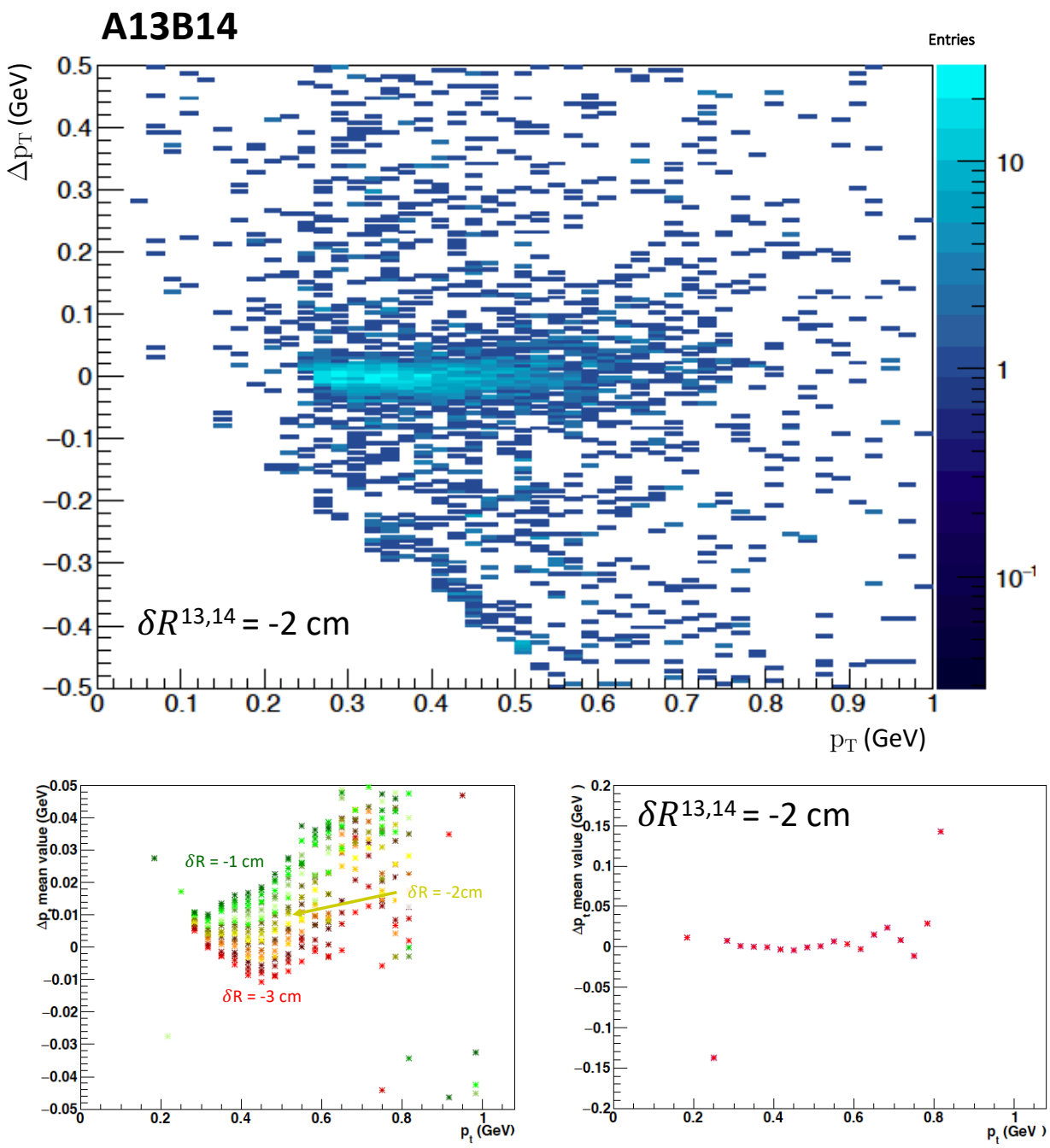

Figure 48: Δp_T as a function of p_T for the pair of scintillators A13B14 using elastic pion scattering data.
Top: distribution for $\delta R_{A_{13}B_{14}} = -2$ cm.
Bottom-right: mean-value of the fitted distribution on the top.
Bottom-left: mean-value of the fitted Δp_T for different values of $\delta R_{A_{13}B_{14}}$.
The value of -2 cm is the one selected automatically by the procedure described in the corresponding paragraph.

A_i	B_j	$\delta A_i B_j$	A_i	B_j	$\delta A_i B_j$	
0	1	8,5	1	1	8	
1	2	8	2	2	8,5	
2	3	8	3	3	8,5	
3	4	8,5	4	4	9	top part
4	5	9	5	5	8	of CAMERA
5	6	8	6	6	9	
6	7	8,5	7	7	8	
7	8	6,5	8	8	6	
8	9	2,5	9	9	2,5	
9	10	-3	10	10	1,5	
10	11	-3	11	11	-0,5	
11	12	-0,5	12	12	2,5	
12	13	-1	13	13	-2,5	
13	14	-2,5	14	14	-1,5	
14	15	-1	15	15	-1	bottom part
15	16	-2	16	16	-2,5	of CAMERA
16	17	2,5	17	17	0,5	
17	18	-1,5	18	18	-2,5	
18	19	-0,5	19	19	-2,5	
19	20	5	20	20	2,5	
20	21	6,5	21	21	6	
21	22	6	22	22	6	
22	23	7,5	23	23	8,5	
23	0	7,5	0	0	8	

Table 4: $\delta R_{A_i B_j}$ for all 48 pairs of scintillators.

I display the result in terms of $\delta R_{A_i B_j}$ in table 4. Unfortunately, we can notice that $\delta R_{A_i B_j}$ exhibits an unsteady behaviour as a function of $A_i B_j$. This is a problem as the calibration was meant to reflect some physics properties of the mechanical system, which should therefore display a continuous pattern. A tentative has been done to represent the evolution of the radial position of Ring A scintillators, considering all ring B scintillators having the same fixed nominal value R_B. This is presented in figure 49. One could imagine this picture testifies the mechanical deformations of Ring A under gravity, however the method aforementioned seems to work for the pair of scintillators belonging to the bottom part of CAMERA only, providing an obvious solution as for the value of $\delta R_{A_i B_j}$. It is unfortunately not the case for the top part of the detector nonetheless. As displayed in figure 50, one can see that pairs of scintillators placed in the bottom part of the detector tend to be easily calibrated (left column), offering an intermediate value of $\delta R_{A_i B_j}$ compatible with a mean-value centred at zero (top-left) and a width which does not vary with the value of $\delta R_{A_i B_j}$ (bottom-left); while pairs from the upper part of the detector (right column) would tend to have more than 9 cm of correction, flat distribution not even corresponding to $\Delta p_T = 0$ (top-right) and a resolution which changes with the value of $\delta R_{A_i B_j}$ (bottom-right).

After several unsuccessful attempts, as it was clear that the least was to reconcile both parts of the detector, I decided to apply an average, but constant value of $\delta R_{A_i B_j} = \delta R_{AB} = 4.7$ cm. For consistency, I decided to apply this δR_{AB} everywhere in the code. I had therefore to incorporate that quantity either to R_A or R_B. I chose to increase R_B, and I redid once the entire set of z and momentum calibration with $R_B = R_B + \delta R_{AB}$. Results are displayed in figures 84 and 52. The value of $\delta R_{AB} = 4.7$ cm provides a reasonable calibration at the scale of the entire

detector and resolution σ/p_T is comparable to the one obtained in 2012 (fig. 84). Δp_T bends slightly towards negative values ($|p_T^{cam}| < |p_T^{spec}|$) as p_T increases. This is not much of an issue as the determination of the proton momentum in this region should be taken to be the one provided by the spectrometer, and not by CAMERA according to their relative accuracy at high p_T. The reconstructed protons in CAMERA without and with $\delta R_{AB} = 4.7$ cm are displayed in figure 52. It appears clearly that the detector reconstructs two distinct populations when calibrated without δR_{AB}, while only one population is visible when $\delta R_{AB} = 4.7$ cm.

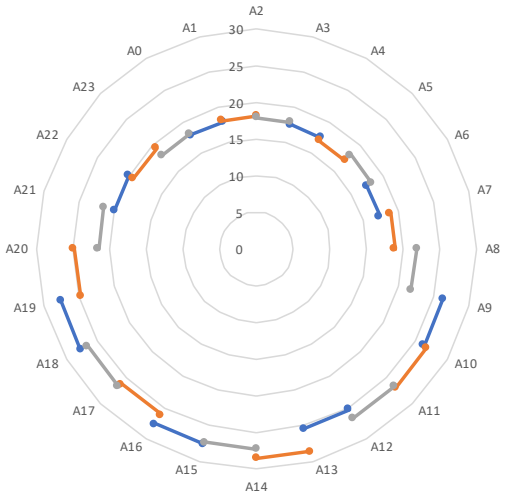

Figure 49: Radial position of Ring A scintillators averaged over the two corresponding B, considering all ring B scintillators having the same fixed nominal value and $\delta R_{A_iB_j}$ contributing only to R_A.

Interestingly, in 2012 a constant time-shift of 340 ps was added to the ToF in order to reach an accurate calibration of the detector. It happens that, for protons having a $\beta = 0.4$, this corresponds to an approximate 4.1 cm radius shift compatible with the value $\delta R_{AB} = 4.7$ cm.

I would like to conclude this chapter comparing the output of the two presented calibrations. The target calibration, on one hand, provides a clean reconstruction of the border of the target and each of its constituents can be clearly identified. It is relatively simple and takes advantage of the strengths of the forward spectrometer. The CAMERA calibration on the other hand appears to be quite complicated and unsatisfactory. Though it provides a reasonable momentum reconstruction for the recoil proton, it relies on geometrical approximations that are hard to refine. An additional tracker with a good position resolution that would have covered even a small part of CAMERA might have been helpful to determine exactly the position of this apparatus.

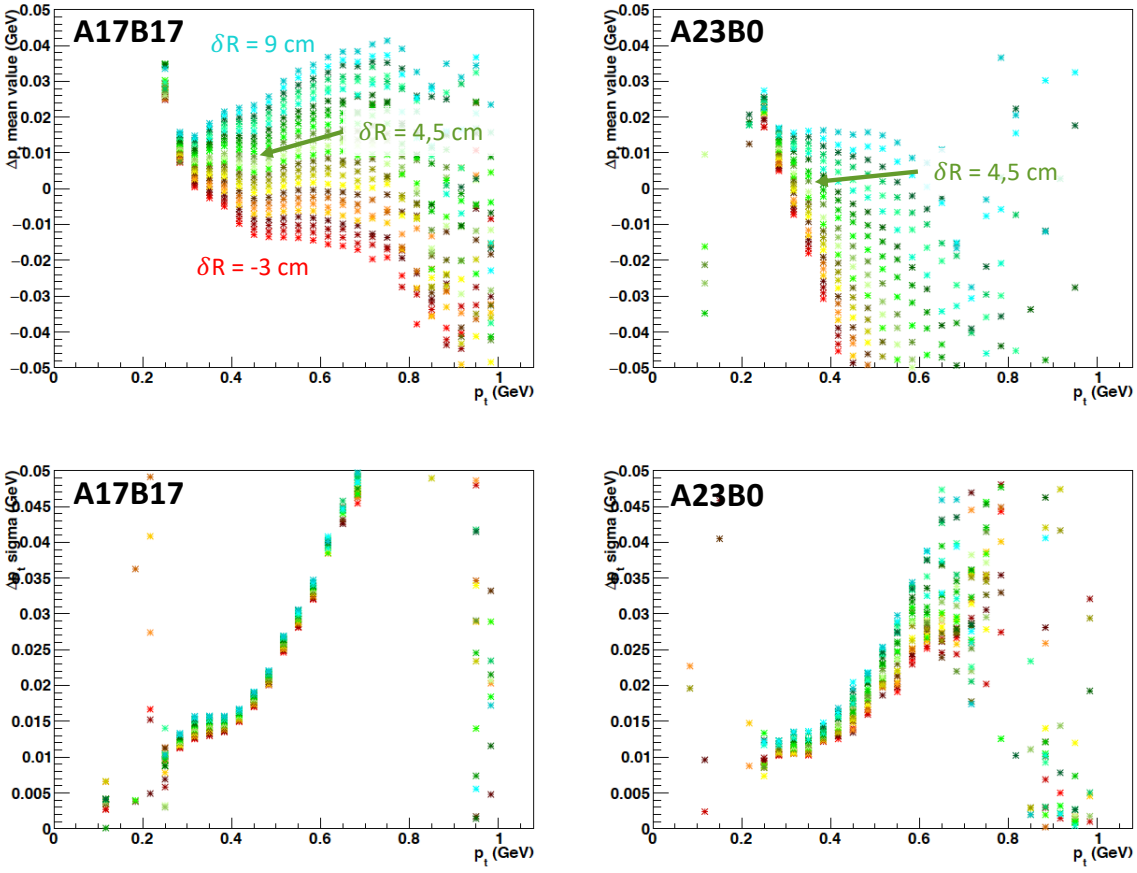

Figure 50: Fitted mean values of Δp_T as a function of p_T^{spec} (top row) and associated width (bottom row), for a pair of scintillator from the bottom part of CAMERA (left column) and the upper part of the detector (right column). The different colours correspond to different values of the parameter $\delta R_{A_iB_j}$. $\delta R_{A_iB_j} = 4.5$ cm is indicated for reference.

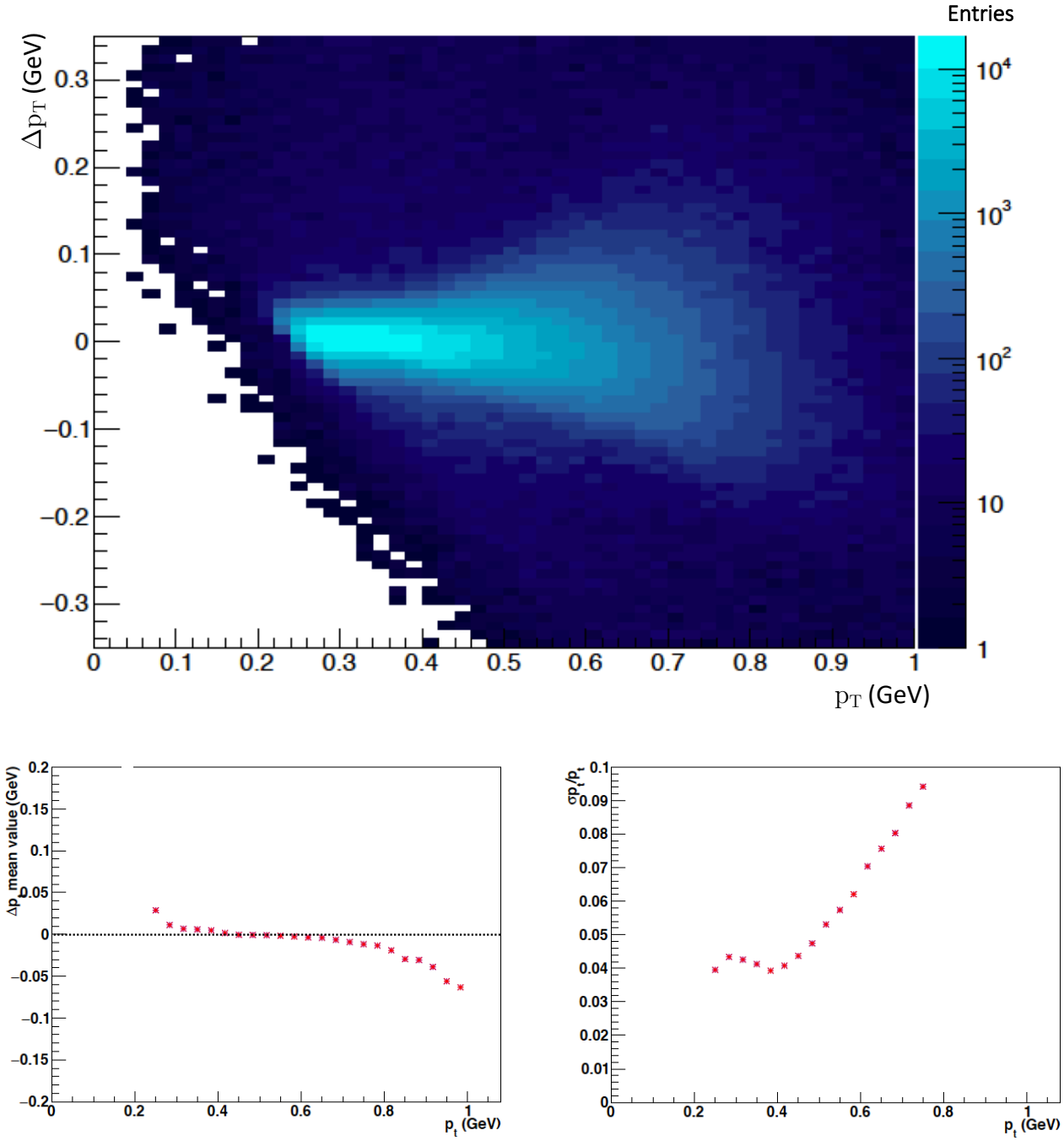

Figure 51: Top : Δp_T as a function of p_T for the entire CAMERA detector and for $\delta R_{AB} = 4.7$ cm, using elastic pion scattering data.
Bottom-left: mean-value of the fitted distribution on the top.
Bottom-right: σ/p_T of the fitted distribution on the top.
Note that, for recoil protons induced by pion elastic scattering, proton tracks have a polar angle close to 80 degrees (fig. 42, left) and $p_T \simeq p * 0.98$.

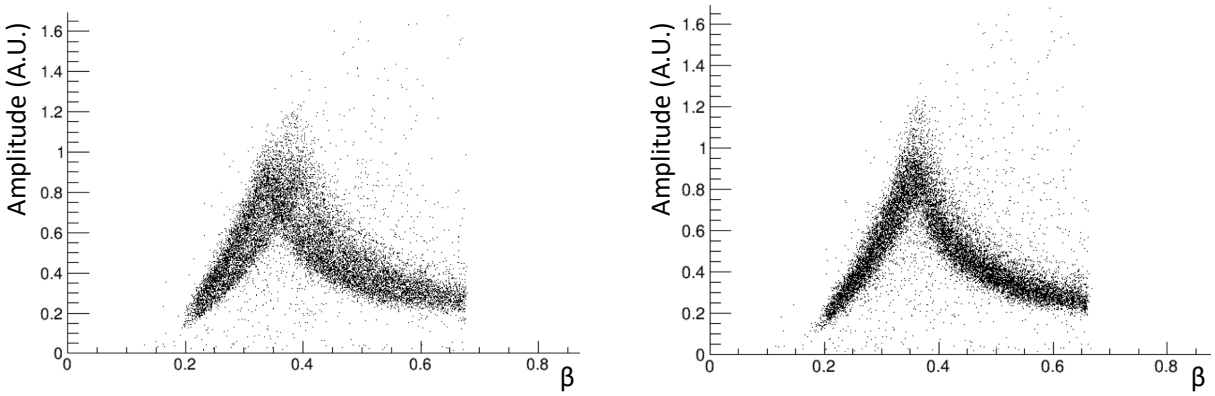

Figure 52: Energy loss in Ring B scintillators as a function of β of the recoiling particle, for exclusive ρ^0 data.
Left picture displays the proton signal out of CAMERA without $\delta R_{AB} = 4.7$ cm.
Right picture displays it including the $\delta R_{AB} = 4.7$ cm correction.

4

THE 2016 COMPASS DATA

The 2016 COMPASS Data has been collected in ten periods of approximately two weeks between April and October 2016. In between each period, changes in the experimental setup were permitted as detector experts could access the hall to maintain the spectrometer. This practically makes the periods the standard statistical units for analysing the data. A period is indeed the longest time scale during which it is reasonable to consider the data *a priori* compatible. At a final stage of the analysis, one has to justify a reasonable merging of the data from different periods in order to reach the total expected statistical significance of the measured cross section.

The ten 2016 periods (P01-P10) were taken with an approximately equal muon and anti-muon statistics and intensity. As μ^+ production is favoured in the scattering of the SPS proton beam on the berylium target, both the relative duration of the μ^+ and μ^- beam-time and the thickness of the berylium target have been adjusted accordingly. The decision to have an equal intensity for muon and anti-muon beams instead of having a greater total statistics, using the maximum reachable intensity with each muon charge, is a consequence of the 2012 test-run. In the 2012 data, taken with higher muon intensity, a discrepancy between muon and anti-muon normalised data was observed, pointing out an increasing inefficiency of tracking and/or CAMERA and/or calorimeters with increasing beam intensity. For this reason, and to allow the extraction of both lepton charge sum and difference cross sections, the decision was made to sacrifice statistics over charge and polarisation intensity ratio.

This chapter will display the systematic analysis of the ten periods of 2016 for three different physics channels. I will expose those channels by growing order of constraints:
- the first section will present the flux determination, which consists in selecting proper incoming muons;
- the second section will present the DIS selection, which consists in selecting an additional scattered lepton out of the target;
- the third section will present the exclusive ρ^0 production channel, which consists in selecting an additional outgoing ρ^0 and a recoiling proton;
- the fourth section will present the exclusive photon production channel, which consists in selecting an outgoing photon instead of a ρ^0;
- the last section will display a summary of these three channels along the 2016 year.

Adding particles in the final state includes more parts of the spectrometer in the analysis. This allows us to carefully investigate the quality of the production and the associated calibrations, as well as ensuring a proper processing of the data throughout the analyses. The flux determination requires only the use of the beam telescope and the target position. The DIS analysis includes in the analysis the full set of trackers in the forward spectrometer as well as the trigger system. The exclusive ρ^0 channel requires the detection of two extra charged tracks

$(\pi^+\pi^-)$ in the spectrometer and the additional use of CAMERA for exclusivity check, and the DVCS channel requires the addition of the electromagnetic calorimeters on top of that.

As the production of the 2016 data is still ongoing, the results displayed in this chapter are nothing but a status of the analysis. In particular a huge effort has been made by the collaboration in order to improve the calibrations of electromagnetic calorimeters in the past few weeks. These new calibrations have not been propagated to all periods of data yet. To do justice to the hard work involved, I decide to present in the following the details of P08 slot4, as this production reflects the very latest state of the production as it was issued the twenty-ninth of May. I will nonetheless present the summary of the analysis for the full year as it was released to the collaboration mid April, with previous productions not including these latest calorimeters calibrations.

Throughout the chapter, I will use the following conventions. We denote k, k', q, q', p, p' the four-momenta of an incident muon, an outgoing muon, a virtual photon, a ρ^0 (or real photon), a target proton, and a recoil proton respectively. For any process involving both an incoming and a scattered lepton ν denotes the energy of the resulting virtual photon in the laboratory frame ($\nu = k^0 - k'^0$), $y = \nu/k^0$ denotes its relative energy, and Q^2 its virtuality. As in chapter 1, for exclusive processes I denote $t = (q - q')^2 = (p - p')^2$ the squarred four-momentum transfer to the proton target, E_ρ (or E_γ) and E_p the energies in the laboratory frame of the meson ρ^0 (or real photon), and the recoil proton respectively.

4.1 FLUX DETERMINATION

It is straightforward that a flux determination is needed when one wants to extract a cross section. The flux determination relies on the existence of a random trigger described in chapter 2 and the accurate determination of the target fiducial volume presented in chapter 3.

The flux determination is performed spill by spill using the beam tracks reconstructed from random trigger events during the spill. It is determined separately for muons and anti-muons and writes as follow:

$$\text{Muon Flux} = \int_{\text{time in spill}} \mathrm{dt}\, \frac{\text{number of reconstructed beam tracks}}{\text{number of random triggers accepted in DAQ} \times \Delta\mathrm{t}} \tag{88}$$

and the beam flux corrected for DAQ dead time is:

$$\text{Muon Flux in DAQ} = \int_{\text{time in spill}} \mathrm{dt}\, \frac{\text{number of reconstructed beam tracks}}{\text{number of random trigger attempts} \times \Delta\mathrm{t}}. \tag{89}$$

Δt is the time interval around the random trigger time (see Fig. 53). In principle, flux should be independent of Δt, but happens to be impacted by the individual time windows set for each detector. Δt should therefore be away from the edges of all detector timing windows. Practically flux values vary smoothly with Δt, and is constant for an intermediate interval around ± 2 ns. The time in spill is considered from 1.5 s to 5.0 s after the beginning of the spill (see Fig. 54).

The reconstructed beam tracks considered for flux determination respect the following conditions:

- time in spill t between 1.5 s and 5 s and within Δt

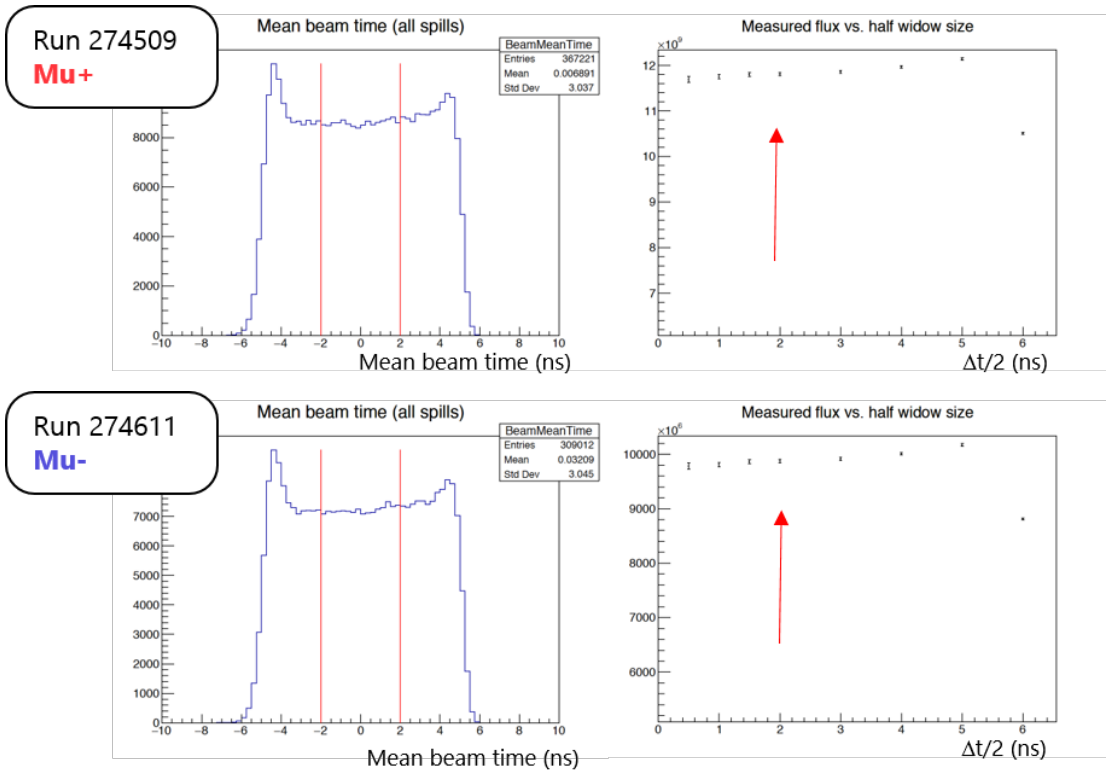

Figure 53: Time distribution of beam tracks for 2 runs of P07 (right figures). The time domain is limited by a software analysis window of [-5, +5 ns] around the random trigger time. The time interval Δt for the flux determination is chosen from -2 to +2 ns where a flat plateau is expected and observed (see left figures).

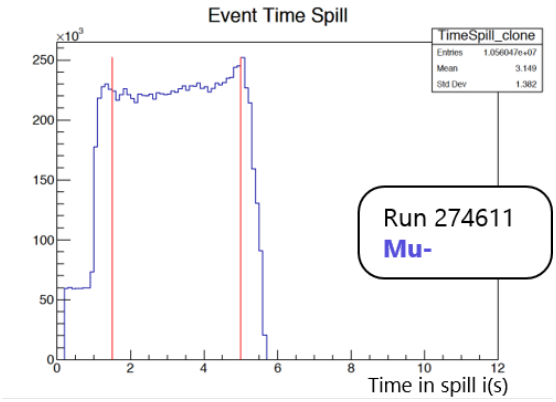

Figure 54: Distribution of events in the spill. The time in spill is considered from 1.5 s to 5.0 s after the beginning of the spill.

- 2 hits in SciFi and 3 hits in SI
- momentum between 140 GeV and 180 GeV
- momentum error $<$ 2.5% of the momentum value
- beam track must traverse target at a distance $<$ 1.9 cm from the target axis and remain below $y = 1$ cm across the full length from z = -318.5 cm to z = -78.5 cm (see Fig. 55)

The timing cuts (first item on the list) are used to ensure the flux stability. They correspond to the selection of random triggers only when there is beam (time in spill cut), and increase the probability that the incoming reconstructed track corresponds to the track that has fired the triggers. The second item allows a precise track reconstruction for the incident muon provided by fast trackers located upstream of the target. The third and fourth items allow for a reasonable momentum determination using the Beam Momentum Station (see figure 21). The target cuts (last item) are used to define accurately the density of the target (as it selects liquid hydrogen only), and it total effective length, in order to evaluate exactly the luminosity. It is very important that the exact same cuts are applied to the data selection as well in order to allow for its normalisation.

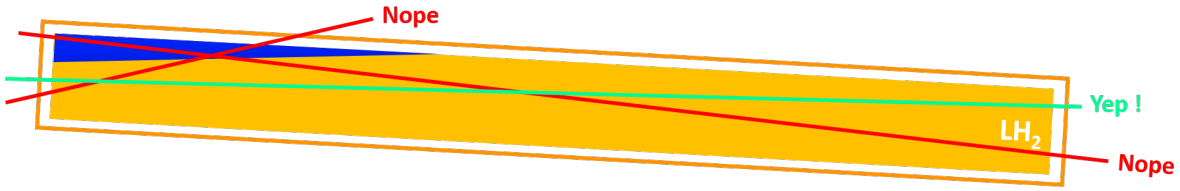

Figure 55: Criteria to select a reconstructed beam track crossing the target.

4.2 THE DIS DATA-SET

The DIS data selection is used as a pre-selection for exclusive events. It is a useful tool to control simultaneously the flux values obtained with the method described in the previous paragraph and their proper use, as well as the spectrometer and triggers performances. Muon and anti-muon DIS events ratio should be equal to one when normalised to their respective flux. In particular, a very thorough geometric analysis of the physics trigger was achieved to clean-up reconstructed scattered muons and improve this ratio. In a further step we should be able to retrieve the known DIS cross section. Additionally, I use this DIS analysis to ensure the complete processing of the data throughout my analysis. Such procedure is important given that the data is split in a very large amount of small data files. The DIS analysis is done twice as a sub-part of the two independent analysis that are ρ^0 HEMP and DVCS. For a given period, the number of DIS events obtained for both procedures should be strictly equal if the same amount of data has been processed.

In all following graphs, I plot in red the μ^+ distributions and in blue the μ^- distributions. The μ^- distributions are normalised to the μ^+/μ^- flux ratio. The figures on the top-right corner of plots correspond to the counts for each charge (before normalisation).

DIS event selection

The cut used to select DIS events are as follows:

- incoming muon selection
  - beam track with the same requirements as for flux determination;

- vertex selection
  - 'best primary vertex': only one vertex is considered for the selected events, and it is the one having the best time and space χ^2 with respect to the reconstruction procedure;
  - vertex in the target: the longitudinal position of the vertices must satisfy the condition -318.5 cm $< z_{vertex} <$ -78.5 cm and the radial distance from the target centre at z_{vertex} must be $r_{vertex}(\text{vertex}, \text{TargetCenter}(z_{vertex})) < 1.9$ cm and $y_{vertex} < 1$ cm (see figure 56);
- outgoing muon selection
  - at least one outgoing muon is detected;
  - muon has triggered the Middle, Ladder or Outer Trigger (MT, LT, OT respectively);
  - outgoing muon must travel more than 15 radiation lengths;
  - the first measured point of the outgoing muon must be upstream of SM1 ($z_{first} <$ 350 cm);
  - the last measured point of the outgoing muon must be downstream of SM1 ($z_{last} >$ 350 cm);
- DIS kinematic cuts
  - $0.05 < y < 0.95$;
  - $1\ (\text{GeV/c})^2 < Q^2 < 10\ (\text{GeV/c})^2$.

All those cuts are applied to control the muonic part of the exclusive processes. If they select DIS events, they are nonetheless chosen to match the kinematic range expected for the exclusive analysis and are not optimised towards the extraction of DIS related quantities.

The incoming muon cut is applied as the flux one for consistency. The r_{vertex} and z_{vertex} cuts are there to ensure the lepton has scattered inside the target. Note that the r_{vertex} cut is a straightforward consequence of the target cut for beam track (see figure 56). The 'best primary vertex' cut is there to avoid double counting of DIS events. Indeed, for one incoming plus (at least) one outgoing muon detected, several primary vertices candidate might be reconstructed by the software, leading to different values of ν and Q^2 associated to the events. We conventionally select the best-fit one. The trigger cut on the outgoing muon is a hardware cut as the event are not recorded if they do not generate triggers. At the present state of the analysis, we consider three main triggers: the middle, the ladder and the outer. We consequently display results for MT, LT, and OT in the following. The three next cuts are applied in order to ensure the proper reconstruction of the outgoing muon momentum. The y cut is used to remove events that would need large radiative corrections at high y and poorly reconstructed kinematics due to bad resolution at small y (or small ν). The lower limit in Q^2 is applied as DVCS requires a high energy scale for collinear factorisation to hold.

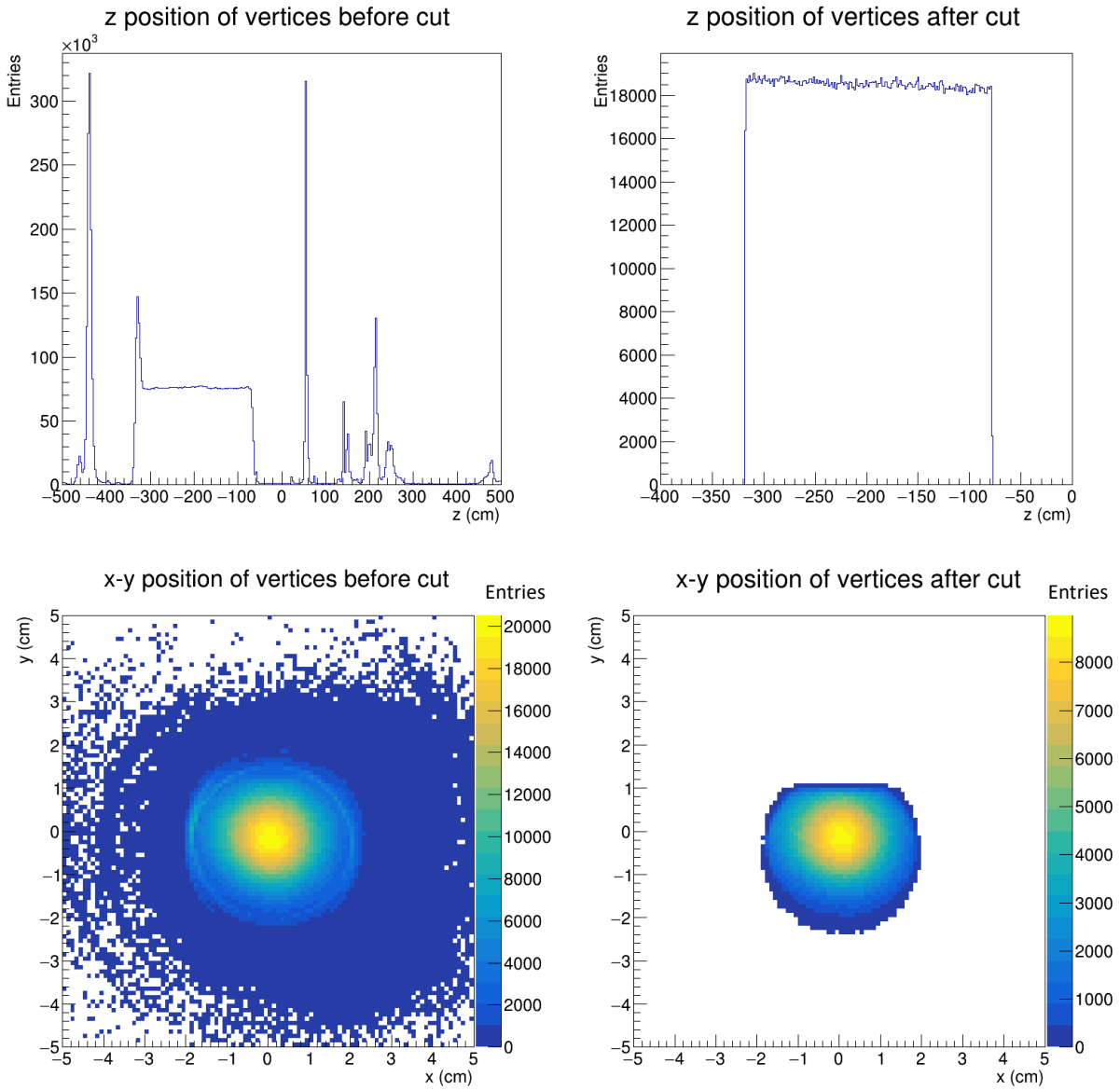

Figure 56: Top row: z-distributions of vertices before (left) and after (right) cuts on the vertex position. Bottom row: (x, y)-distributions of vertices before (left) and after (right) cuts on the vertex position (P08 slot4).

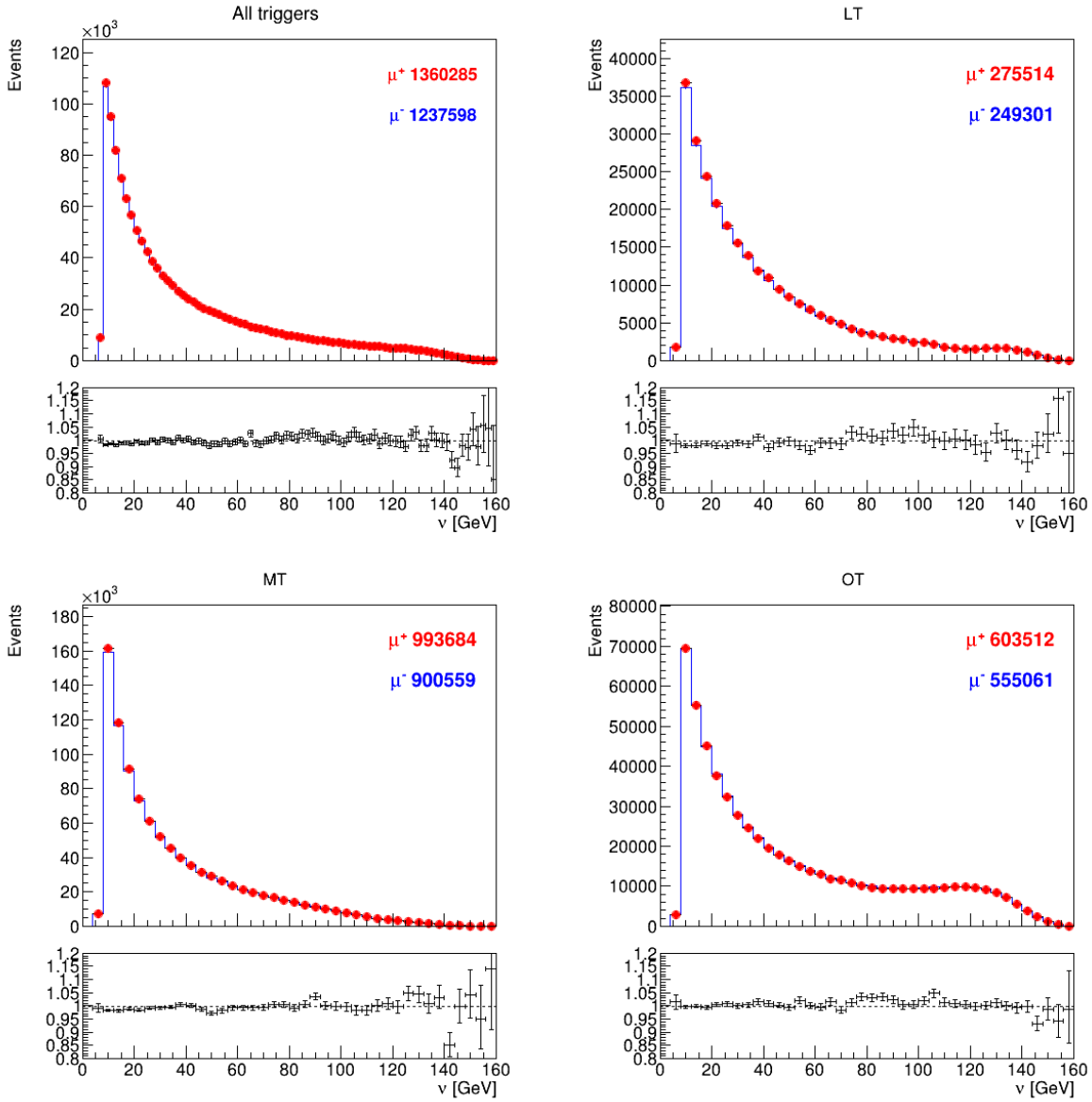

Figure 57: Virtual photon energy (ν) distributions of DIS events per trigger for μ^+ (red) and μ^- (blue) beams. The μ^- distributions are normalised to the μ^+/μ^- flux ratio. The ratio between μ^+ and μ^+ distributions is displayed below the graphs (P08 slot4).

Results

The distributions of DIS events for one period and for each trigger is presented in figure 57. The μ^- distributions are normalised to the μ^+ beam flux. The agreement between μ^+ and μ^- distributions is rather good except at small ν (< 20 GeV) where there is a 1 or 2% discrepancy.

4.3 THE EXCLUSIVE ρ^0 DATA-SET

The selection of $\mu p \to \mu p \rho^0$ events requires to detect three extra particles in the final states: the recoil proton using CAMERA, and the two charged pions resulting from the ρ^0 meson decay that can be detected in the spectrometer. COMPASS data displays a very neat ρ^0 signal that makes this channel particularly useful and unambiguous. Detector-wise, this channel allows to control that the addition of the CAMERA detector does not bias the analysis regarding the ratio of muon over anti-muon signal. The recoil proton induced by exclusive ρ^0 production is kinematically very close to the one in DVCS, hence this signal is relevant for calibration use while not relying on the *delicate* use of calorimeters. The cuts used for muons and vertex selection are the same as displayed in the above paragraph.

Proton selection and exclusivity cuts

A good proton candidate is reconstructed in CAMERA if it displays two geometrically correlated hits (one in Ring A and one in Ring B) with a reconstructed β between 0.1 and 1. For a given proton candidate, the kinematics of the reaction is over-determined and we can compare observables reconstructed using only the spectrometer to the one reconstructed in CAMERA.

All good proton candidates (see Fig. 58) are then combined with the four other charged tracks selected beforehand for μ, μ' and ρ^0, to create a list of exclusive events candidate. At this stage, the list of candidates still contains a significant fraction of non-exclusive background events, which are removed by applying suitable exclusivity cuts.

The distribution of energy deposit of good proton candidates in Ring B of CAMERA (see fig. 58 left) displays a cusp which separates two domains: $\beta < 0.4$, where protons stop inside Ring B scintillators and deposit all their energy in it, and $\beta > 0.4$, where protons are energetic enough to escape Ring B scintillator and deposit less and less energy as they cross faster the scintillator. The distribution of energy deposit of good proton candidates in Ring A of CAMERA (see fig. 58 right) only displays the decreasing part of the Ring B distribution, as all protons escape the scintillators (which is intended to allow for ToF measurement of the track).

The exclusive reaction $\mu p \to \mu p \rho^0$ or $\mu p \to \mu p \gamma$ can be studied using the spectrometer alone, and applying a cut either on missing mass or energy, assuming the missing particle to be a proton:

$$M^2_{miss} = M^2_{X=p'} = (k + p - k' - q')^2 = 2m_p(\nu - E_{\rho^0}) + {m_p}^2 + t \tag{90}$$

$$E_{miss} = (M^2_{miss} - {m_p}^2)/2m_p = \nu - E_{\rho^0} + \frac{t}{2m_p} \tag{91}$$

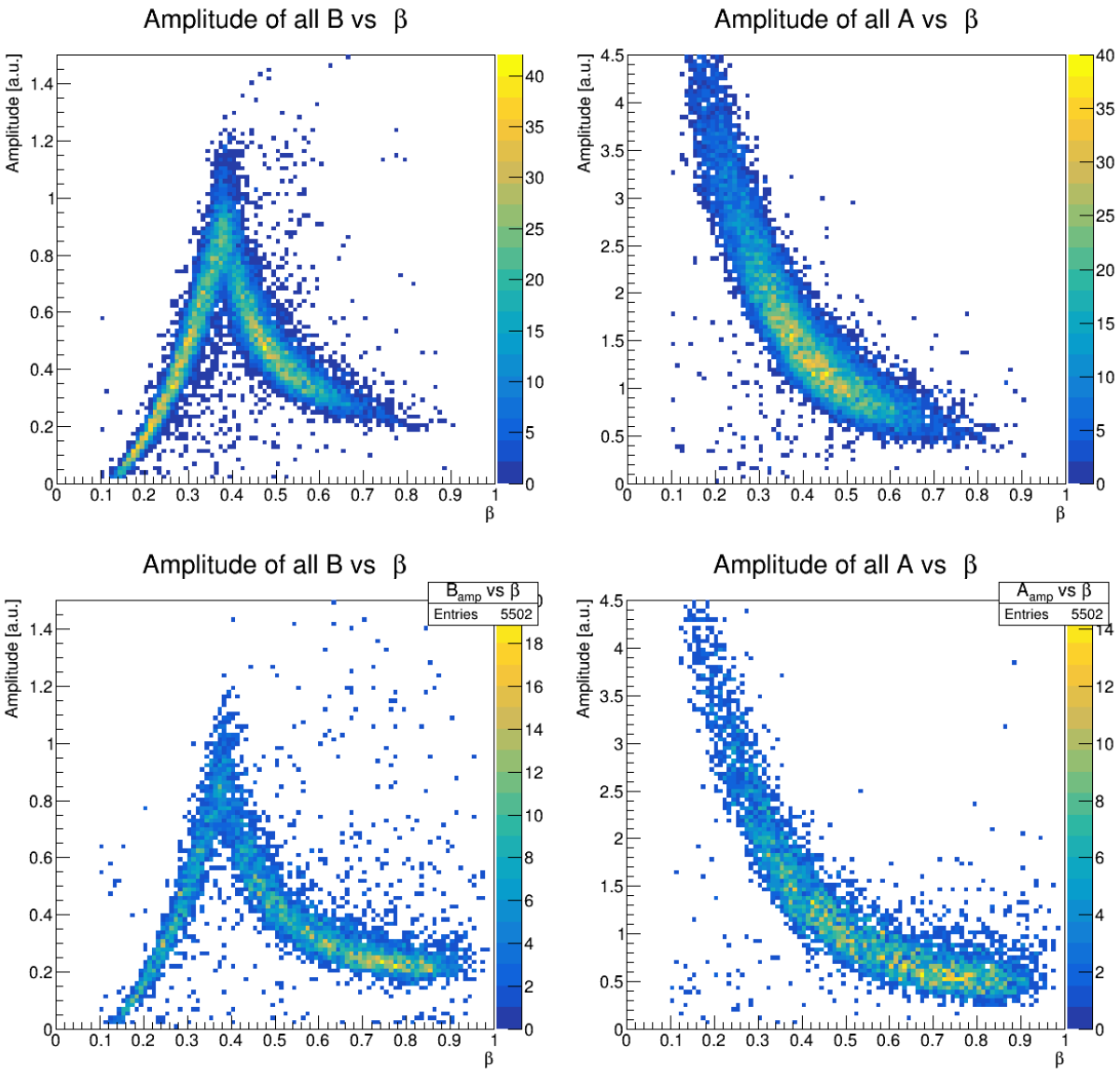

Figure 58: Energy loss in B and A scintillators of CAMERA vs proton velocity (β) for proton selection in exclusive ρ^0 (top figures) and γ (bottom figures) productions (P08 slot4).

The evaluation of such quantities is always done using the four-momenta (left hand of the expression). The right hand of the expression is here to show how they relate to the kinematic variables of interest.

This idea can be extended when detecting the complete final state using the proton detected in CAMERA, with a cut on the missing mass of a particle which should be nothing or background:

$$M^2_{undet} = M^2_{X=0} = (k + p - k' - q' - p')^2 = 2(\mathrm{m_p} - E_p)(\nu - E_{\rho^0} - E_p) + t \tag{92}$$

We construct three other so called 'exclusivity variables', which always measure the difference between an observable reconstructed in CAMERA and the same observable reconstructed in

the forward spectrometer. We consider this difference for azimuthal angles, for transverse momenta of the proton, as well as the difference between the z position of the hits in the inner CAMERA ring given either by the Ring A scintillator or by the interpolation between the vertex and the outer ring:

$$\Delta\varphi = \varphi^{cam} - \varphi^{spec} \tag{93}$$

$$\Delta p_T = |p_T^{cam}| - |p_T^{spec}|, \tag{94}$$

$$\Delta z = z_A^{cam} - z_A^{z_B \text{ and vertex}}. \tag{95}$$

In practice, Δp_T can be evaluated either relatively to the virtual photon direction, the direction of the incident muon or the laboratory z-axis. The last solution yields better resolution as it is the variable which has been optimised by the calibration procedure of CAMERA. It is the one used in the plots presented below.

Exclusive ρ^0 event selection

Cuts are applied tight for this analysis as the selection of ρ is done either to study CAMERA or to calibrate it. This event selection is not used for absolute cross section determination and we favour a clean signal over an optimised statistics.

The cuts used to select $\mu p \to \mu p \rho^0$ events are as follow:

- incoming muon selection
  - beam track with the same requirements as for flux determination;
- vertex selection
  - 'best primary vertex': only one vertex is considered for the selected events, and it is the one having the best time and space χ^2 with respect to the reconstruction procedure;
  - vertex in the target: the longitudinal position of the vertices must satisfy the condition -318.5 cm $<$ z_{vertex} $<$ -78.5 cm and the radial distance from the target centre at z_{vertex} must be $r_{vertex}(\text{vertex}, \text{TargetCenter}(z_{vertex})) < 1.9$ cm and $y_{vertex} < 1$ cm;
- outgoing muon selection
  - at least one outgoing muon is detected;
  - muon has triggered the Middle, Ladder or Outer Trigger (MT, LT, OT respectively);
  - outgoing muon must travel more than 15 radiation lengths;
  - the first measured point of the outgoing muon must be upstream of SM1 ($z_{first} < 350$ cm);
  - the last measured point of the outgoing muon must be downstream of SM1 ($z_{last} > 350$ cm);
- DIS cuts
  - $0.05 < y < 0.95$;
  - 1 GeV^2 $< Q^2 <$ 10 GeV^2;

- ρ^0 cuts
  - two additional charged tracks with opposite sign;
  - with a reconstructed invariant mass: 0.5 GeV $< M_{\pi\pi} <$ 1.1 GeV;
- proton cuts
  - a hit in Ring A and a hit in Ring B of CAMERA that belong to azimuthal sectors that are geometrically correlated;
  - the candidate proton has $0.1 < \beta < 1$;
  - z_A and z_B inside the domain of the scintillators A and B;
- exclusivity cuts
  - $|\Delta\varphi| < 0.15$ rad;
  - $|\Delta p_T| < 0.08$ GeV;
  - $|\Delta z|$ <16 cm;
  - $|M^2_{undet}| < 0.15$ GeV^2;

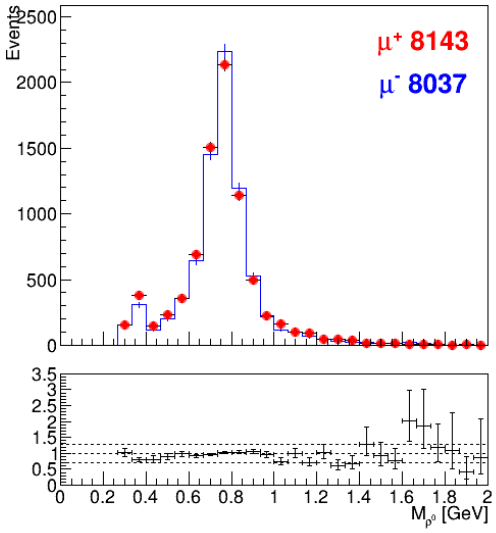

Figure 59: $\pi^+\pi^-$ invariant mass with all other cuts applied but the 'exclusive event' one for μ^+ (red) and μ^- (blue) beams. A peak is clearly visible around the ρ^0 mass ($M_{\rho^0} = 775$ GeV) (P08 slot4).

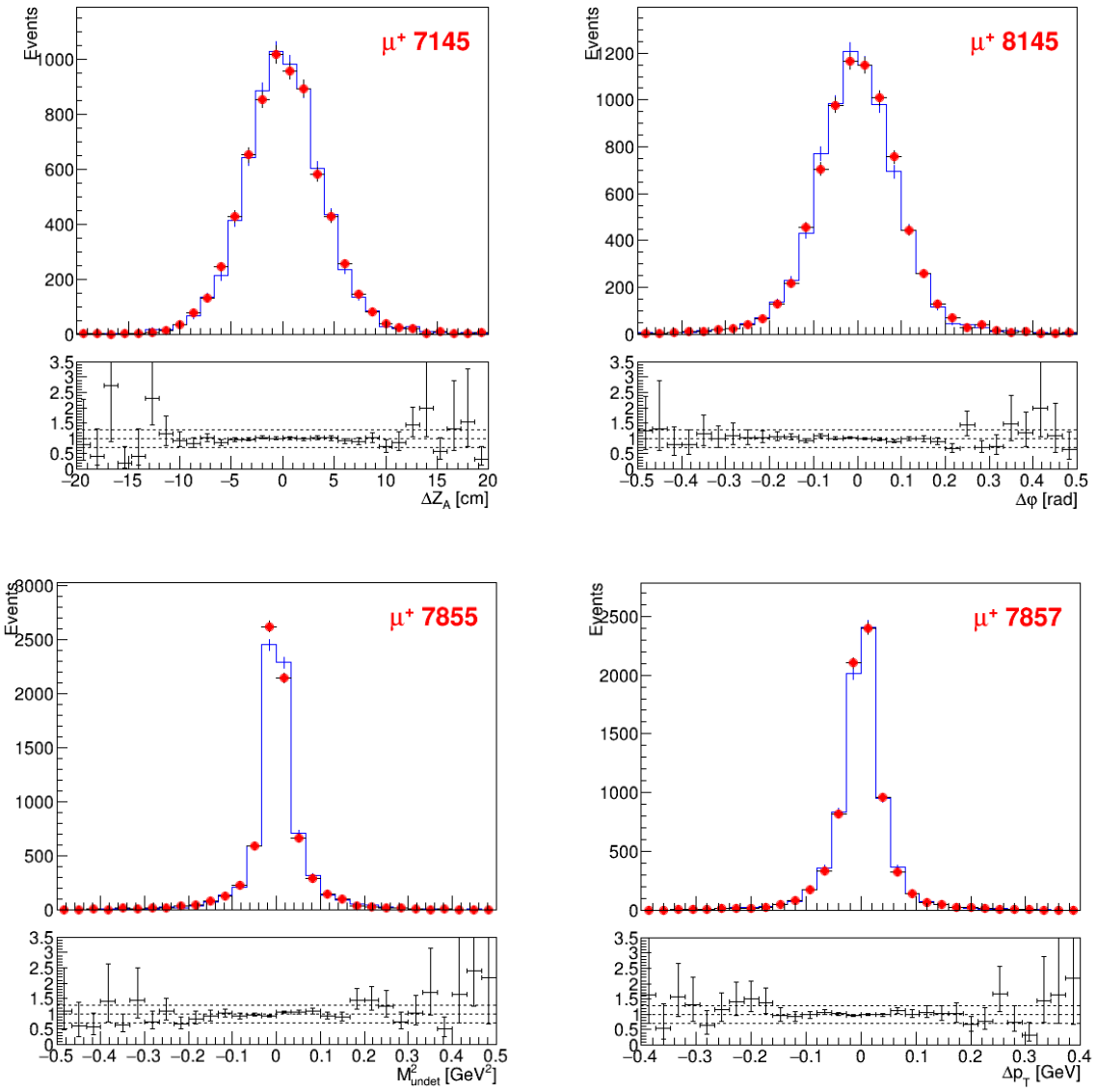

Figure 60: Exclusivity variables for exclusive ρ^0 production (P08 slot4) with all other cuts applied for μ^+ (red) and μ^- (blue) beams. Note the good agreement between the distributions of opposite beam charge.

Results

Figure 59 displays the invariant mass of the two charged-track system with all other cuts applied. A peak is clearly visible around the ρ^0 mass ($M_{\rho^0} = 775$ GeV).

Figure 60 displays the exclusivity variables for exclusive ρ^0 production with all other cuts applied. Note the good agreement between the distributions of opposite beam charge. As μ^+ and μ^- signals are compatible, we can conclude that adding CAMERA in the analysis does not seem to deteriorate the μ^+ and μ^- compatibility.

Figure 61 displays the missing energy E_{miss} of ρ^0 exclusive events. The determination of E_{miss} uses only muons and ρ^0 momenta. It is therefore very sensitive to the beam telescope and the spectrometer alignment. We can observe a slight deviation on the distributions of figure 61. The width of the distributions is mainly due to the resolution on muons momenta. No background contribution surrounds the neat peak, pointing to an effective selection of ρ^0 exclusive events.

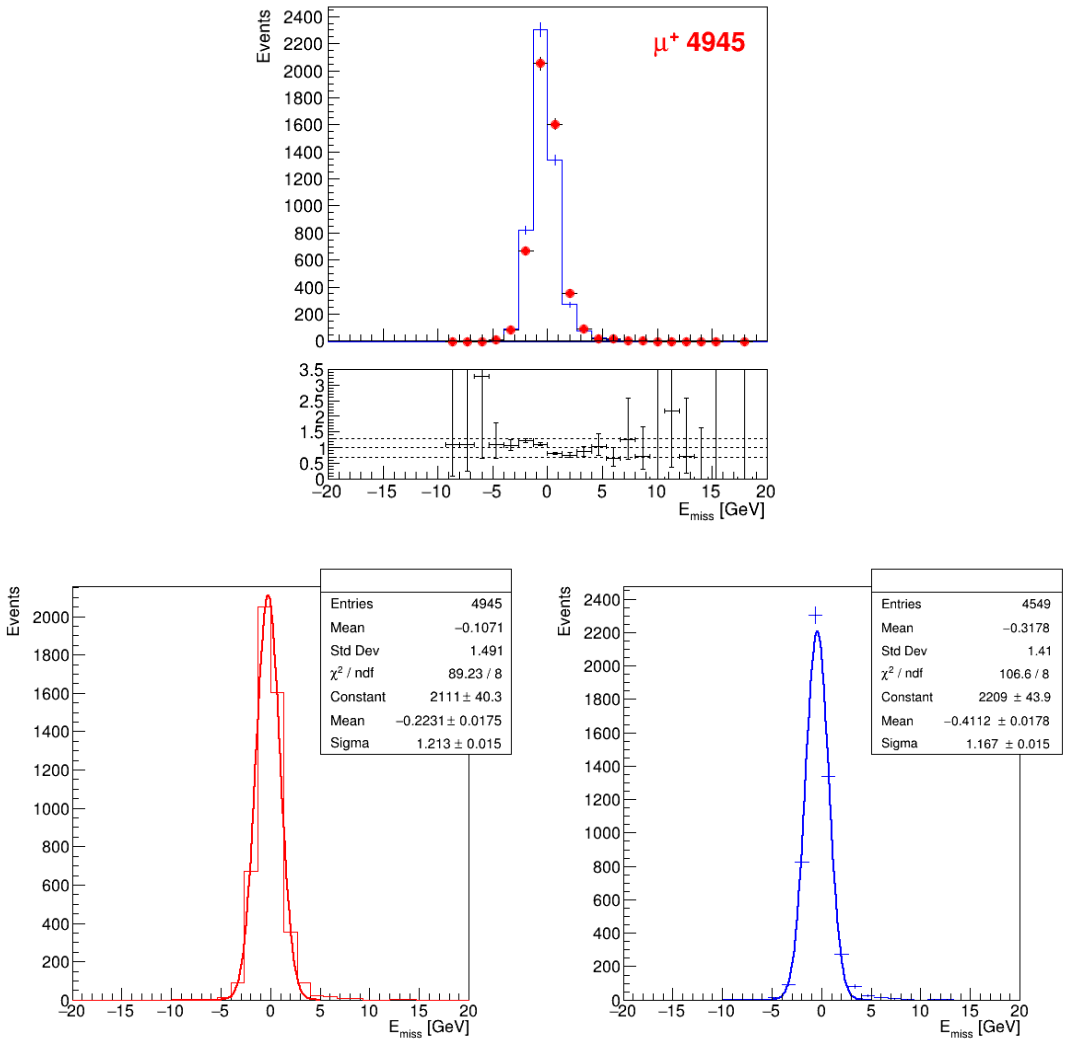

Figure 61: E_{miss} for exclusive ρ^0 production (P08 slot4) for μ^+ (red) and μ^- (blue) beams.
Top: μ^+ *vs* μ^- comparison.
Bottom: left: μ^+ data fitted with a Gaussian, right: μ^- data fitted with a Gaussian.

4.4 THE EXCLUSIVE SINGLE PHOTON DATA-SET

The selection of events of the type $\mu p \to \mu' p' \gamma$ is the starting point for the DVCS cross section extraction. Exclusive single photon events have a topology similar to the $\mu p \to \mu' p' \rho^0$ events discussed above, but instead of looking for two charged pions in the forward spectrometer, we look for a real photon. This analysis hence requires the use of the three electromagnetic calorimeters described in chapter 2 on top of the already discussed selections.

Photon selection

As photons manifest themselves in the spectrometer only *via* energy deposit in calorimeter cells, they are detected as neutral clusters in the apparatus, that is clusters non-associated to a charged track. A cluster is defined by its timing, its energy, and its position inside the calorimeter. The photon selection is done relatively to both time and energy information of the cluster. A Monte-Carlo simulation was used to define energy thresholds below which no DVCS photons are expected in the apparatus (4, 5, 10 GeV for ECAL0, 1, 2 respectively, see fig. 62). The timing of the cluster should be correlated with the timing of the event, but we decided not to include timing cuts at this stage of the analysis, as all periods were not properly calibrated yet.

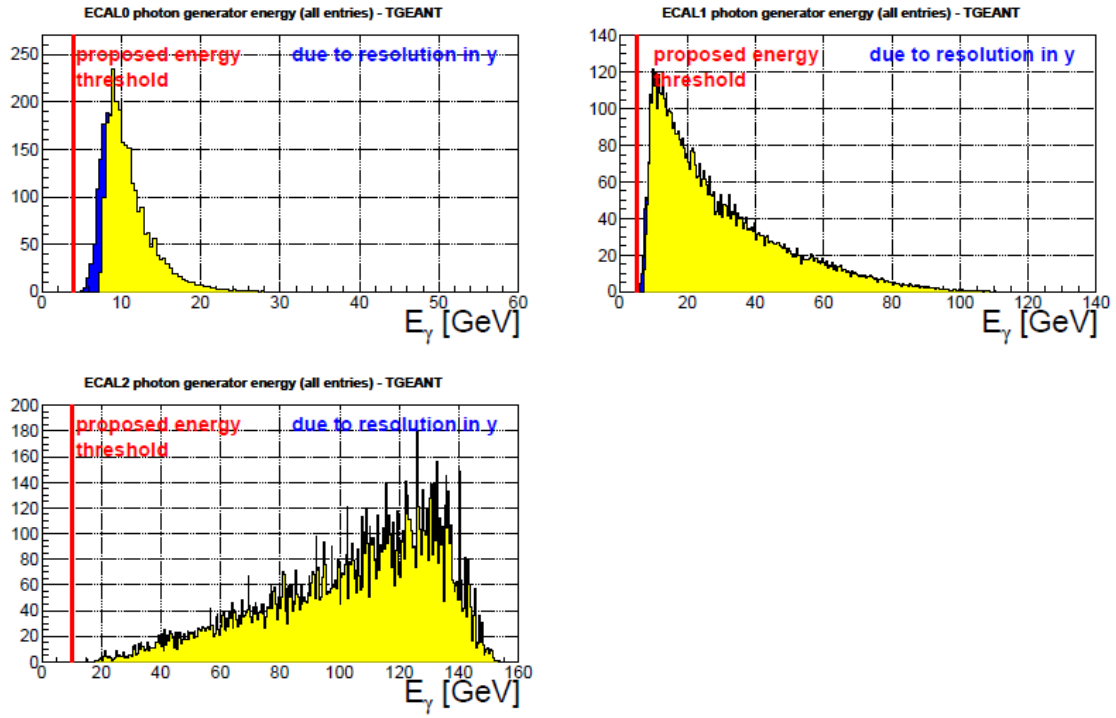

Figure 62: Distributions showing the reconstructed photon energy in ECal0 (top left), ECal1 (top right) and ECal2 (bottom left), derived by applying the event selection to a single photon Monte Carlo yield, while no threshold for the photon was applied. The photon energy threshold is shown by the red lines. Blue areas represent the impact of the poor energy resolution at small y (small ν or large x_B) affecting mainly ECAL0 and slightly ECAL1. Fig. from [42].

Since a neutral cluster is not associated to any track, it cannot be associated *a priori* to a particular vertex. This leads us to proceed in the following way to identify these exclusive events:

1. we loop over all the reconstructed vertices, keeping only those which fulfil certain quality criteria (see vertex and muons selections below);
2. if at least one vertex is retained, we loop over all the reconstructed ECAL clusters and keep only events with one single exclusive photon candidate above the DVCS threshold (see photon selection below);
3. if the event contains a single exclusive photon candidate, we loop over all the good recoil tracks reconstructed in the CAMERA detector and we build a list of candidate exclusive events from all possible combinations of good vertices, good ECAL clusters and good CAMERA tracks. The list of candidates is then reduced by applying exclusivity cuts. We finally retain events in which only one combination passes all exclusivity conditions.

$\mu p \to \mu' p' \gamma$ event selection

The cut used to select $\mu p \to \mu' p' \gamma$ events are as follows:

- incoming muon selection
  - beam track with the same requirements as for flux determination;
- vertex selection
  - vertex in the target: the longitudinal position of the vertices must satisfy the condition -318.5 cm $< z_{vertex} <$ -78.5 cm and the radial distance from the target centre at z_{vertex} must be $r_{vertex}(\text{vertex}, \text{TargetCenter}(z_{vertex})) < 1.9$ cm;
- outgoing muon selection
  - at least one outgoing muon is detected;
  - muon has triggered the Middle, Ladder or Outer Trigger (MT, LT, OT respectively);
  - outgoing muon must travel more than 15 radiation lengths;
  - the first measured point of the outgoing muon must be upstream of SM1 ($z_{first} < 350$ cm);
  - the last measured point of the outgoing muon must be downstream of SM1 ($z_{last} > 350$ cm);
- DIS cuts
  - $0.05 < y < 0.95$;
  - $1\ \text{GeV}^2 < Q^2 < 10\ \text{GeV}^2$;
- photon cuts
  - charged clusters ignored (charged track association performed by CORAL);
  - energy of the clusters above to 4, 5, 10 GeV in ECAL0, 1, 2 respectively (these thresholds take into account the value of $y > 0.05$ and $t < 0.64\ \text{GeV}^2$ within their resolution);

  - only one cluster after E_γ cuts;
  - no timing cut applied on the cluster time (as only part of the periods are produced with the new timing calibrations);
- proton cuts
  - a hit in Ring A and a hit in Ring B of CAMERA that belong to azimuthal sectors that are geometrically correlated;
  - the candidate proton has $0.1 < \beta < 1$;
  - z_A and z_B inside the domain of the scintillators A and B;
- exclusivity cuts
  - $|\Delta\varphi| < 0.4$ rad;
  - $|\Delta p_T| < 0.3$ GeV;
  - $|\Delta z|$ <16 cm;
  - $|M^2_{undet}| < 0.3$ GeV^2;
- exclusive event
  - only one primary vertex, incoming muon, scattered muon, recoil proton and γ remain after all cuts. The event is rejected otherwise.

Results

Figure 63 displays the exclusivity variables for single-exclusive photon production with all other cuts applied but the 'exclusive event' one. Note the good agreement between the distributions of opposite beam charge. As μ^+ and μ^- signals are compatible, we can conclude that adding CAMERA and ECALs in the analysis does not seem to deteriorate the μ^+ and μ^- compatibility.

The figure 64 displays the number of candidate exclusive events per events with all other cuts applied but the 'exclusive event' one. One can see that less than one percent of the events have more than one $\mu p \to \mu' p' \gamma$ candidate and are therefore rejected.

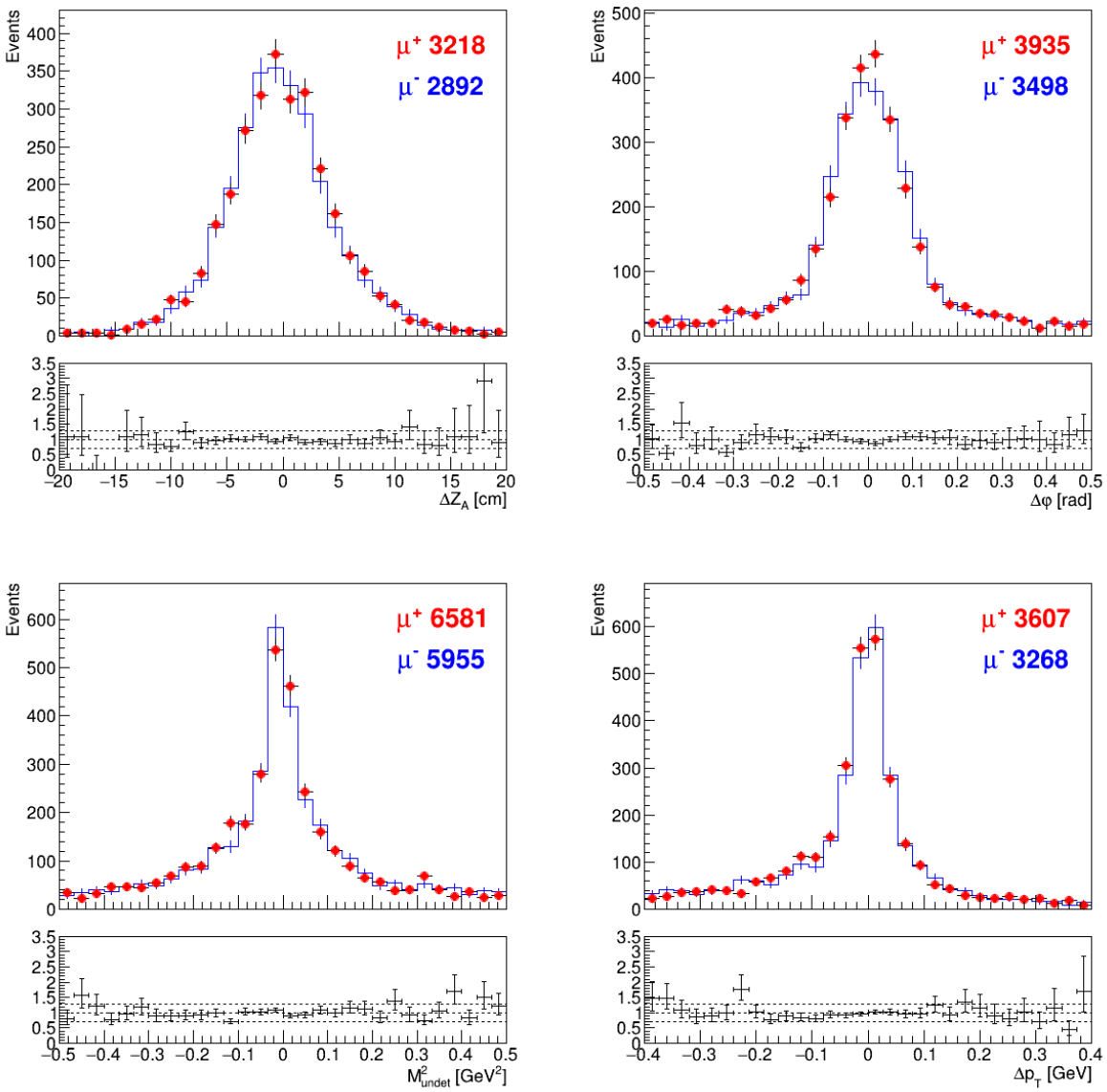

Figure 63: Exclusivity variables for exclusive photon production for μ^+ (red) and μ^- (blue) beams (P08 slot4). All other cuts are applied but the 'exclusive event' one. Note the good agreement between the distributions of opposite beam charge.

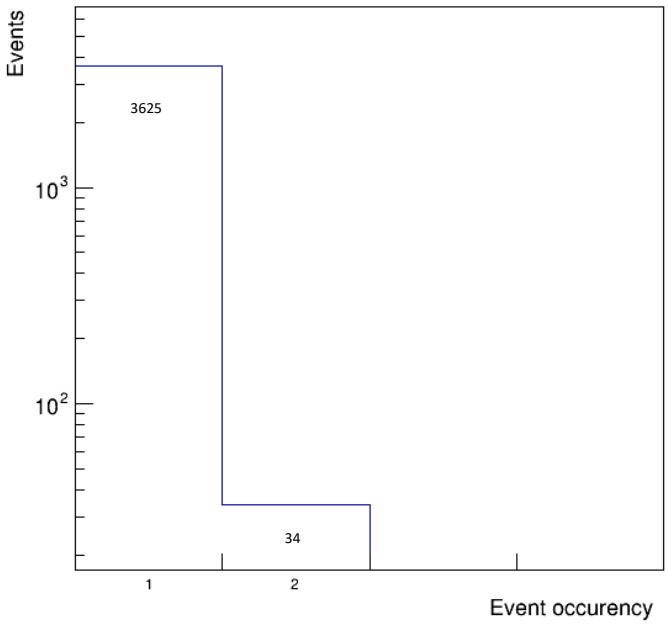

Figure 64: Number of candidate exclusive vertices per event in the selected data (P08 slot4). All other cuts are applied but the 'exclusive event' one. All event having more than one candidate exclusive vertex are rejected, this represents less than 1% of the selected events.

Quality of the selected photons

As for ρ^0, a systematic investigation of the quality of the event selection can be achieved using E_{miss} distributions. In this particular case, the observable presents an additional and strong sensitivity to the reconstructed energy of the calorimeter cluster. This control of the missing energy can be extended to a direct control of the energy distributions of clusters. Figure 65 displays the position and energy of the selected photons for one period for each calorimeter. Figure 66 displays the missing energy for the exclusive photon production reaction. Its large

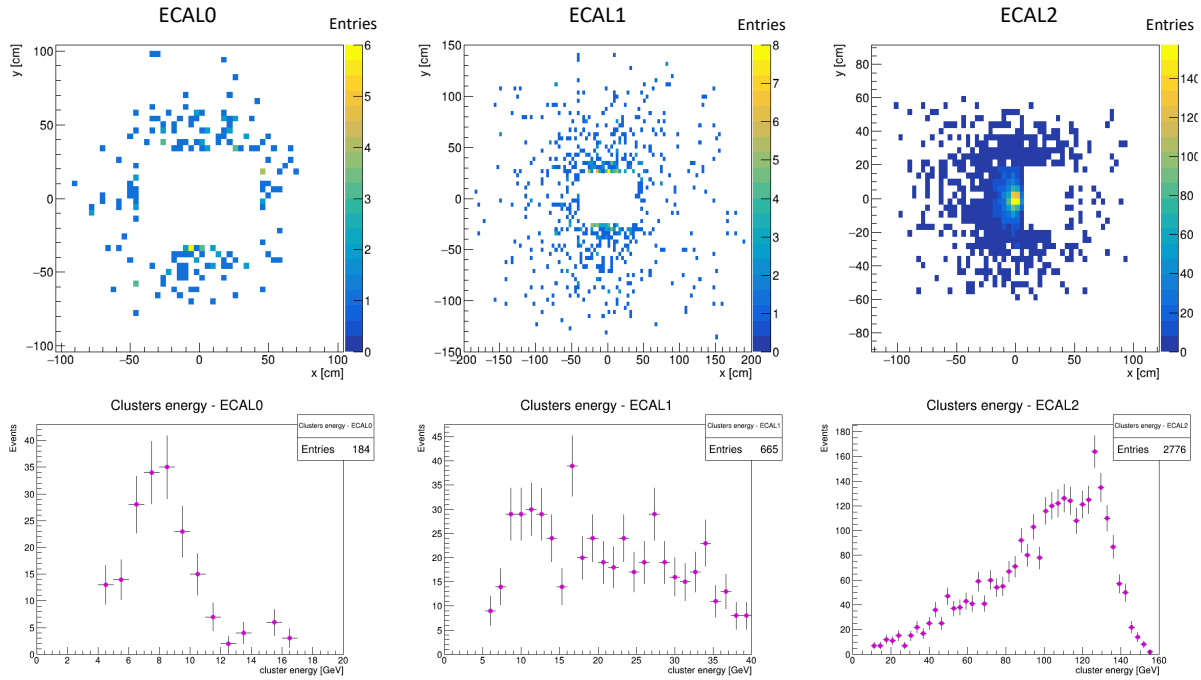

Figure 65: (x, y) position (top) and energy (bottom) of the selected clusters in ECAL0 (left), ECAL1 (middle) and ECAL2 (right) (P08 slot4).

width compared to the one for exclusive ρ^0 (see fig. 61) is the result of the convolution between the forward spectrometer and the three different calorimeter energy resolutions. The separation of E_{miss} for the different calorimeters is displayed in the same figure, and one finds Gaussian distributions with different widths and mean values. The impact of the new calibration of ECAL2 on E_{miss} and on the energy profile of the detected photon is displayed in figure 67. In the previous P08 t7 production, the E_{miss} distribution for exclusive single photon displayed a large tail at negative energy in ECAL2, as well as a spurious tail at high energy of the cluster. These problematic features have been removed by improving the ECAL2 calibration.

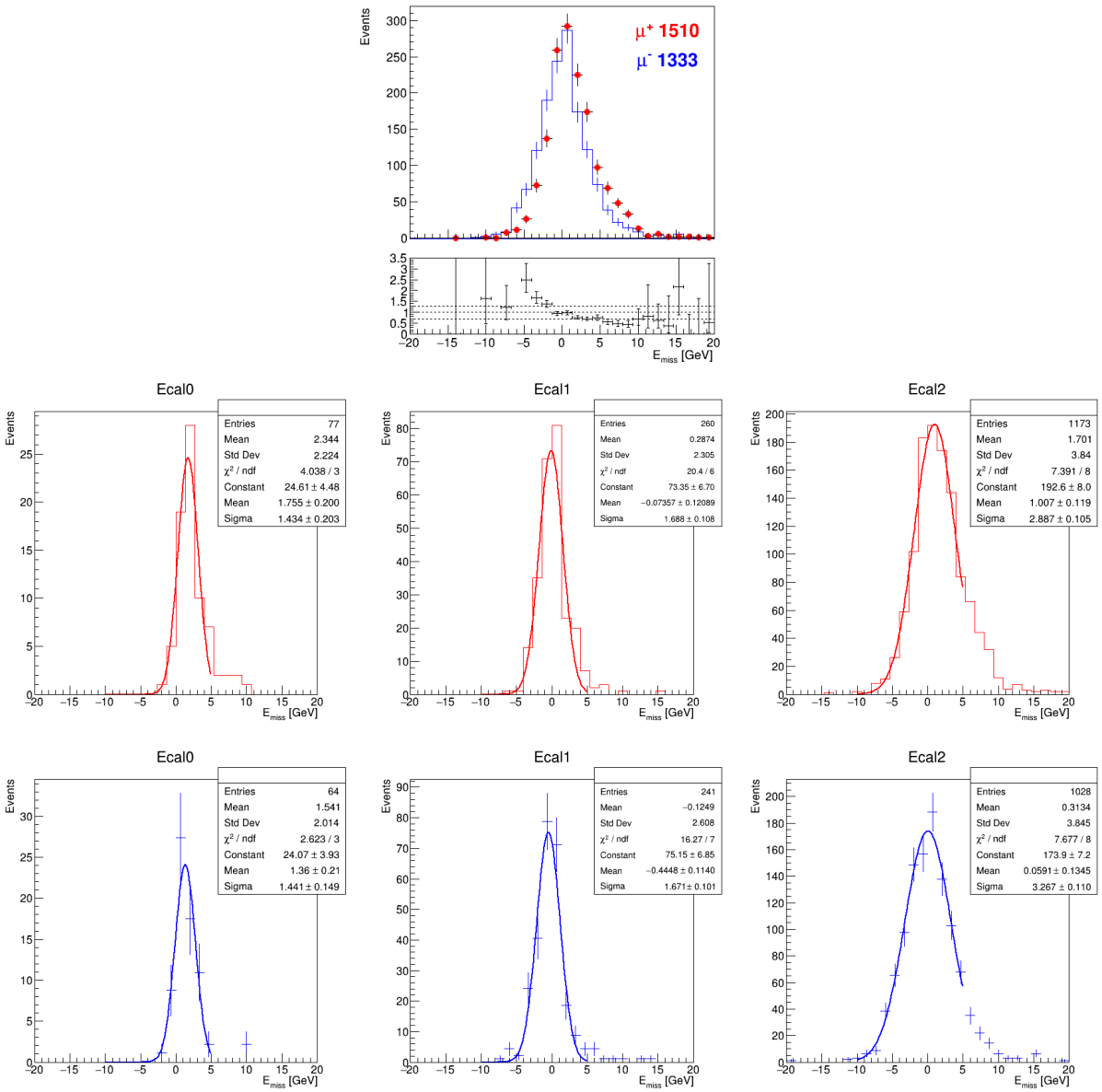

Figure 66: E_{miss} for exclusive γ production (first row) for μ^+ (red) and μ^- (blue) beams and decomposition for ECAL0, ECAL1 and ECAL2 in the first, second and last column of the 2nd and 3rd rows (P08 slot4).

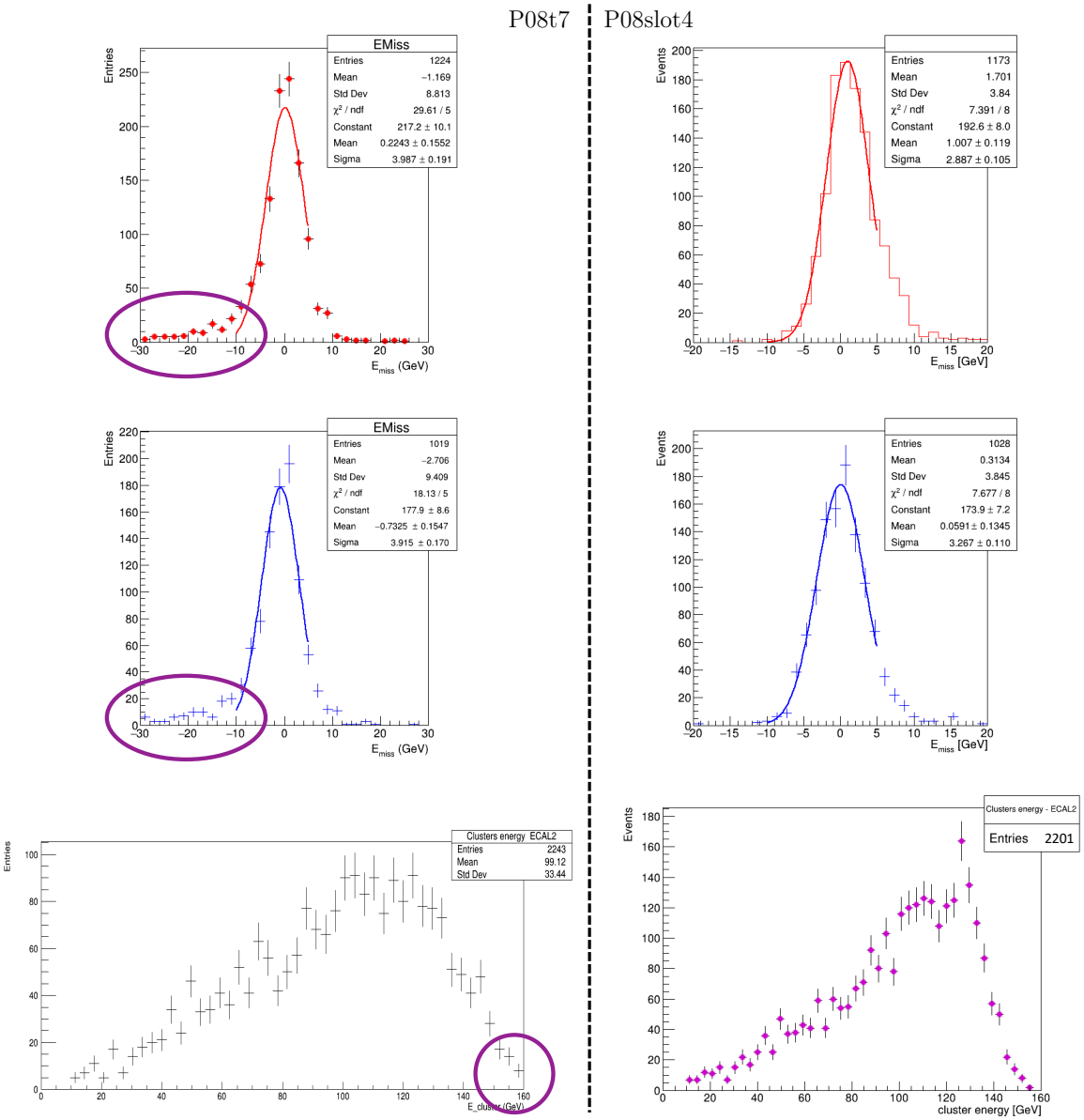

Figure 67: E_{miss} for exclusive γ production for μ^+ (top) and μ^- (middle) beams for ECAL2 and energy of the selected clusters in ECAL2 (bottom) for two different productions: P08 t7 (left) and P08 slot4 (right).

Visible π^0 contamination

Events selected accordingly to the method described above are contaminated by a remaining π^0 background. This contamination occurs when the produced π^0 decays in only one highly energetic photon above the DVCS thresholds and one photon escapes the detection for one of the three following reasons: energy below threshold, photon outside the geometrical acceptance, photon absorbed in the apparatus. Some of the smaller energy photons can be detected in one of the other calorimeter allowing for the pion identification.

This appears clearly in the data when combining all selected exclusive photons with all photons detected in ECAL0 and ECAL1 below the DVCS threshold, and plotting the invariant mass of such a system (see fig. 68). Despite a large combinatorial background, a peak around the π^0 mass appears clearly pointing to a contamination given either by exclusive π^0 production or by semi-inclusive π^0 production. We call this contamination: 'visible' π^0 background. Indeed, this points towards the fact that, besides the visible π^0 contamination, some photons out of pion decay might propagate out of the calorimeters acceptance or get absorbed, and be irremediably lost. These are called 'invisible' π^0 background.

The visible π^0 background is removed by rejecting all events having entries in this plot (fig. 68) ± 20 MeV/c^2 around the PDG π^0 mass. Most of these events have small ν, and for $10 < \nu < 32$ GeV, this contamination reaches around 10% of the signal. Note that photons in ECAL2 with energy below the DVCS threshold do not contribute to the π^0 signal but only to the background in the $M_{\gamma\gamma}$ spectrum, as it has been shown by the exclusive π^0 production analysis lead on 2012 data [7]. The invisible π^0 background will be shortly discussed in chapter 5.

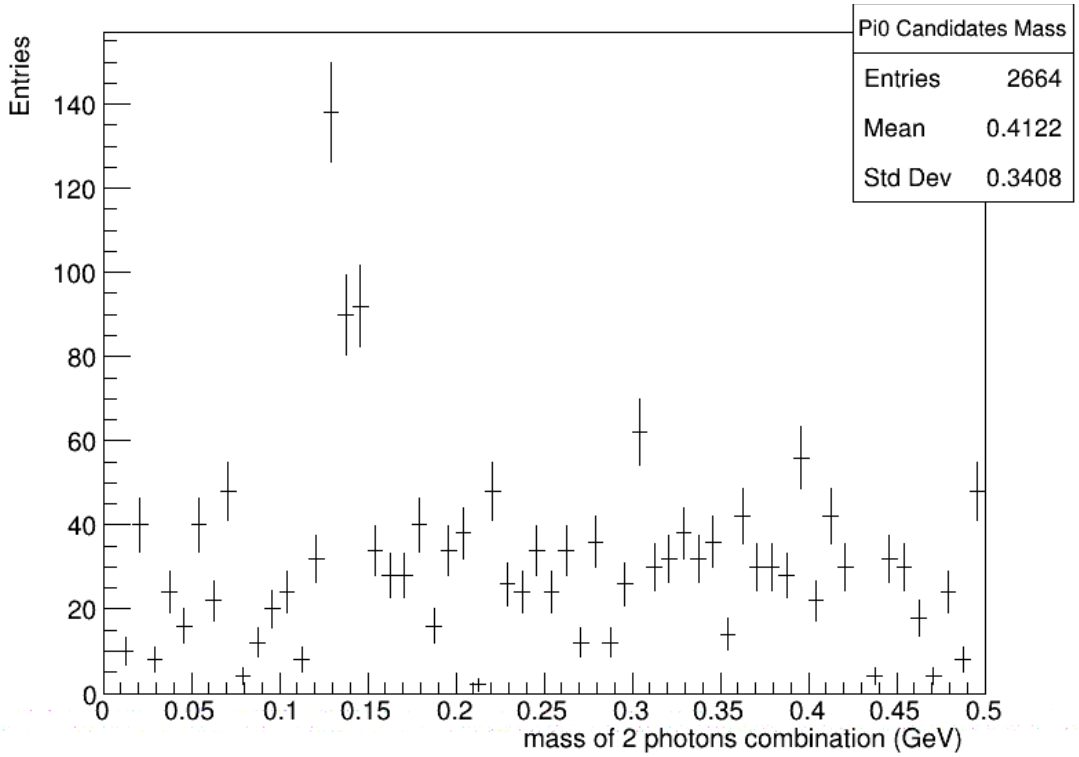

Figure 68: Two photon invariant mass in the exclusive single photon sample selected at the end of the previous section.

ϕ modulation of the exclusive single photon events

Fig. 85 presents the exclusive single photon events obtained in P08 slot4 as a function of ϕ for μ^+ and μ^- beams in three ν ranges, as they were defined in the 2012 analysis [5]. Only the visible π^0 contribution has been removed. Both beam charge distributions are in good agreement even though no bad-spill rejection is yet applied, and this is an important result which was not achieved in 2012 analysis due to the high intensity difference between the two muon beams. Obviously, small differences of interest should appear for $\nu < 80$ GeV. They are nonetheless invisible due to the small statistics of one period.

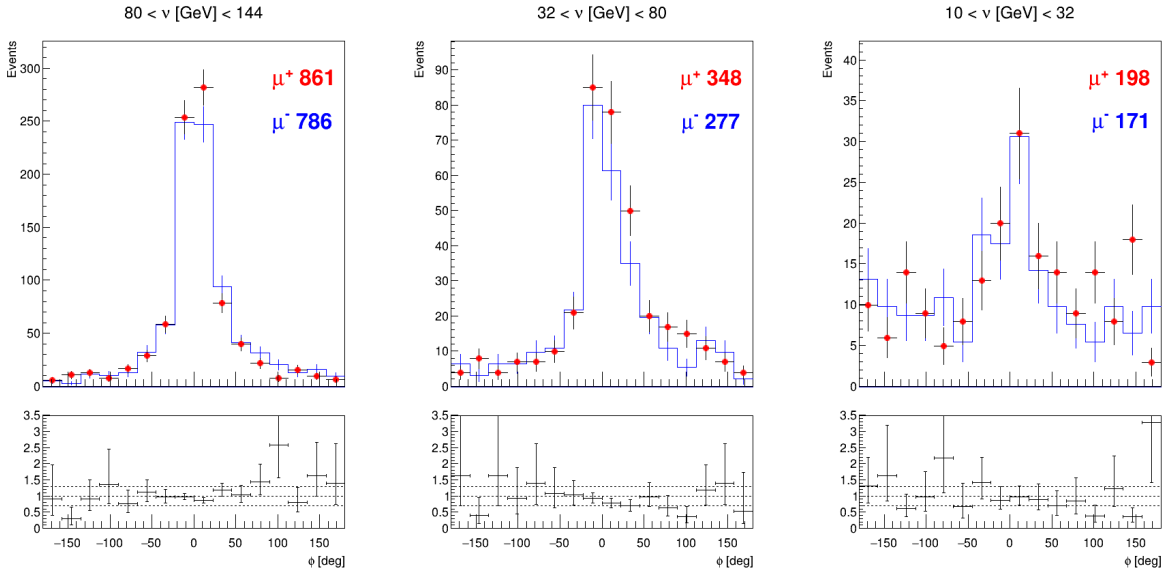

Figure 69: Exclusive single photon events as a function of ϕ for μ^+ (red) and μ^- (blue) beams in 3 ν ranges. The visible π^0 contribution has been removed.

4.5 SUMMARY OF THE 2016 DATA

Flux

The result of the flux analysis per period is displayed in figure 70. The total flux collected using μ^+ (μ^-) beam is $8.06 \cdot 10^{12}$ ($6.95 \cdot 10^{12}$). The ratio between the two fluxes is 1.16, as the goal was to collect comparable fluxes for both muon charge. This is about three times more than the data collected for the 2012 test run, and represents approximately a third of the combined 2016 and 2017 statistics (the proton intensity on T6 was increased by a factor two for the 2017 run).

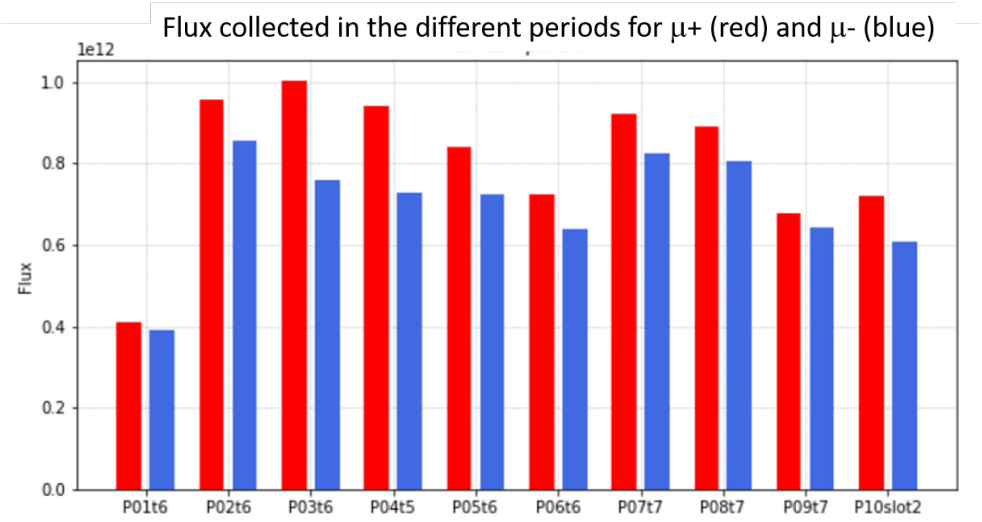

Figure 70: Flux for all 2016 periods for μ^+ (red) and μ^- (blue) beams.

DIS and ρ^0 event selection

A summary of the DIS data is displayed in figure 71. μ^+ and μ^- are normalised to a same muon flux (10^{12}). The first comment is that, besides P10, all period display reasonable agreement between μ^+ and μ^-. This confirms that the decision to run using equivalent intensity for both charges was correct. If the spectrometer was stable one would get a constant number of count across all periods. We can see that it is not the case for the total number of DIS events. Decomposing this distribution over each trigger helps to decipher this distribution.

One can see that steps are introduced by three different states of the OT and two different states of the MT. The OT changes are due to changes in the hodoscopes: some slats were improved along the year, increasing the number of detected events. The MT change is due to the fact that a correlation between horizontal (Y) and vertical (X) MT hodoscopes was required for this trigger for the first three periods, while only horizontal MT was used for the rest of the year. A discrepancy between P03 μ^- and μ^+ remains to be explained. A loss of events due to the high intensity beam is visible in P10 μ^+. The number of selected exclusive ρ^0 events increases along the year following the different trigger conditions, reinforcing the discrepancy

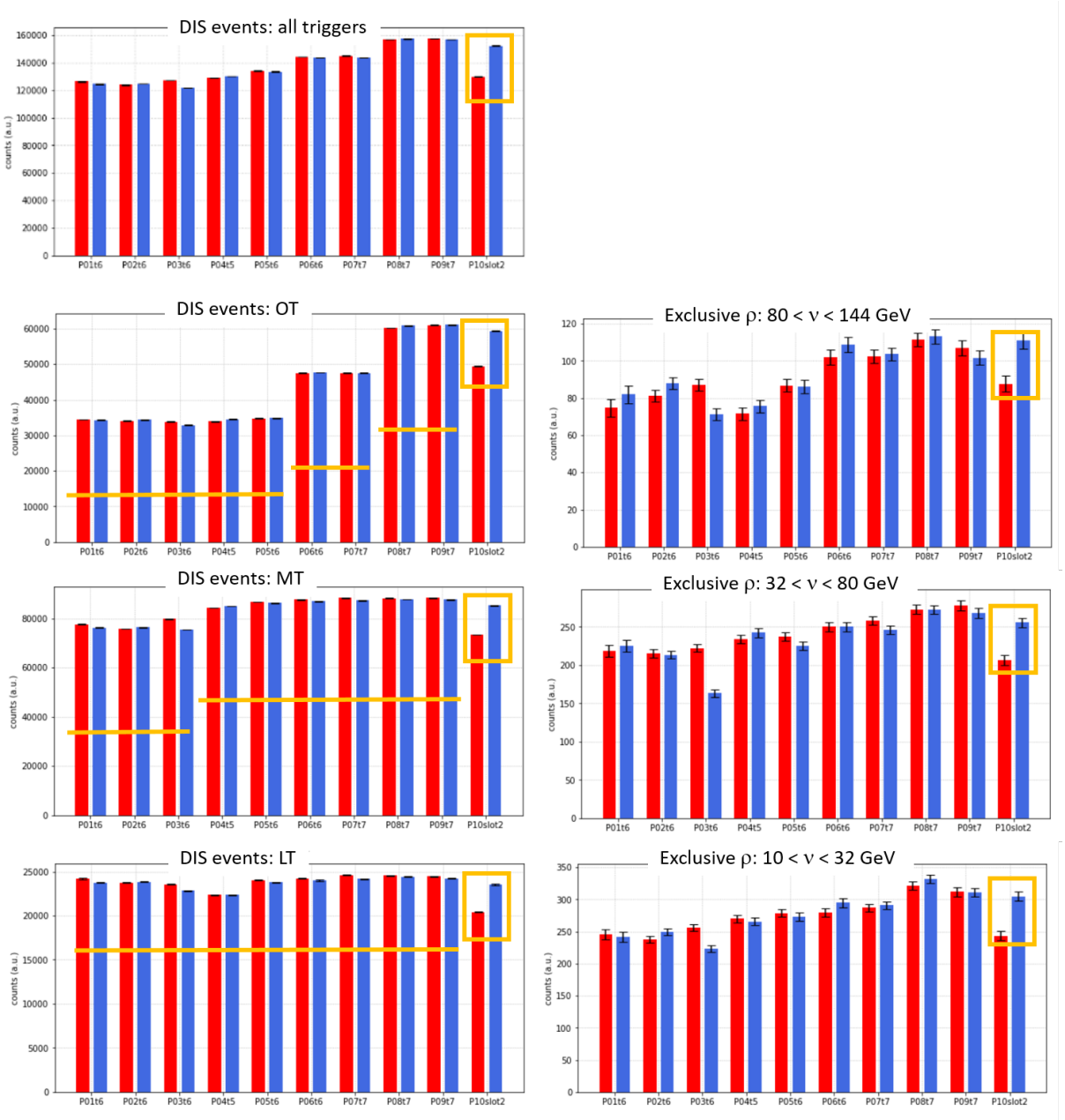

Figure 71: Summary of number of DIS events for all triggers and every trigger and number of exclusive ρ^0 events for 3 domains of ν for all the periods and μ^+ (red) and μ^- (blue) beams. All the numbers are normalised to a same muon flux (10^{12}).

between P03 μ^- and μ^+. The P10 μ^- and μ^+ discrepancy for DIS is obviously propagated to the ρ^0 events.

The different states of the trigger along the years will have to be addressed in the simulation in order to properly reproduce the apparatus. P10 should not be used for further analysis as it displays an incompatible signal between μ^+ and μ^-.

Exclusive single-photon event selection

Figure 72 summarises the number of exclusive single-photon events for all the periods in 3 ν ranges and for exclusive single-photon photons collected in the different electromagnetic calorimeters. Alike DIS and exclusive ρ^0 production, an increase of exclusive single-photon events should be expected for the last periods. This progression is observed in ECAL0 and ECAL1 but it is not observed in ECAL2 nor in the middle and large ν bin. Counts in ECAL2 for P06 mark a clear discontinuity which remains to be explained. Those variations justify the need for more careful calibration of calorimeters, in particular the one actually ongoing for ECAL2 (see fig. 67).

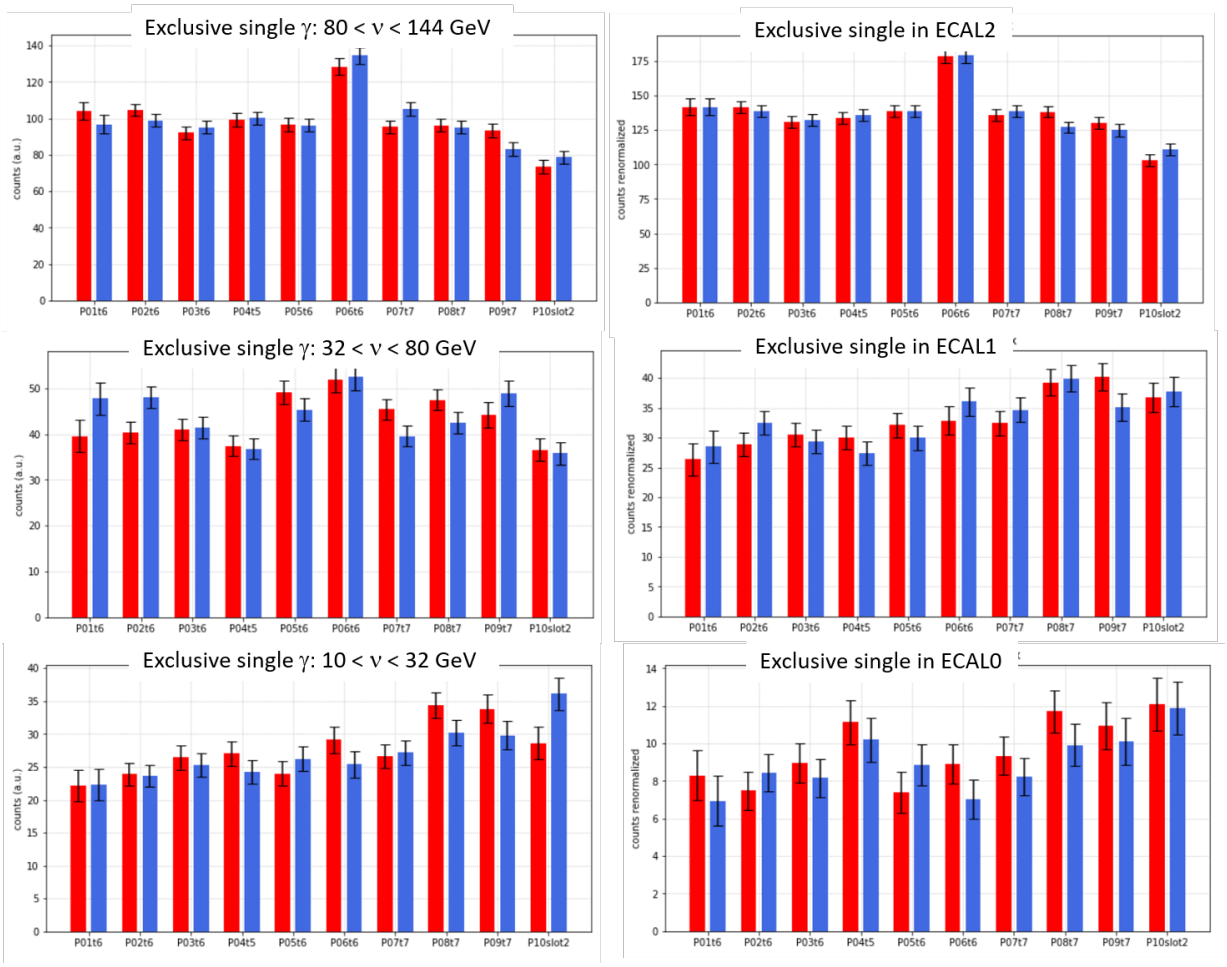

Figure 72: Summary of number of exclusive single-photon events for 3 domains of ν and for the 3 ECALs for all the periods and μ^+ (red) and μ^- (blue) beams. All the numbers are normalised to a same muon flux (10^{12}).

This systematic study of all periods from COMPASS 2016 data shows that it would be unreasonable to merge periods at this stage of the analysis, as this merge would not bring more physics insight at the present time. This analysis is nonetheless very encouraging as it displays a good compatibility between μ^+ and μ^- data for all periods taken with similar beam intensity. The careful systematic study and comparison of the data on a period-basis is a very effective

method to investigate its quality, and sharpen our knowledge about the state of the apparatus as well. Updated productions of the data are ongoing, including more accurate calibrations of electromagnetic calorimeters and a refined data quality analysis. The analysis of the freshly produced P08 slot4 period including said calibrations attests improvements in missing energy and energy of the selected cluster distributions for ECAL2.

5

TOWARDS THE DVCS CROSS SECTION AND ITS t-SLOPE

I will summarise in this chapter how we intend to extract the t-slope of the DVCS cross section out of the data presented above. A detailed presentation can be found in [42]. As the analysis is still ongoing, I will present here the main needed steps and, when relevant, the first associated results.

5.1 FROM EXCLUSIVE SINGLE-PHOTON EVENTS TO DVCS CROSS SECTION

The experimental extraction of the cross section is carried out by binning the data. In the following, I will consider a (Q^2, ν, t, ϕ) bin and I will omit average signs around quantities:

$$\frac{\mathrm{d}^4\sigma(lp \to lp\gamma)}{\mathrm{d}Q^2\mathrm{d}x_B\mathrm{d}|t|\mathrm{d}\phi} \quad \text{stands for} \quad \left\langle \frac{\mathrm{d}^4\sigma(lp \to lp\gamma)}{\mathrm{d}Q^2\mathrm{d}x_B\mathrm{d}|t|\mathrm{d}\phi} \right\rangle_{Q^2,\nu,t,\phi}$$

where $\mathrm{d}\sigma = \frac{1}{2}(\mathrm{d}\sigma^{\overleftarrow{\pm}} + \mathrm{d}\sigma^{\overrightarrow{-}})$.

The $lp \to lp\gamma$ cross section

The number of counts in one bin for the $lp \to lp\gamma$ process relates to its associated cross section in the following way:

$$\frac{\mathrm{d}^4\sigma(lp \to lp\gamma)}{\mathrm{d}Q^2\mathrm{d}\nu\mathrm{d}|t|\mathrm{d}\phi} = \frac{1}{\delta Q^2 \delta\nu \delta t \delta\phi} \frac{1}{2} \sum_{\mu^\pm} \frac{1}{\mathcal{L}} \frac{1}{a} \sum_{e}^{\text{data}} 1 \tag{96}$$

where I have denoted with δX the width of the bin in dimension X.

The first sum is done over the two beam charges while the second simply loops over the events (e) selected in the data according to the method details in the previous chapter for the considered bin $\delta Q^2 \delta\nu \delta t \delta\phi$ and beam charge.

$\mathcal{L}$ stands for the integrated luminosity of the considered beam charge:

$$\mathcal{L} = \frac{\rho_{\mathrm{LH}_2} \mathcal{N}_\mathcal{A} \mathrm{L}}{M_p} (1 - c_{vdt}) \Phi \tag{97}$$

and does not depend on the bin. It relates the flux Φ described in equation 88 to the density of the target $\rho_{\mathrm{LH}_2} = 0.0704$ g/cm^3, its effective length $\mathrm{L} = 240$ cm, the Avogadro number $\mathcal{N}_\mathcal{A} = 6.022 \cdot 10^{23}$ mol^{-1} and the molar proton mass $M_p = 1.0078$ g/mol. c_{vdt} accounts for the dead-time of the veto on the triggers.

a stands for the acceptance of the considered bin. It depends on the bin and the beam charge, and accounts for any phase-space inefficiency of the apparatus. Acceptances are obtained *via* Monte-Carlo simulation and are discussed in a further section of this chapter.

The $\gamma^* p \to \gamma p'$ cross section

As we are interested in the DVCS cross section independently of the experimental process used to radiate a virtual photon on the proton, we need to get rid of the lepton scattering part of this quantity. This is doable following the convention provided by Hand [36, 57], re-weighting each event with a kinematic factor Γ, called transverse virtual photon flux:

$$\Gamma(Q^2, \nu) = \frac{\alpha_{em}}{2\pi} \frac{1 - x_B}{Q^2 y E} \left[y^2 \left(1 - \frac{2m_\mu^2}{Q^2} \right) + \frac{2}{1 + \frac{Q^2}{\nu^2}} \left(1 - y - \frac{Q^2}{4E^2} \right) \right]. \tag{98}$$

This factor is evaluated event by event. The $\gamma^* p \to \gamma p'$ differential cross section then relates to the events in the following way, denoting kinematic variables values for the considered event in the sum with the subscript e:

$$\frac{\mathrm{d}^2\sigma(\gamma^* p \to \gamma p')}{\mathrm{d}|t|\mathrm{d}\phi} = \frac{1}{\Delta Q^2 \Delta\nu \delta t \delta\phi} \frac{1}{2} \sum_{\mu^\pm} \frac{1}{\mathcal{L}} \sum_{\nu, Q^2} \frac{1}{a} \sum_e^{\text{data}} \frac{1}{\Gamma(Q_e^2, \nu_e)} \tag{99}$$

where ΔX is the total integration domain of the variable X. The second sum runs over all bins $\delta Q^2 \delta\nu$ inside $\Delta Q^2 \Delta\nu$ and the third one runs over all events inside the bin $\delta Q^2 \delta\nu \delta t \delta\phi$. It should be noted that the two quantities defined by equations (98) and (99) are not observables.

The DVCS cross section

At this stage, the single-photon data selected still contains four contributions: a DVCS, a BH, a DVCS-BH interference and a π^0 one:

$$\sigma(\gamma^* p \to \gamma p') = \sigma^{\text{DVCS}}_{\gamma^* p \to \gamma p'} + \sigma^{\text{BH}}_{\gamma^* p \to \gamma p'} + \sigma^{\text{Int}}_{\gamma^* p \to \gamma p'} + \sigma^{\pi^0}_{\gamma^* p \to \gamma p'}. \tag{100}$$

The π^0 contamination corresponds to the case described in chapter 4. The three last items on the list need to be subtracted from the data. The Bethe-Heitler and π^0 contributions are estimated using a weighted Monte-Carlo simulation, while interferences are suppressed integrating ϕ over 2π (eq. 48,50):

$$\frac{\mathrm{d}\sigma^{\text{DVCS}}_{\gamma^* p \to \gamma p'}}{\mathrm{d}|t|} = \frac{1}{\Delta\phi \Delta Q^2 \Delta\nu \delta t} \frac{1}{2} \sum_{\mu^\pm} \frac{1}{\mathcal{L}} \sum_{\phi, \nu, Q^2} \frac{1}{a} \left[\sum_e^{\text{data}} \frac{1}{\Gamma(Q_e^2, \nu_e)} - k_{\text{BH}} \sum_e^{\text{BH}} \frac{w_{\text{BH}}}{\Gamma(Q_e^2, \nu_e)} - k_{\pi^0} \sum_e^{\pi^0} \frac{w_{\pi^0}}{\Gamma(Q_e^2, \nu_e)} \right] \tag{101}$$

where the second sum runs over all bins $\delta Q^2 \delta\nu \delta\phi$ inside $\Delta Q^2 \Delta\nu \Delta\phi$. The sums on Bethe-Heitler and π^0 events represent the loop over corresponding simulated events passing the same exclusive single-photon selection as for the data. Those contributions have a per-event kinematic weight w_{BH} (w_{π^0} respectively) and a normalisation constant k^{BH} (k^{π^0}). It is then possible to fit an exponential to the values of $\frac{\mathrm{d}\sigma^{\text{DVCS}}_{\gamma^* p \to \gamma p'}}{\mathrm{d}|t|}$ obtained in the different t bins as it has been done for the 2012 test-run [5].

5.2 HANDLING MONTE-CARLO

The simulation of the experiment is the backbone of this analysis as its contribution enters directly the expression of the cross section. Alike many other high-energy physics experiments, COMPASS simulation is based on a Geant4 Monte-Carlo setup that propagates events generated by specific physics generators into a model of the apparatus.

The simulation software is named TGeant and its full documentation can be found in reference [60]. It provides output files compatible with the one obtained in real data taking, simulating hits in detectors. These files are then reconstructed inside CORAL, just as real data would be, and can therefore be analysed using PHAST.

Physics generators

Two different physics generators are needed to attempt to reproduce the experiment. One is aimed at simulating the semi-inclusive events while the other reflects exclusive processes.

LEPTO [39], on one hand, is used to account for semi-inclusive event generation to estimate the inclusive part of the pion contamination. We are, as I am writing, producing such semi-inclusive samples in this perspective, but we do not have any results associated yet to show.

On the other hand, exclusive events are generated using HEPGen++ [61, 62]. This generator has been designed specifically for COMPASS and offers a wide variety of exclusive processes. It is a weighted generator, meaning it provides for each generated event a weight w that contains the information relative to the cross section of the considered process.

HEPGen++ serves three purposes in this analysis. It includes an exact analytic calculation of the Bethe-Heitler contribution to the exclusive single photon cross section made by Pierre Guichon [35] that accounts for the muon mass, which is used for BH subtraction. It includes as well a model for the DVCS and interference contributions that partially incorporates muon-mass effects, at least up to its contribution to the propagator of the corresponding graphs. Lastly it provides a model for exclusive π^0 generation based on Goloskokov and Kroll's predictions [34] that will be used for subtracting the exclusive part of the remaining π^0 background in the data, which sample is also under preparation and not presented in this work.

MC setup

The accurate description of the experimental apparatus in the MC simulation requires three types of inputs: real data beam-files, detectors' efficiencies, and alignment. The beam files contain all measured incoming muon momenta of a certain charge during one data period registered by the random trigger. These muons are used randomly as a starting point for the generation of events. Detectors' efficiencies reflect the ability of detectors, channel by channel, to detect an incoming particle. Alignment provides the position of each detector. The target and CAMERA scintillators are individually positioned to match the information extracted throughout the calibration procedure (see chapter 3).

As a consequence, it means that, in principle, each MC sample has to be processed differently for each period, as input parameters vary from one period to another. It implies that one needs

4(physics processes)×10(periods)×2(beam-files)= 80 different MC samples to be generated, only for the first year of data taking.

CAMERA simulation

Inside TGeant, CAMERA material budget is fully modelled. Nonetheless, the simulation does not propagate the photons sparkled by a charged particle flying through its scintillators, and the registered information solely consists in the hit position and its associated energy deposit. As CAMERA informations are not treated at CORAL level, I smear this information at PHAST level in order to account for CAMERA resolution, and apply CAMERA efficiencies.

The goal is to go from a non smeared timing of the hit t at known position z to two timings smeared at both ends of the scintillator, which can then be treated exactly as in the data. The first step consists in shifting t by $\sqrt{x^2+y^2+(z+900)^2}/30$, as the origin of time in the simulation is taken to be the moment when the incoming muon is shot 900 metres ahead of the target. I then use the calibrated value of the light-speed in the considered scintillator to propagate the hit both to the upstream and downstream photo-multipliers inverting the system:

$$\begin{cases} t = \frac{t^u+t^d}{2} \\ z = \frac{1}{2}V(t^u-t^d)+C \end{cases} \quad \text{which leads to} \quad \begin{cases} t^u = t + \frac{z-C}{V} \\ t^d = t - \frac{z-C}{V} \end{cases} \tag{102}$$

Finally t^u and t^d are smeared independently according to a Gaussian law which width is tuned in order to reproduce the resolution of $\Delta z = z^{cam} - z^{spec}$ obtained in the data.

The constants $C_{A_iB_j}$ introduced for the time-of-flight in the data have no reason to be introduced in the simulation, as the timing of A and B hits are not shifted with respect to one another. There are all set to zero.

The φ calibration is taken to be the same as for the data, given that all scintillators have been placed accordingly. The φ resolution arises mainly from the geometry of the scintillator and does not need to be tuned.

5.3 THE π^0 CONTAMINATION

The Monte-Carlo study of π^0 contamination is still ongoing, but as it is the main background of the experiment, I want to review quickly the related issues.

As discussed in the previous chapter, part of this contamination is 'visible'. This occurs when both photons associated to the π^0 decay are detected in calorimeters: one of them being mistaken to belong to a candidate exclusive single-photon event, the other being below DVCS calorimeter thresholds but still inside the acceptance of the apparatus. This part of the contamination can be removed from the data cutting around the π^0 mass in the two-photon mass spectrum, but it pinpoints cases in which the second photon might have escaped detection. This background has therefore to be estimated using simulation, and can be normalised to the visible part of the signal.

The tricky point arises from the fact there are two sources of π^0: semi-inclusive and exclusive π^0 production. It follows that the term in equation 101 has to be substituted according to:

$$k_{\pi^0} \sum_{e}^{\pi^0} \frac{w_{\pi^0}}{\Gamma(Q^2_e, \nu_e)} \longrightarrow r_{incl/excl}\, k_{\text{incl}} \sum_{e}^{\text{incl}\pi^0} \frac{1}{\Gamma(Q^2_e, \nu_e)} + (1 - r_{incl/excl})\, k_{\text{excl}} \sum_{e}^{\text{excl}\pi^0} \frac{w_{\text{excl}\pi^0}}{\Gamma(Q^2_e, \nu_e)}, \tag{103}$$

where $r_{incl/excl}$ is the ratio of inclusive *vs* exclusive π^0 production, k_{incl} (respectively k_{excl}) the normalisation constant of the inclusive (exclusive) MC sample. Unfortunately, none of their respective cross sections is known well enough to allow for a direct normalisation of these contributions. If k_{incl} and k_{excl} can be easily determined using the visible π^0 contamination, one needs another independent data-set to disentangle the ratio $r_{incl/excl}$. The problem is that this ratio is specific to a certain set of cuts, as it produces the noise profile of the analysis. One way to deal with this problem is to relax slightly the exclusivity cuts of the single-photon analysis and select events inside the π^0 mass region in the two-photon mass spectrum to produce a new data-set which remains quite similar to the one of interest. Then, try to fit the background of distributions adjusting the value of $r_{incl/excl}$. In 2012 this ratio was taken to be $r_{incl/excl} = 0.9$ [42].

5.4 ACCEPTANCES

Acceptances of the experiment are evaluated using the MC simulation. They account for all phase-space inefficiencies (induced either by geometry or detectors efficiencies), and regulate the phase-space in which it is reasonable to extract a result. In principle, acceptances do not depend on the physics but solely on the apparatus, as long as they are evaluated in small bins and all independent kinematic variables. The acceptance correction writes, for a bin $\delta\Omega = \delta\nu\delta Q^2\delta t\delta\phi$:

$$a(\delta\Omega_r) = \frac{N_r(\delta\Omega_r)}{N_g(\delta\Omega_g)}, \tag{104}$$

where N_g is the number of generated events having generated kinematic variables inside $\delta\Omega$ and N_r is the number of reconstructed events having reconstructed kinematic variables inside $\delta\Omega$. Defined in this way, acceptances also account for migration of events from one bin to another during the reconstruction process due to kinematic smearing and resolutions effects. In the particular case of our analysis, as we already integrate target acceptance effects inside the flux, it is important to define $N_g(\delta\Omega_g)$ as being the number of generated events that pass the same cuts as the flux. $N_r(\delta\Omega_r)$, on the other hand, is defined to be the number of events that pass the entire set of cuts for the exclusive single-photon production selection.

To extract acceptances for the 2016 data, we chose to use the DVCS weight of the HEPGen++ generator. Results are displayed in figure 73 as a function of ϕ, t and Q^2 and in figure 74 as a function of ϕ, Q^2 and ν. They are presented inside the domain $8 < \nu < 32$ GeV of interest for the study of the DVCS cross section, where the subtraction of the BH contribution is small enough. Acceptances are reasonably flat everywhere except for the region of small ν and high Q^2, where they tend to zero around $\phi = \pi$. It means that COMPASS can expect to extract

valuable information about the cross section in all other bins displayed. This range is extended with respect to the 2012 data, as the acceptance coverage has been improved for small ν and high Q^2 by the outer extension of ECAL0. The value around 30% accounts for efficiency of the apparatus, including the large photon absorption in the target and all detectors, rather than reduced kinematic coverage of the experiment.

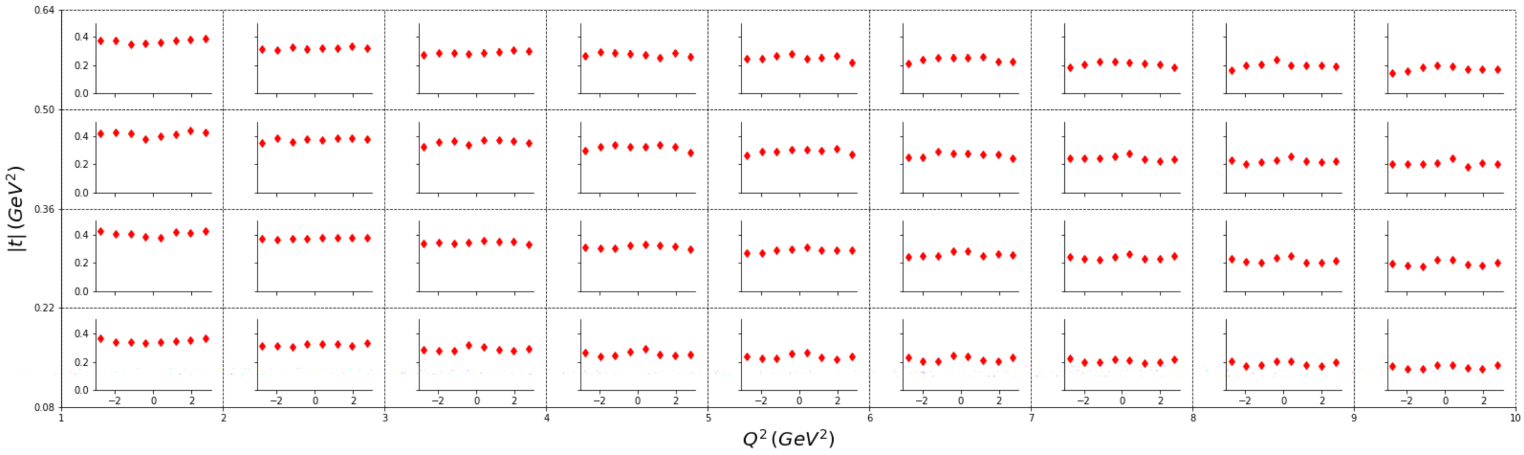

Figure 73: Acceptances for μ^+ MC as a function of t, Q^2 and ϕ. The inner y-axis displays the value of the acceptance while the x-axis displays ϕ in radian).

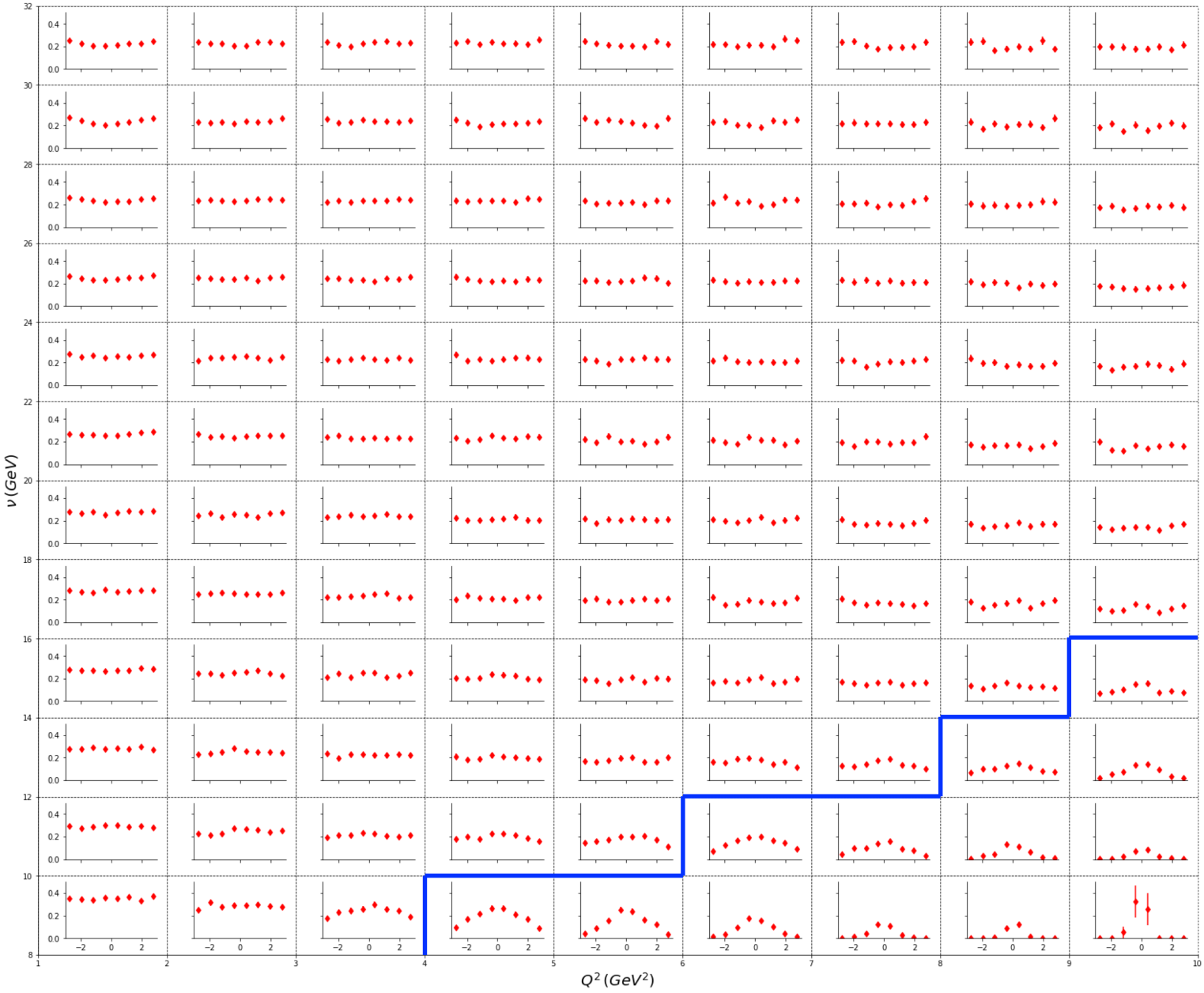

Figure 74: Acceptances for μ^+ MC as a function of ν, Q^2 and ϕ, the inner y-axis displays the value of the acceptance while the x-axis displays ϕ in radian. Bins below the blue line reach less than 10% acceptance, and will not be considered for the final analysis.

5.5 THE BETHE-HEITLER CONTRIBUTION

Normalisation of the BH MC

The Bethe-Heitler contribution to the signal has a special status in this analysis. Indeed, as being a pure QED process, it is assumed to be exactly known. The P. Guichon version of the BH cross section implemented inside HEPGen++ does take into account the complete effects of the muon mass. Moreover, if the BH process contributes on the entire phase-space to the signal, it appears that it dominates at high ν (or low x_B), where the DVCS part of the cross section is negligible and the exclusive π^0 production does not contribute. Hence for bins where ν is high enough, one expects that:

$$\sum_e^{\text{data}} \frac{1}{\Gamma(Q_e^2, \nu_e)} - k_{\text{BH}} \sum_e^{\text{BH}} \frac{w_{\text{BH}}}{\Gamma(Q_e^2, \nu_e)} = 0 \tag{105}$$

where the normalisation constant k_{BH} is independent of the bin.

This equality is twofold. Either one considers the equation to be true, and then finds out the value of k_{BH} normalising the MC on the data at high ν. Or one gets independently k_{BH} and uses the high ν data to verify whether the experiment and the simulation agree. This second way to look at equation 105 is the one intended in this analysis. The HEPGen++ generator allows for computing a so-called Monte-Carlo flux associated to the Monte-Carlo sample used. Hence k_{BH} is evaluated regardless of the data and any difference between data and Monte-Carlo points towards a problem.

The evaluation of the Monte-Carlo luminosity is done as follows:

$$\mathcal{L}_{\text{MC}} = \sum_{\Delta\Omega} w_{\text{DVCS}} \Big/ \int_{\Delta\Omega} \frac{\mathrm{d}\sigma^{\text{DVCS}}_{\text{HEPGen++}}}{\mathrm{d}\Omega} \mathrm{d}\Omega \tag{106}$$

where $\frac{\mathrm{d}\sigma^{\text{DVCS}}_{\text{HEPGen++}}}{\mathrm{d}\Omega}$ is the DVCS cross section implemented in HEPGen++. As $\mathcal{L}_{\text{MC}}$ does not depend on the process and as the DVCS cross section implemented in HEPGen++ benefits from a smoother behaviour comparatively to the BH one, the DVCS one is used for luminosity determination. It is nonetheless very important to integrate weights and cross section on the same (but arbitrary) phase-space $\Delta\Omega$. The normalisation constant is then simply given by:

$$k_{\text{BH}} = \frac{\mathcal{L}}{\mathcal{L}_{\text{MC}}} \tag{107}$$

where $\mathcal{L}$ stands for the luminosity of the data considered. More details about this procedure can be found in [42].

MC vs data comparison

In the following, I compare data and Monte-Carlo in the bin $80 < \nu < 144$ GeV, where I expect the BH to dominate. I will only show here the comparison between P08 slot4 μ^+ data (in red) to P08 μ^+ Monte-Carlo (in black). The Monte-Carlo is normalised independently of the data,

using the MC luminosity as described above, and contains preliminary 'mean' efficiencies for the tracking system as well as CAMERA and triggers efficiencies.

I display in figure 75 the longitudinal and transverse position of vertices. MC and data x- and y-positions of the vertices reasonably agree, while z-positions suffers from a small deviation upstream. Figure 76 displays the extrapolation of outgoing muon tracks at $z = 40$ meters. The overall shape of the triggers seems in agreement, but some parts of the MC trigger do not reproduce exactly the data despite large error bars. Figure 77 displays the position and energy of clusters. Most of these photons are collected in ECAL2. The MC does not reproduce well the shape of the energy distribution, despite the new calibration. Figure 78 displays the energy loss of the recoil proton in both Ring A and Ring B scintillators. Distributions reasonably agree except for the lower β part. This points that the CAMERA detection threshold is not properly tuned in the MC. Figure 79 displays the exclusivity variables distributions. Besides a problem of normalisation, all distributions have comparable width between data and MC. Δp_T is not centred in the data while it is in the MC. This points to a remaining problem in the CAMERA calibration.

The overall state of the MC is reasonable but the simulation still requires some tuning. Moreover, no bad-spill list nor requirement on detector stability are applied to the data, and detector efficiencies are not all included in the MC at the moment. The data overshoots the MC and this is partly due to the imperfect reproduction of the z-distribution of vertices, and improper CAMERA detection threshold.

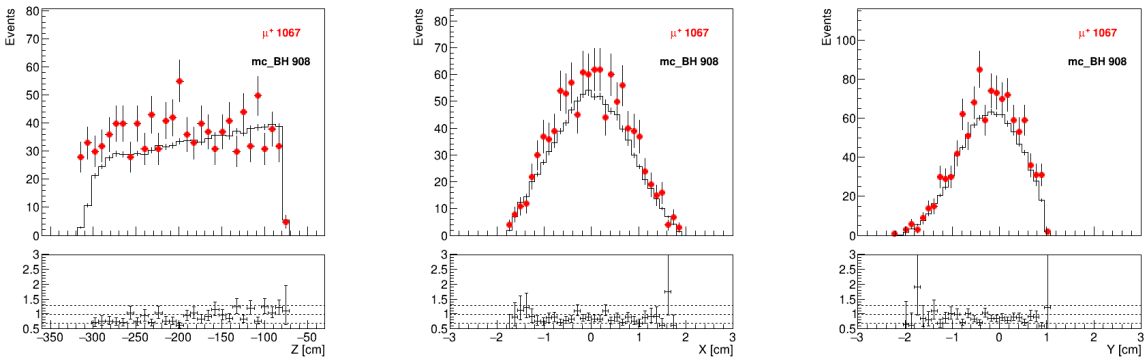

Figure 75: MC *vs* P08 slot4 data comparison: Distribution of z (left), x (middle) and y (right) position of vertices.

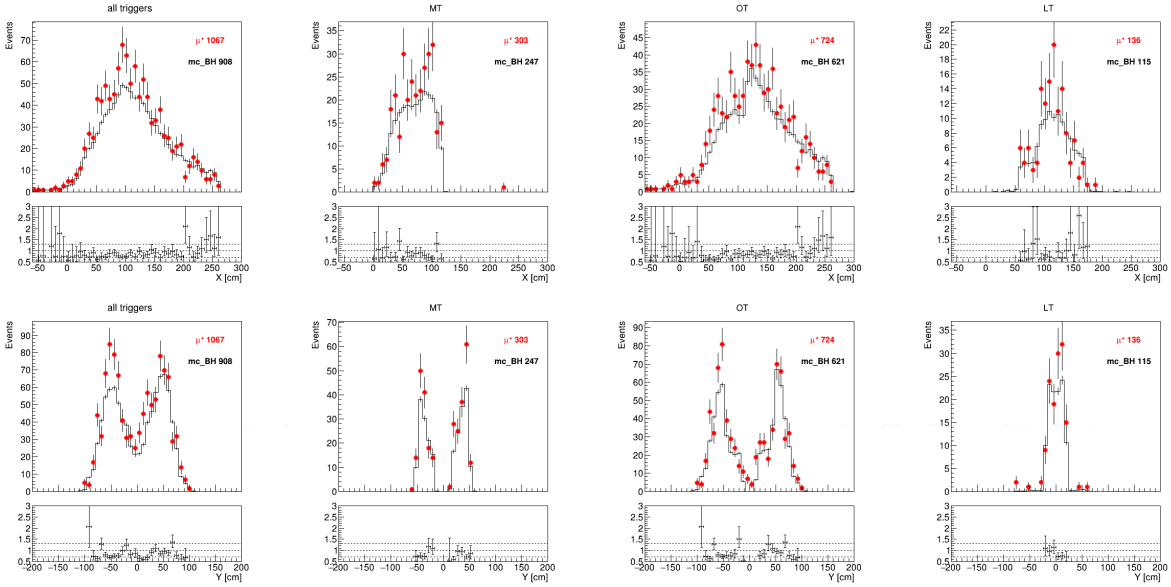

Figure 76: MC *vs* P08 slot4 data comparison: Distribution of x (top row) and y (bottom row) extrapolation of outgoing muon at $z = 40$ meters for all (first column), MT (second column), OT (third column) and LT (fourth column) events.

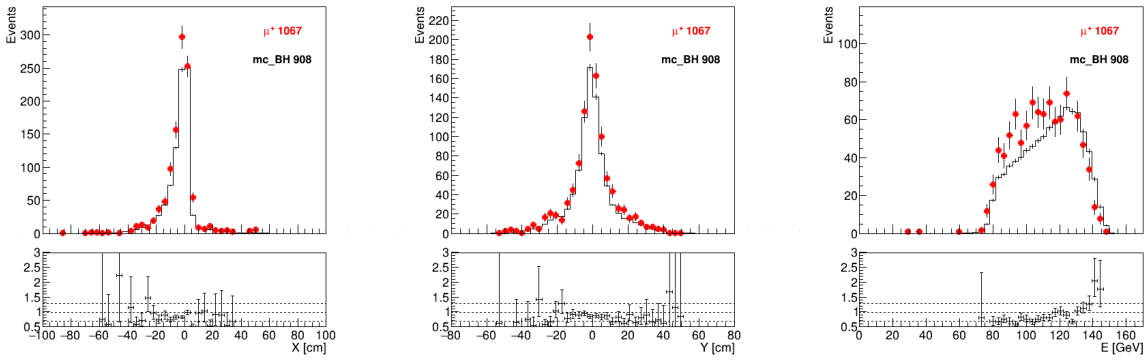

Figure 77: MC *vs* P08 slot4 data comparison: Distribution of x (left) and y (middle) position and energy (right) of the clusters.

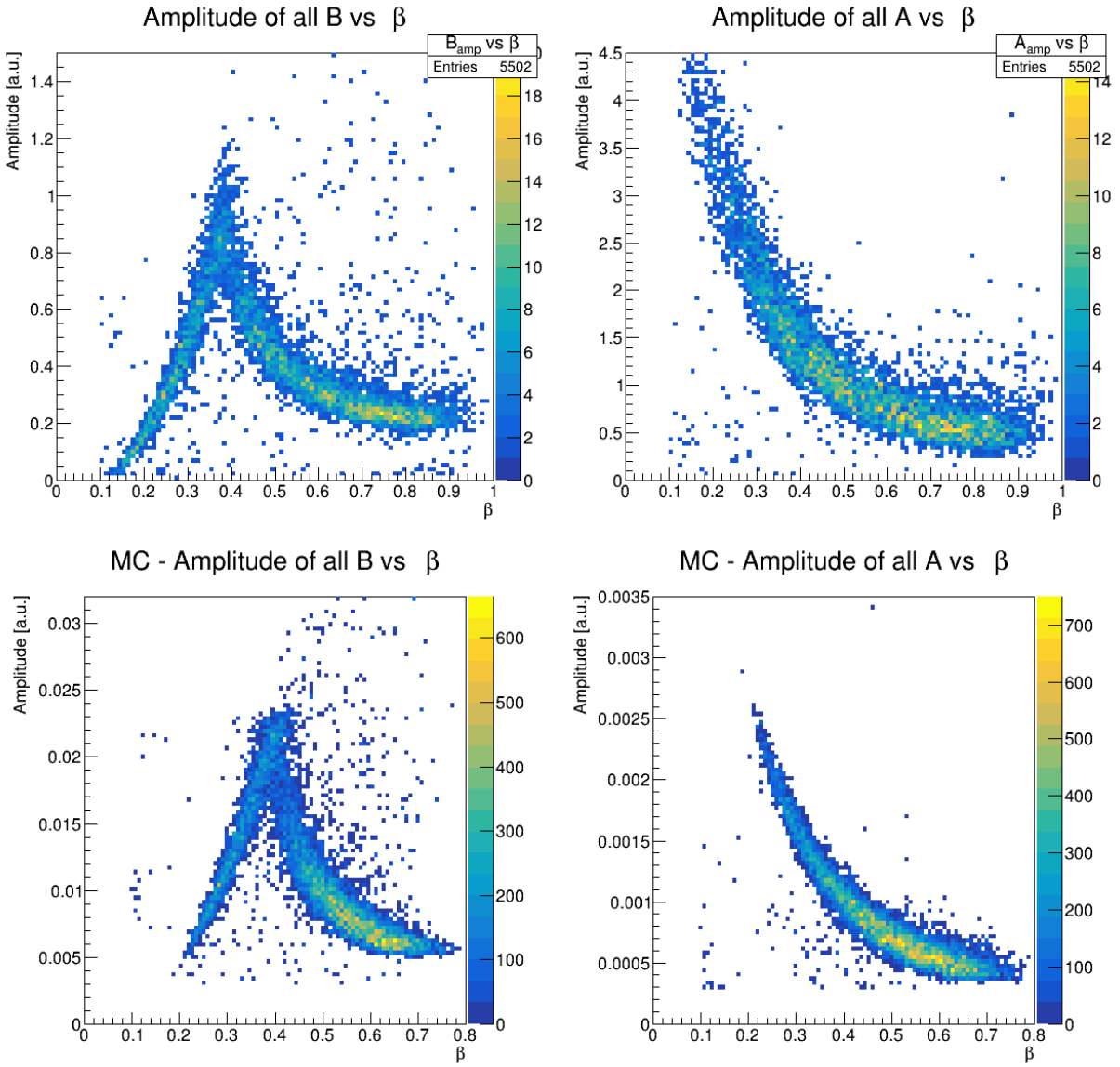

Figure 78: MC *vs* P08 slot4 data comparison: Energy deposit in Ring A (left) and Ring B (right) as a function of β of the recoil proton in real data (top row) and MC (bottom row).

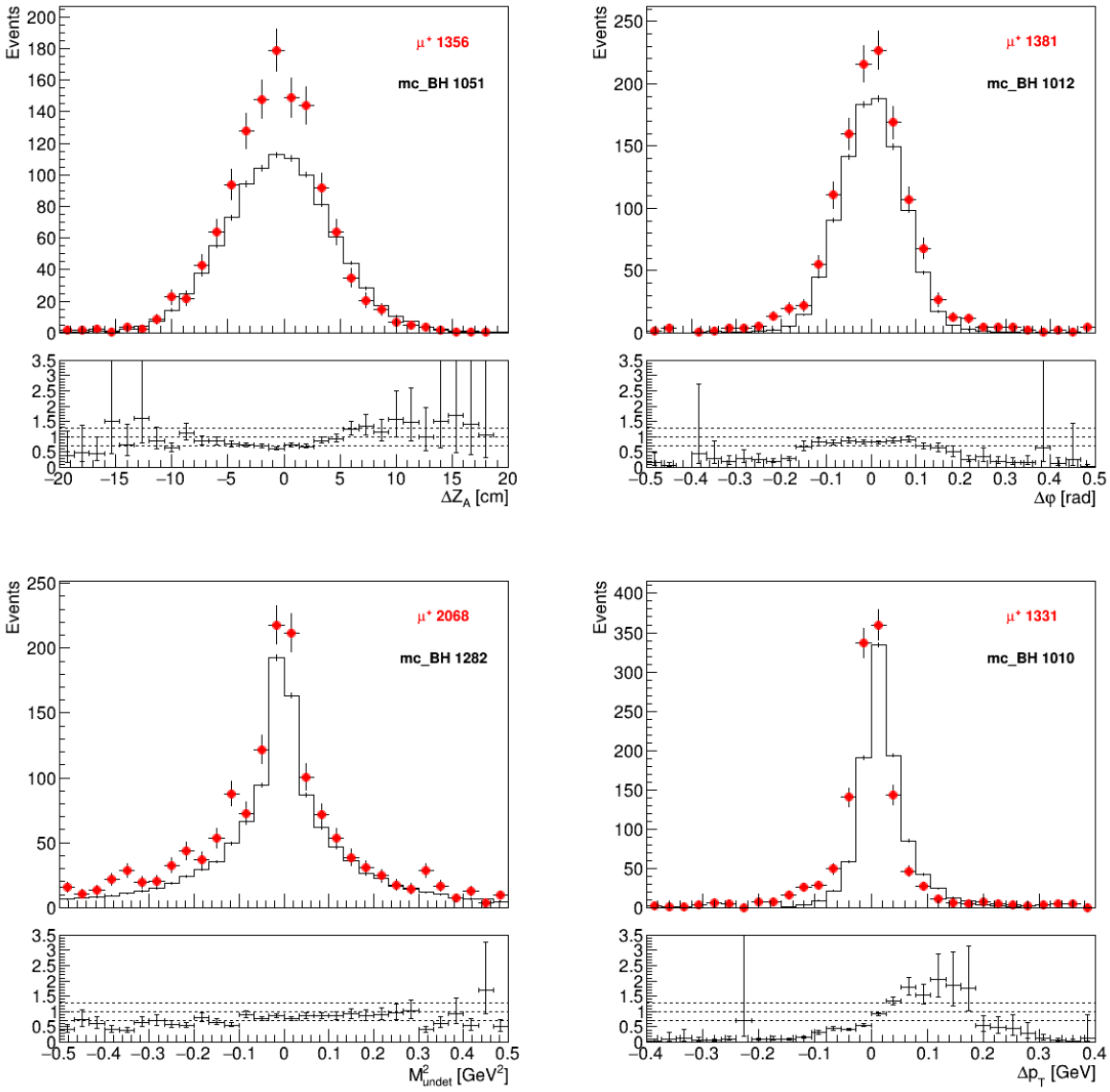

Figure 79: MC *vs* P08 slot4 data comparison: Distribution of exclusivity variables.

ϕ modulation of the exclusive single-photon production

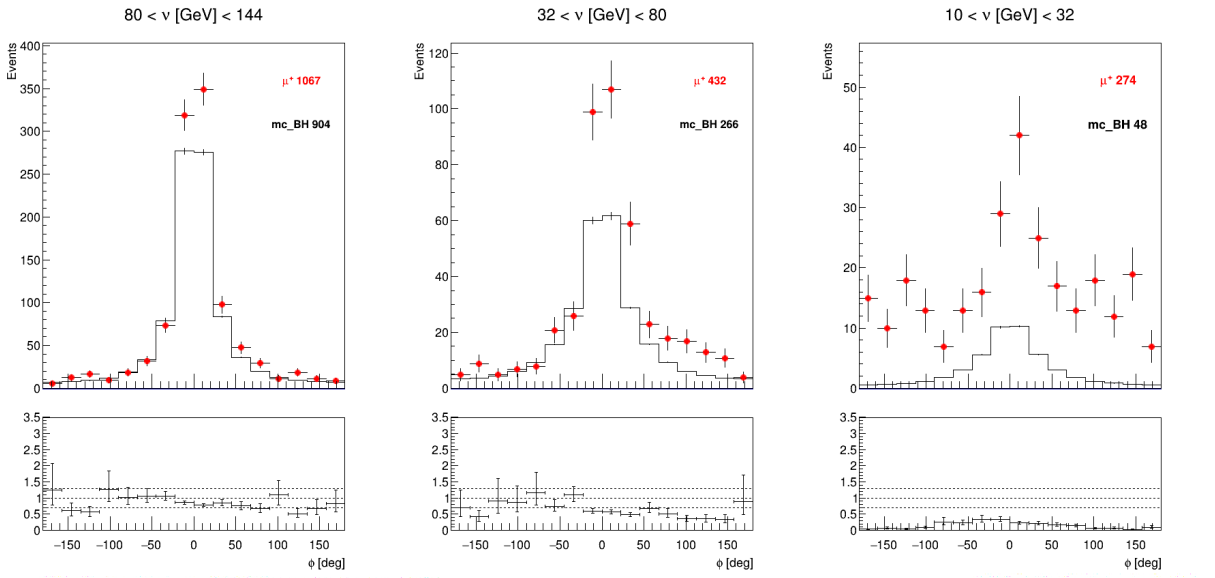

Figure 80: MC *vs* P08 slot4 data comparison: ϕ modulation of the exclusive single-photon event selection for three ν bins.

Figure 86 displays the ϕ modulation of the exclusive single-photon event selection for BH MC and all data for the entire ν coverage. In the high ν bin ($\nu > 80$ GeV), where BH is expected to be the only contribution,

data overshoots the BH simulation by about 17%. This still has to be understood but is rather positive already. In the two other bins at smaller ν, the difference between data and BH MC is large enough to make way for significant DVCS and interference contributions (even slightly contaminated by π^0). The study of the slope of the t-dependence of the extracted DVCS cross section will give further measurements of the transverse extension of the partons in the proton probed in the COMPASS experiment.

The current state of the ongoing analysis does not allow to extract any t-slope to be presented in this manuscript. Nonetheless, this work has pointed out several problems along with some methods for improvement. However, the reasonable agreement at high ν bin between data and MC normalised to the exact Bethe-Heitler cross section is very encouraging.

CONCLUSION AND PERSPECTIVES

I have presented in this thesis a first comprehensive analysis of exclusive single-photon production in the COMPASS 2016 data as a first step towards the extraction of the DVCS cross section. I described my input regarding the preparation of the analysis on both the target position determination and the CAMERA detector calibrations, as well as my systematic analysis of DIS, exclusive ρ^0 events and exclusive single-photon events in the complete 2016 data-set. I showed the compatibility between μ^+ and μ^- beam data for all physics channels above across the year, and discussed the quality and compatibility of the data across the different periods. This achievement is needed in order to allow for a convincing extraction of the beam charge and polarisation sum cross section, and required for further study related to the beam charge and polarisation difference. I presented a comparison of this data to a preliminary Monte-Carlo simulation normalised independently on the exact Bethe-Heitler cross section, and showed a relative agreement between data and simulation in a kinematic domain where data is dominated by the Bethe-Heitler process. This gives hope for a rigorous subtraction of the Bethe-Heitler contribution to the exclusive single-photon production cross section.

If this document summarises the results of about three years of work, and constitutes for me the conclusion of my involvement with the COMPASS collaboration, it is nothing but a step in this collaborative analysis. The precise extraction of the DVCS cross section requires a meticulous understanding of the data which is a completely collective process. Hard work is currently ongoing in order to refine the data:

- the delicate calibration of electromagnetic calorimeters is being worked through by Sergei Gerasimov, Marketa Peskova and Po-Ju Lin,
- exhaustive works on detector stability, on bad-spill and bad-run rejections are carried out by Andrea Moretti, Johannes Giarra and Jan Matousek respectively,
- a detailed study to optimise the usable time duration of each spill is performed by Johannes Giarra,
- an intensive work related to efficiencies extraction is taken care of by Anatolii Koval for the spectrometer, Johannes Giarra, Moritz Veit and Jens Barth for the triggers, and Sandro Scherrers for CAMERA,
- a complete DIS analysis aiming at extracting F_2 is carried out by Karolina Juraskova, who also studies the exclusive π^0 production together with Marketa Peskova,
- while Brian Ventura and Po-Ju Lin worked extensively with me in Saclay to produce those results on exclusive single-photon production.

This thorough investment from many physicists, and its extension to the COMPASS 2017 data-set, should lead to an extraction of the t-slope of the DVCS cross section with a statistics ten times bigger than in 2012. Studying its evolution in x_B should help constraining models for GPDs in-between valence and sea quarks and gluons kinematic region, and hence deepen our knowledge about the internal structure of the proton.

RÉSUMÉ EN FRANÇAIS

INTRODUCTION

Le processus DVCS ($\mu p \to \mu p$) consiste à sonder le proton à l'aide d'un photon virtuel qui va diffuser sur un des partons du nucléon. Ce parton va ensuite se désexciter en émettant un photon réel puis réintégrer le proton qui aura changé d'impulsion. La section efficace du processus DVCS est reliée aux distributions de partons généralisés (GPDs) qui encodent la corrélation entre l'impulsion longitudinale des particules qui composent le proton avec leur position dans le plan transverse.

Expérimentalement, on crée le photon virtuel en irradiant une cible d'hydrogène liquide avec des muons de haute énergie. Par conséquence, le DVCS interfère avec un second processus présentant le même état final et initial : le Bethe-Heitler (BH). Le BH est la radiation spontanée d'un photon réel par le muon avant ou après diffusion sur le proton. Cette contribution purement électromagnétique, calculable, doit être soustraite du signal mesuré dans l'expérience à l'aide d'une simulation.

L'objet de ce travail est d'avancer vers l'extraction de la section efficace du DVCS à partir des données collectées par COMPASS en 2016 et 2017.

L'EXPÉRIENCE COMPASS AU CERN

COMPASS est une expérience du SPS au CERN, dotée d'un faisceau de muon de 160 GeV qui est utilisé pour sonder les protons d'une cible d'hydrogène liquide. Les traces chargées sont détectées à l'avant dans un spectromètre constitué de nombreux trackers, tandis que les particules neutres déposent leur énergie dans les trois calorimètres électromagnétiques de l'expérience. Le proton de recul du DVCS est détecté dans un détecteur de temps de vol nommé CAMERA et disposé autour de la cible.

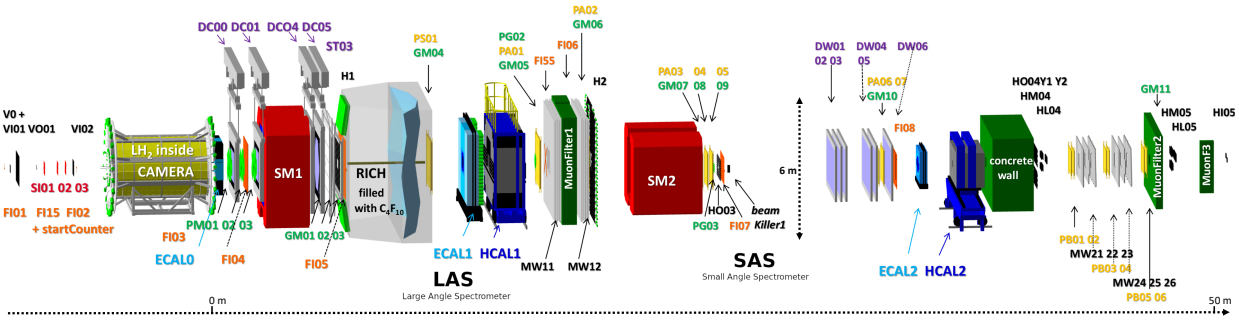

Figure 81: Schéma de principe de l'expérience COMPASS pour 2016 et 2017.

DETERMINATION DE LA POSITION DE LA CIBLE

Pour accéder à la section efficace du processus mesuré, il est nécessaire d'évaluer la luminosité incidente du dispositif expérimental. Cette étape requiert la connaissance précise de la position de la cible que j'ai eu à déterminer. Le résultat de cette analyse est présenté figure 82.

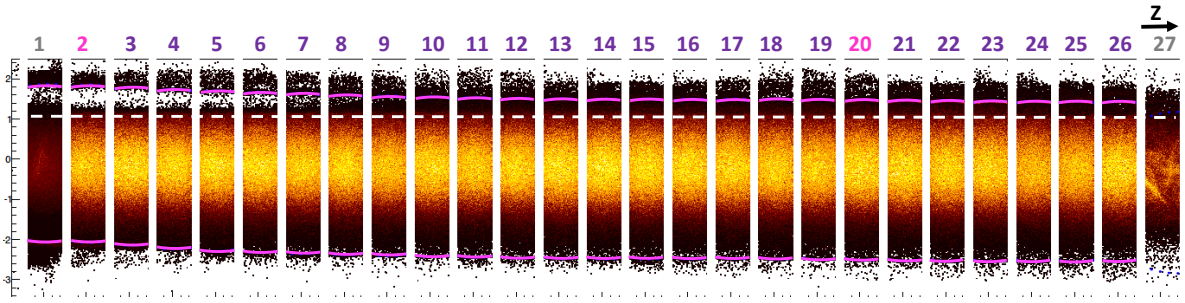

Figure 82: Tomographie de la cible d'hydrogène liquide.
Cette étude est réalisée en comptant le nombre de vertex dans la région de la cible. Les bords de la cible sont éclairés par le halo du faisceau et composés d'un matériau plus dense que l'hydrogène, dont on peut ensuite extraire la géométrie.

Les valeurs de chaque paramètre ajusté en fonction de z sont présenté figure 83. On constate que le rayon est constant le long de l'axe z et que $R_{cible} = 2 \pm 0.005cm$. La coordonnée x (coordonnée horizontale) du centre de la cible oscille autour de zéro de 1 mm sur une longueur de 2.4 m. La coordonnée y est volontairement incliné vers le bas afin de maintenir l'hydrogène gazeux au début de la cible, et est inclinée de 4 mm sur une longueur de 2.4 m.

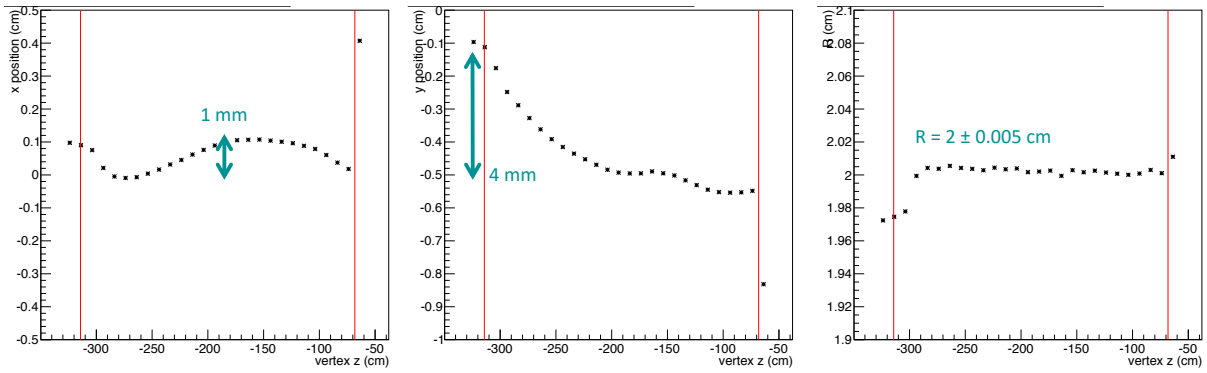

Figure 83: Position et rayon du centre de la cible en fonction de z.

CALIBRATION DE CAMERA

Pendant ma thèse je me suis également attelé à la calibration du détecteur de proton de recul CAMERA. Ce détecteur mesure le temps de vol des particules chargées sortant de la cible, et permet à la fois l'identification de la particule et la mesure de son impulsion. La calibration s'effectue en utilisant différents canaux de physiques, en comparant les données reconstruites à l'avant dans le spectromètre et les signaux dans CAMERA. Après calibration, l'impulsion

mesuré dans le spectromètre ou dans CAMERA doit être identique. Le résultat est présenté figure 84 pour l'impulsion d'un proton sortant de CAMERA dans le cas de la diffusion élastique d'un faisceau de pion sur le proton.

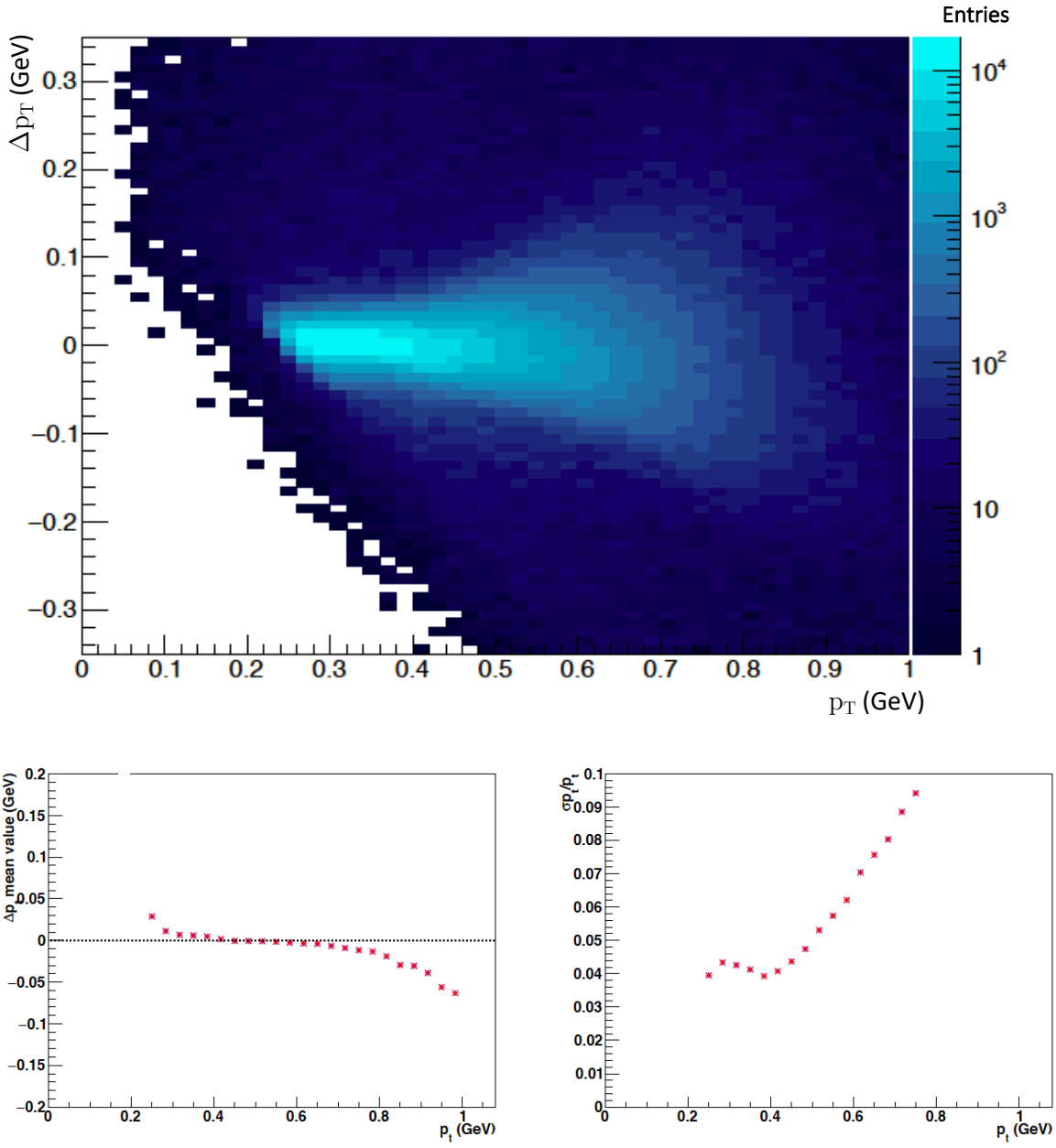

Figure 84: En haut : différence entre l'impulsion transverse reconstruite par masse manquante dans le spectromètre et par temps de vol dans CAMERA pour un proton de recul issu de la diffusion élastique d'un faisceau de pion sur le proton, en fonction de l'impulsion transverse reconstruite par masse manquante dans le spectromètre.
En bas à gauche : moyenne de la distribution du haut ajustée par un gaussienne.
En bas à droite : σ/p_T de la distribution du haut ajustée par un gaussienne.

ANALYSE DE LA PRODUCTION EXCLUSIVE DE PHOTONS UNIQUES

La sélection des événements exclusifs $lp \to lp\gamma$ combine les informations issues des calorimètres (où les photons sont détectés), du spectromètre (où les traces chargées sont reconstruites) et CAMERA (où le proton de recul est détecté). La modulation angulaire des évènements mesurés pour une période est présentée figure 85 pour trois régions en ν. Les variables cinématiques sont définies dans le corps de la thèse. Le résultat principal réside ici dans la compatibilité entre le signal obtenu pour le faisceau de μ^+ et de μ^-.

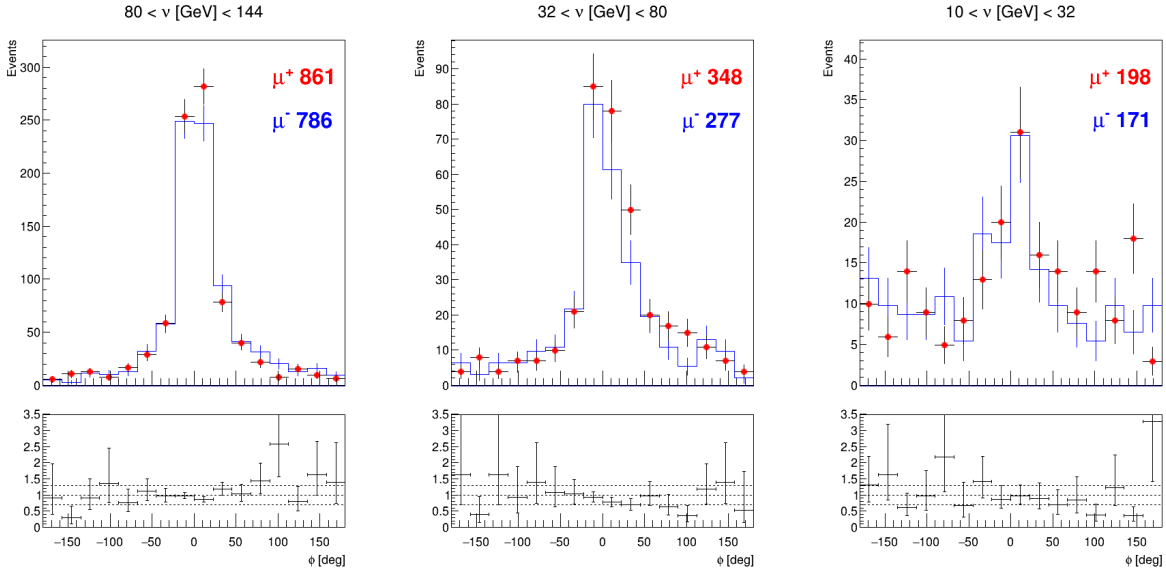

Figure 85: Événements exclusifs $lp \to lp\gamma$ en fonction de ϕ pour le faisceau de μ^+ (rouge) et de μ^- (bleu) pour trois régions en ν.

SIMULATION ET SOUSTRACTION DU BETHE-HEITLER

La contribution du BH pur est simulée afin d'être soustraite. L'interférence entre BH et DVCS sera soustraite par intégration en ϕ du signal. Le résultat de la simulation est présenté figure 86, où je compare la modulation en ϕ de la simulation et des évènements mesurés pour une période et trois régions en ν. A grand ν ($\nu > 80$ GeV), le BH est la seule contribution attendue. La contribution des données excède celle de la simulation (normalisée de manière indépendante) d'environ 17%. Ce premier résultat, bien qu'imparfait, est encourageant pour la suite de l'analyse. A plus petit ν, la différence entre la mesure et la simulation est suffisamment importante pour permettre une contribution du signal DVCS.

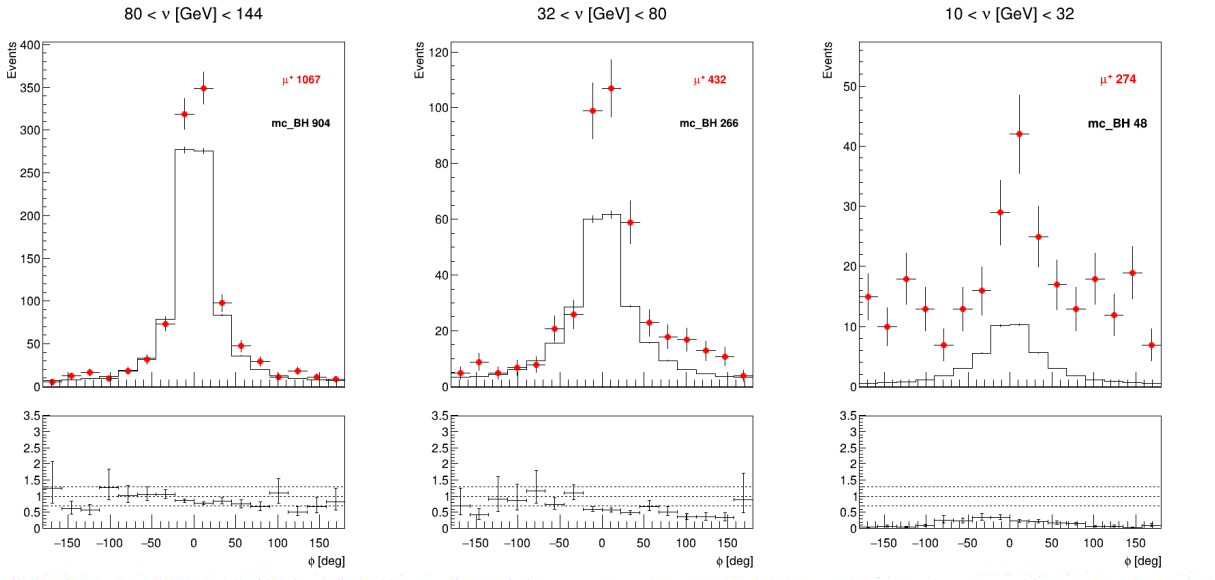

Figure 86: Événements exclusifs $lp \to lp\gamma$ en fonction de ϕ pour le faisceau de μ^+ (rouge) et pour la contribution du BH pur (noir) pour trois régions en ν.

CONCLUSIONS

Cette première analyse des évènements $lp \to lp\gamma$ doit encore être affinée avant de permettre l'extraction rigoureuse de la section efficace du processus DVCS et de sa pente en t. En particulier les systématiques par périodes présentées dans le corps de la thèse empêchent de raisonnablement sommer la statistique à ce stade de l'analyse. Une attention particulière doit encore être portée sur la calibration des calorimètres, la rejection des mauvais *spills*, la prise en compte des efficacités des détecteurs, et la qualité de la simulation.

BIBLIOGRAPHY

[1] F. D. Aaron et al. "Measurement of deeply virtual Compton scattering and its t-dependence at HERA". In: *Phys. Lett.* B659 (2008), pp. 796–806. DOI: 10.1016/j.physletb.2007.11.093. arXiv: 0709.4114 [hep-ex].

[2] F. D. Aaron et al. "Deeply Virtual Compton Scattering and its Beam Charge Asymmetry in e+- Collisions at HERA". In: *Phys. Lett.* B681 (2009), pp. 391–399. DOI: 10.1016/j.physletb.2009.10.035. arXiv: 0907.5289 [hep-ex].

[3] P. Abbon et al. "The COMPASS experiment at CERN". In: *Nucl. Instrum. Meth.* A577 (2007), pp. 455–518. DOI: 10.1016/j.nima.2007.03.026. arXiv: hep-ex/0703049 [hep-ex].

[4] Ph. Abbon et al. "The COMPASS Setup for Physics with Hadron Beams". In: *Nucl. Instrum. Meth.* A779 (2015), pp. 69–115. DOI: 10.1016/j.nima.2015.01.035. arXiv: 1410.1797 [physics.ins-det].

[5] R. Akhunzyanov et al. "Transverse extension of partons in the proton probed in the sea-quark range by measuring the DVCS cross section". In: *Phys. Lett.* B793 (2019), pp. 188–194. DOI: 10.1016/j.physletb.2019.04.038.

[6] A. Aktas et al. "Measurement of deeply virtual compton scattering at HERA". In: *Eur. Phys. J.* C44 (2005), pp. 1–11. DOI: 10.1140/epjc/s2005-02345-3. arXiv: hep-ex/0505061 [hep-ex].

[7] M. G. Alexeev et al. "Measurement of the cross section for hard exclusive π^0 leptoproduction". In: (2019). arXiv: 1903.12030 [hep-ex].

[8] Elke-Caroline Aschenauer, Salvatore Fazio, Kresimir Kumericki, and Dieter Mueller. "Deeply Virtual Compton Scattering at a Proposed High-Luminosity Electron-Ion Collider". In: *JHEP* 09 (2013), p. 093. DOI: 10.1007/JHEP09(2013)093. arXiv: 1304.0077 [hep-ph].

[9] Alessandro Bacchetta, Umberto D'Alesio, Markus Diehl, and C. Andy Miller. "Single-spin asymmetries: The Trento conventions". In: *Phys. Rev.* D70 (2004), p. 117504. DOI: 10.1103/PhysRevD.70.117504. arXiv: hep-ph/0410050 [hep-ph].

[10] Andrei V. Belitsky, Dieter Mueller, and A. Kirchner. "Theory of deeply virtual Compton scattering on the nucleon". In: *Nucl. Phys.* B629 (2002), pp. 323–392. DOI: 10.1016/S0550-3213(02)00144-X. arXiv: hep-ph/0112108 [hep-ph].

[11] Jan C. Bernauer and Michael O. Distler. "Avoiding common pitfalls and misconceptions in extractions of the proton radius". In: *ECT* Workshop on The Proton Radius Puzzle Trento, Italy, June 20-24, 2016*. 2016. arXiv: 1606.02159 [nucl-th].

[12] C. Bernet et al. "The COMPASS trigger system for muon scattering". In: *Nucl. Instrum. Meth.* A550 (2005), pp. 217–240. DOI: 10.1016/j.nima.2005.05.043.

[13] B. Berthou et al. "PARTONS: PARtonic Tomography Of Nucleon Software". In: *Eur. Phys. J.* C78.6 (2018), p. 478. DOI: 10.1140/epjc/s10052-018-5948-0. arXiv: 1512.06174 [hep-ph].

[14] E. Bielert et al. “A 2.5 m long liquid hydrogen target for COMPASS”. In: *Nucl. Instrum. Meth.* A746 (2014), pp. 20–25. DOI: 10.1016/j.nima.2014.01.067.

[15] Matthias Burkardt. “Impact parameter dependent parton distributions and off forward parton distributions for zeta —> 0”. In: *Phys. Rev.* D62 (2000). [Erratum: Phys. Rev.D66,119903(2002)], p. 071503. DOI: 10.1103/PhysRevD.62.071503,10.1103/PhysRevD.66.119903. arXiv: hep-ph/0005108 [hep-ph].

[16] Matthias Burkardt. “Impact parameter space interpretation for generalized parton distributions”. In: *Int. J. Mod. Phys.* A18 (2003), pp. 173–208. DOI: 10.1142/S0217751X03012370. arXiv: hep-ph/0207047 [hep-ph].

[17] Matthias Burkardt. “GPDs with zeta not equal 0”. In: (2007). arXiv: 0711.1881 [hep-ph].

[18] C.E. Carlson. *Theoretical overview on the proton radius puzzle*. IWHSS, Bonn. March 2018. URL: https://indico.cern.ch/event/658983/contributions/2915165/attachments/1619890/2576809/CEC_PRad_Bonn_2018.pdf.

[19] S. Chekanov et al. “A Measurement of the Q^2, W and t dependences of deeply virtual Compton scattering at HERA”. In: *JHEP* 05 (2009), p. 108. DOI: 10.1088/1126-6708/2009/05/108. arXiv: 0812.2517 [hep-ex].

[20] Nabil Chouika. “Generalized Parton Distributions and their covariant extension : towards nucleon tomography”. Thèse de doctorat dirigée par Moutarde, Hervé Physique hadronique Paris Saclay 2018. PhD thesis. 2018. URL: http://www.theses.fr/2018SACLS259.

[21] Maxime Defurne. “Photon and π^0 electroproduction at Jefferson Laboratory-Hall A”. Thèse de doctorat dirigée par Sabatié, Franck Physique Paris 11 2015. PhD thesis. 2015. URL: http://www.theses.fr/2015PA112105.

[22] M. Diehl. “Generalized parton distributions in impact parameter space”. In: *Eur. Phys. J.* C25 (2002). [Erratum: Eur. Phys. J.C31,277(2003)], pp. 223–232. DOI: 10.1007/s10052-002-1016-9. arXiv: hep-ph/0205208 [hep-ph].

[23] M. Diehl. “Generalized parton distributions”. In: *Phys. Rept.* 388 (2003), pp. 41–277. DOI: 10.1016/j.physrep.2003.08.002,10.3204/DESY-THESIS-2003-018. arXiv: hep-ph/0307382 [hep-ph].

[24] M. Diehl. *Introduction to perturbative QCD and factorization*. Ecole Joliot-Curie, La Grande Motte. October 2018. URL: https://ejc2018.sciencesconf.org/resource/page/id/4.

[25] Markus Diehl. “Introduction to GPDs and TMDs”. In: *Eur. Phys. J.* A52.6 (2016), p. 149. DOI: 10.1140/epja/i2016-16149-3. arXiv: 1512.01328 [hep-ph].

[26] Raphael Dupre, Michel Guidal, and Marc Vanderhaeghen. “Tomographic image of the proton”. In: *Phys. Rev.* D95.1 (2017), p. 011501. DOI: 10.1103/PhysRevD.95.011501. arXiv: 1606.07821 [hep-ph].

[27] Raphaël Dupré, Michel Guidal, Silvia Niccolai, and Marc Vanderhaeghen. “Analysis of Deeply Virtual Compton Scattering Data at Jefferson Lab and Proton Tomography”. In: *Eur. Phys. J.* A53.8 (2017), p. 171. DOI: 10.1140/epja/i2017-12356-8. arXiv: 1704.07330 [hep-ph].

[28] L. Favart, M. Guidal, T. Horn, and P. Kroll. "Deeply Virtual Meson Production on the nucleon". In: *Eur. Phys. J.* A52.6 (2016), p. 158. DOI: 10.1140/epja/i2016-16158-2. arXiv: 1511.04535 [hep-ph].

[29] Andrea Ferrero. "Nucleon Structure with TMDs and GPDs". Thèse d'habilitation à diriger les recherches, Université Paris-Sud, 2017. PhD thesis. 2017.

[30] F Gautheron et al. "COMPASS-II Proposal". In: (2010).

[31] S. V. Goloskokov and P. Kroll. "Vector meson electroproduction at small Bjorken-x and generalized parton distributions". In: *Eur. Phys. J.* C42 (2005), pp. 281–301. DOI: 10.1140/epjc/s2005-02298-5. arXiv: hep-ph/0501242 [hep-ph].

[32] S. V. Goloskokov and P. Kroll. "The Role of the quark and gluon GPDs in hard vector-meson electroproduction". In: *Eur. Phys. J.* C53 (2008), pp. 367–384. DOI: 10.1140/epjc/s10052-007-0466-5. arXiv: 0708.3569 [hep-ph].

[33] S. V. Goloskokov and P. Kroll. "An Attempt to understand exclusive pi+ electroproduction". In: *Eur. Phys. J.* C65 (2010), pp. 137–151. DOI: 10.1140/epjc/s10052-009-1178-9. arXiv: 0906.0460 [hep-ph].

[34] S. V. Goloskokov and P. Kroll. "Transversity in hard exclusive electroproduction of pseudoscalar mesons". In: *Eur. Phys. J.* A47 (2011), p. 112. DOI: 10.1140/epja/i2011-11112-6. arXiv: 1106.4897 [hep-ph].

[35] P.A.M. Guichon. *Private communication*. 2015.

[36] L. N. Hand. "Experimental investigation of pion electroproduction". In: *Phys. Rev.* 129 (1963), pp. 1834–1846. DOI: 10.1103/PhysRev.129.1834.

[37] R. Hofstadter and R. W. McAllister. "Electron Scattering From the Proton". In: *Phys. Rev.* 98 (1955), pp. 217–218. DOI: 10.1103/PhysRev.98.217.

[38] Robert Hofstadter. "Electron Scattering and Nuclear Structure". In: *Rev. Mod. Phys.* 28 (3 1956), pp. 214–254. DOI: 10.1103/RevModPhys.28.214. URL: https://link.aps.org/doi/10.1103/RevModPhys.28.214.

[39] G. Ingelman, A. Edin, and J. Rathsman. "LEPTO 6.5: A Monte Carlo generator for deep inelastic lepton - nucleon scattering". In: *Comput. Phys. Commun.* 101 (1997), pp. 108–134. DOI: 10.1016/S0010-4655(96)00157-9. arXiv: hep-ph/9605286 [hep-ph].

[40] Xiang-Dong Ji. "Deeply virtual Compton scattering". In: *Phys. Rev.* D55 (1997), pp. 7114–7125. DOI: 10.1103/PhysRevD.55.7114. arXiv: hep-ph/9609381 [hep-ph].

[41] Xiang-Dong Ji. "Gauge-Invariant Decomposition of Nucleon Spin". In: *Phys. Rev. Lett.* 78 (1997), pp. 610–613. DOI: 10.1103/PhysRevLett.78.610. arXiv: hep-ph/9603249 [hep-ph].

[42] Philipp Jörg. "Deeply virtual compton scattering at CERN - what is the size of the proton?" Thèse de doctorat dirigée par Fischer, Horst Physique hadronique Albert-Ludwigs-Universität Freiburg 2017. PhD thesis. 2018. URL: https://freidok.uni-freiburg.de/data/12397.

[43] Kresimir Kumericki, Simonetta Liuti, and Herve Moutarde. "GPD phenomenology and DVCS fitting". In: *Eur. Phys. J.* A52.6 (2016), p. 157. DOI: 10.1140/epja/i2016-16157-3. arXiv: 1602.02763 [hep-ph].

[44] Kresimir Kumerički and Dieter Mueller. "Deeply virtual Compton scattering at small x_B and the access to the GPD H". In: *Nucl. Phys.* B841 (2010), pp. 1–58. DOI: 10.1016/j.nuclphysb.2010.07.015. arXiv: 0904.0458 [hep-ph].

[45] Kresimir Kumerički, Dieter Müller, and Morgan Murray. "HERMES impact for the access of Compton form factors". In: *Phys. Part. Nucl.* 45.4 (2014), pp. 723–755. DOI: 10.1134/S1063779614040108. arXiv: 1301.1230 [hep-ph].

[46] Krešimir Kumerički and Dieter Müller. "Description and interpretation of DVCS measurements". In: *EPJ Web Conf.* 112 (2016), p. 01012. DOI: 10.1051/epjconf/201611201012. arXiv: 1512.09014 [hep-ph].

[47] C. Lorce and B. Pasquini. "Quark Wigner Distributions and Orbital Angular Momentum". In: *Phys. Rev.* D84 (2011), p. 014015. DOI: 10.1103/PhysRevD.84.014015. arXiv: 1106.0139 [hep-ph].

[48] Cédric Lorcé, Hervé Moutarde, and Arkadiusz P. Trawiński. "Revisiting the mechanical properties of the nucleon". In: *Eur. Phys. J.* C79.1 (2019), p. 89. DOI: 10.1140/epjc/s10052-019-6572-3. arXiv: 1810.09837 [hep-ph].

[49] Cédric Mezrag. "Generalised Parton Distributions : from phenomenological approaches to Dyson-Schwinger equations". Thèse de doctorat dirigée par Sabatié, Franck Physique Paris 11 2015. PhD thesis. 2015. URL: http://www.theses.fr/2015PA112144.

[50] Gerald A. Miller. "The Proton Radius Puzzle- Why We All Should Care". In: *13th Conference on the Intersections of Particle and Nuclear Physics (CIPANP 2018) Palm Springs, California, USA, May 29-June 3, 2018*. 2018. arXiv: 1809.09635 [physics.atom-ph].

[51] Gerald A. Miller. "Defining the proton radius: A unified treatment". In: *Phys. Rev.* C99.3 (2019), p. 035202. DOI: 10.1103/PhysRevC.99.035202. arXiv: 1812.02714 [nucl-th].

[52] Laurent Mossé. "Etude de la diffusion Compton virtuelle en régime profondément inélastique pour le dispositif expérimental COMPASS". Thèse de doctorat dirigée par D'Hose, Nicole Physique Paris 11 2002. PhD thesis. 2002, 194 p. URL: http://www.theses.fr/2002PA112027.

[53] H. Moutarde, P. Sznajder, and J. Wagner. "Border and skewness functions from a leading order fit to DVCS data". In: *Eur. Phys. J.* C78.11 (2018), p. 890. DOI: 10.1140/epjc/s10052-018-6359-y. arXiv: 1807.07620 [hep-ph].

[54] H. Moutarde, P. Sznajder, and J. Wagner. "Unbiased determination of DVCS Compton Form Factors". In: *Eur. Phys. J.* C79.7 (2019), p. 614. DOI: 10.1140/epjc/s10052-019-7117-5. arXiv: 1905.02089 [hep-ph].

[55] Dieter Müller, D. Robaschik, B. Geyer, F. M. Dittes, and J. Hořejši. "Wave functions, evolution equations and evolution kernels from light ray operators of QCD". In: *Fortsch. Phys.* 42 (1994), pp. 101–141. DOI: 10.1002/prop.2190420202. arXiv: hep-ph/9812448 [hep-ph].

[56] Maxim V. Polyakov and Peter Schweitzer. "Forces inside hadrons: pressure, surface tension, mechanical radius, and all that". In: *Int. J. Mod. Phys.* A33.26 (2018), p. 1830025. DOI: 10.1142/S0217751X18300259. arXiv: 1805.06596 [hep-ph].

[57] J. Pretz. *Virtual Photon Flux Factor, not neglection the lepton mass*. COMPASS Note. November 2002.

[58] A. V. Radyushkin. "Scaling limit of deeply virtual Compton scattering". In: *Phys. Lett.* B380 (1996), pp. 417–425. DOI: 10.1016/0370-2693(96)00528-X. arXiv: hep-ph/9604317 [hep-ph].

[59] A. V. Radyushkin. "Nonforward parton distributions". In: *Phys. Rev.* D56 (1997), pp. 5524–5557. DOI: 10.1103/PhysRevD.56.5524. arXiv: hep-ph/9704207 [hep-ph].

[60] C. Regali and T. Szameitat. *TGEANT, A Geant4 based Monte Carlo simulation for the COMPASS-II experiment*. URL: https://na58-project-tgeant.web.cern.ch/.

[61] Christopher Regali. "Exclusive event generation for the COMPASS II experiment at CERN and improvements for the Monte-Carlo chain". Thèse de doctorat dirigée par Fisher, Horst Physique hadronique Albert-Ludwigs-Universität Freiburg 2016. PhD thesis. 2016.

[62] A. Sandacz and P. Sznajder. "HEPGEN - generator for hard exclusive leptoproduction". In: (2012). arXiv: 1207.0333 [hep-ph].

[63] S. Strauch. *The proton charge-radius puzzle*. IWHSS, Aveiro. June 2019. URL: https://indico.cern.ch/event/784271/contributions/3395431/attachments/1868063/3073146/IWHSS-2019_Strauch.pdf.

[64] M. Tanabashi et al. "Review of Particle Physics". In: *Phys. Rev.* D98.3 (2018), p. 030001. DOI: 10.1103/PhysRevD.98.030001.

[65] Richard E. Taylor. "Deep inelastic scattering: The Early years". In: *Rev. Mod. Phys.* 63 (1991), pp. 573–595. DOI: 10.1103/RevModPhys.63.573.

[66] J-L. Ville. *CAMERA: Study of elastic events*. 2012. URL: http://wwwcompass.cern.ch/compass/gpd/meetings/201211_14nov_CERN/Jean-Loup.ElasticStudy_GPD_meeting.pdf.

[67] Eugene P. Wigner. "On the quantum correction for thermodynamic equilibrium". In: *Phys. Rev.* 40 (1932), pp. 749–760. DOI: 10.1103/PhysRev.40.749.

[68] Nicole d'Hose, Silvia Niccolai, and Armine Rostomyan. "Experimental overview of Deeply Virtual Compton Scattering". In: *Eur. Phys. J.* A52.6 (2016), p. 151. DOI: 10.1140/epja/i2016-16151-9.

université PARIS-SACLAY | ÉCOLE DOCTORALE PHENIICS

Titre : Étude de la structure interne du proton par diffusion Compton virtuelle à COMPASS, CERN

Mots clés : Diffusion Compton, Structure interne du nucléon, Distributions de partons Généralisées, COMPASS

Résumé : La diffusion Compton virtuelle (DVCS) est un processus idéal pour étudier la structure interne du proton. Cette réaction exclusive permet d'accéder aux distributions de partons généralisées (GPDs) qui encodent les corrélations entre impulsion longitudinale et position transverse des partons à l'intérieur du proton. Le DVCS consiste à sonder le proton au moyen d'un photon virtuel de grande virtualité pour produire dans l'état final un unique photon réel de grande énergie tout en laissant le proton intact.
A COMPASS au CERN, où deux années de données ont été collectées en 2016 et 2017 afin de mesurer la section efficace du processus DVCS, le photon virtuel est issu de la diffusion d'un faisceau de μ^+ ou de μ^- polarisé de 160 GeV sur une cible d'hydrogène liquide. Toutes les particules de la réaction sont détectées dans l'expérience : le muon incident est détecté dans le télescope du faisceau, le muon diffracté et le photon réel sont détectés à l'avant dans le spectromètre et les trois calorimètres tandis que le proton de recul est détecté dans un détecteur de temps de vol placé autour de la cible.
Je présente dans cette thèse l'état de l'analyse du processus DVCS sur les données collectées à COMPASS en 2016. Après un rappel du contexte théorique et expérimental, je décris l'expérience COMPASS. Je détaille ensuite mon travail de calibration du détecteur de proton de recul et de détermination de la position exacte de la cible de 2 cm de diamètre et 2.5 m de longueur. J'étudie dans la partie suivante la sélection de différents canaux de physique permettant de contrôler de manière systématique la qualité des détecteurs : la diffusion profondément inélastique (DIS) qui implique le télescope du faisceau et le spectromètre, la production exclusive de $/rho^0$ qui inclut aussi le détecteur de temps de vol ; puis je présente la première analyse de la production exclusive de photons uniques qui implique en plus les trois calorimètres. Dans une dernière partie j'évoque les étapes nécessaires à la détermination de la section efficace du DVCS à partir de cette sélection, et je présente les premiers résultats issus de la simulation associée.

Title : Probing the proton structure through deep virtual Compton scattering at COMPASS, CERN

Keywords : Deep virtual Compton scattering, Internal structure of the nucleon, Generalised parton distributions, COMPASS

Abstract : Virtual Compton Scattering (DVCS) is an ideal process to study the internal structure of proton. This exclusive reaction provides access to generalised parton distributions (GPDs), which encode the correlations between longitudinal momentum and transverse position of partons inside the proton. DVCS consists in probing a proton with a virtual photon of high virtuality, in order to produce a single high energy real photon while leaving the proton intact in the final state.
At COMPASS at CERN, where two years of data were collected in 2016 and 2017 to measure the DVCS cross section, the virtual photon is produced by scattering of a 160 GeV polarised μ^+ or μ^- beam on a liquid hydrogen target. All particles are detected in the experiment: the incident muon is detected in the beam telescope, the diffracted muon and the real photon are detected in the forward spectrometer and the three calorimeters, while the recoil proton is detected in a time-of-flight detector positioned around the target.
In this thesis I present the state of the analysis of the DVCS process on the data collected at COMPASS in 2016. After a reminder of the theoretical and experimental context, I describe the COMPASS experiment. I then detail my work on calibrating the recoil proton detector and determining the the exact position of the 2 cm diameter and 2.5 m long target. In the next section, I study the selection of different physics channels used to systematically control detector quality: Deep Inelastic Scattering (DIS) which involves the beam-telescope and spectrometer, exclusive $/rho^0$ production which requires the addition of the time-of-flight detector and I follow with the first analysis of the exclusive single photon production which depends as well on the calorimetres quality. In a last part, I discuss the necessary steps needed to extract the DVCS cross-section out of this event selection, and present the first results associated to the Monte-Carlo simulation.

Université Paris-Saclay
Espace Technologique / Immeuble Discovery
Route de l'Orme aux Merisiers RD 128 / 91190 Saint-Aubin, France